UNIVERSITY OF CALIFORNIA, SAN DIEGO

Surface-towed controlled source electromagnetic system for mapping extent of subsea permafrost on the Beaufort shelf, Alaska

A dissertation submitted in partial satisfaction of the
requirements for the degree
Doctor of Philosophy

in

Earth Sciences

by

Joanna E Sherman

Committee in charge:

Professor Steven C. Constable, Chair
Professor Adrian Borsa
Professor Adam Burgasser
Professor James Day
Professor Kerry Key
Professor Leonard Snrka

2018

The dissertation of Joanna E Sherman is approved, and it is acceptable in quality and form for publication on microfilm and electronically:

_____

_____

_____

_____

_____

_____

Chair

University of California, San Diego

2018

DEDICATION

For my sister Arwyn, who has been my rock over the years.

EPIGRAPH

"But then...it used to be so simple, once upon a time.

Because the universe was full of ignorance all around and the scientist panned through it like a prospector crouched over a mountain steam, looking for the gold of knowledge among the gravel of unreason, the sand of uncertainty and the little whiskery eight-legged swimming things of superstition.

Occasionally he would straighten up and say things like "Hurrah, I've discovered Boyle's Third Law." And everyone knew where they stood. But the trouble was that ignorance became more interesting, especially big fascinating ignorance about huge and important things like matter and creation, and people stopped patiently building their little houses of rational sticks in the chaos of the universe and started getting interested in the chaos itself-partly because it was a lot easier to be an expert on chaos, but mostly because it made really good patterns that you could put on a t-shirt."

- Terry Pratchett, from *Witches Abroad*

TABLE OF CONTENTS

LIST OF FIGURES

LIST OF TABLES

ACKNOWLEDGEMENTS

First and foremost I would like to thank my advisor, Steve Constable, for his many years of mentorship and for opening this door for me. I was one of the undergraduate students Steve has recruited from his Exploration Geophysics class over the years. He told me coming to Scripps for graduate school was a possibility and gave me a taste of what the experience would be like by inviting me on a research cruise to San Nicholas Basin, CA over winter break and teaching me how to process and invert the MT data from that cruise during a 10-week independent study program. From that starting point Steve provided opportunities for me to travel the world for projects and conferences - Germany, Thailand, Uruguay, the Alaskan Arctic, Dutch Harbor, and Japan- and I am grateful for all the time spent abroad and at sea during my doctoral work. Lastly, I am grateful to both Steve and Cathy for opening their home on so many occasions for dinner and always making me feel welcome.

Kerry Key deserves a shoutout for his willingness to pause his busy life to answer my questions and help me with my struggles through my entire phD. And for all the weeks he motivated our lab to make the trek out to Don Carlos to get delicious burritos for lunch.

The older students in the Marine EM lab, especially Samer Naif and Peter Kannberg, deserve a thank you for all their help and profitable discussions. Peter specifically put a lot of time and effort into planning field work in the Arctic for this project and did some of the initial processing, and then let me steal this project from him after his committee told him he had too much data for one dissertation. And also a thank you to David Myer

for his invaluable help on all things code and computer related.

And a heartfelt thank you to the rest of the marine EM lab family: John Souders, Jaques Lemire, Chris Armeding, and Jake Perez for all their hard work preparing and executing project after project with so much success. And for making life more fun along the way.

Funding was provided by Department of Energy (contract no. DE-FE0010144). Special thanks go to Carolyn Ruppel of the USGS for extensive advice on logistics, providing seismic line locations and digital well logs. We thank Kerry Key for use of his MARE2DEM inversion code, which can be downloaded from http://mare2dem.ucsd.edu. BP provided access to West Dock. We thank the owner and captain of the RV Ukpik, Bill Kopplin and Mike Flemming. Finally, we acknowledge the Scripps Electromagnetic Methods Consortium for continued support and funding of DS. Data used in this paper may be found online at http://marineemlab.ucsd.edu.

The text in Chapter 4, in part or in full, is a reprint of material from its publication in *Earth and Planetary Science Letters*. The dissertation author was the first author of the published work; coauthors on the publication were Peter Kannberg and Steven Constable. Peter Kannberg aided in data collection and initial processing. Steven Constable supervised the research.

Portions of the text in Chapters 5 and 6, are being prepared for publication. The dissertation author is the first author of the work preparation; the coauthor on the publication is Steven Constable who supervised the research.

VITA

2018	Ph. D. in Earth Sciences, University of California, San Diego
2012	B. S. in Environmental Engineering, University of California, San Diego

PUBLICATIONS

Sherman, D., P. Kannberg, and S. Constable (2017) Surface towed electromagnetic system for mapping subsea Arctic permafrost, *Earth. Planet. Sci. Lett.*, 460, 97-104

Sherman, D. and S. Constable. Permafrost extent on the Alaskan Beaufort shelf from surface-towed CSEM surveys. *in preparation*

Sherman, D. and S. Constable. Stability of marine MT transfer functions, *in preparation*

ABSTRACTS

Sherman,D. and S. Constable. Mapping subsea permafrost using surface-towed electromagnetic methods near Prudhoe Bay, AK. AGU Fall Meeting 2017

Sherman, D., P. Kannberg, and S. Constable. Surface towed CSEM systems for shallow water mapping of Arctic permafrost. 23^{nd} Electromagnetic Induction Workshop, Chiang Mai, Thailand, 2016

Sherman, D., P. Kannberg, and S. Constable. Surface towed CSEM systems for shallow water mapping. AGU Fall Meeting 2015

Sherman, D. and S. Constable. Magnetotelluric sounding used to characterize basin geometry offshore Uruguay as an aid to frontier oil exploration. 22^{nd} Electromagnetic Induction Workshop, Weimar, Germany, 2014

Sherman, D., and S. Constable. Understanding noise in marine magnetotelluric measurements. AGU Fall Meeting 2013

ABSTRACT OF THE DISSERTATION

Surface-towed controlled source electromagnetic system for mapping extent of subsea permafrost on the Beaufort shelf, Alaska

by

Joanna E Sherman

Doctor of Philosophy in Earth Sciences

University of California, San Diego, 2018

Professor Steven C. Constable, Chair

A surface-towed electric dipole-dipole system capable of operating in shallow water and deployable from small vessels has been developed for use in the Alaskan Arctic. Our system uses electromagnetic energy from a modulated manmade source to interrogate the underlying resistivity structure of the seafloor. We used this system in the summers of 2014 and 2015 to map subsea ice-bearing permafrost on the Beaufort Shelf along 200 km of coastline, from Tigvariak Island to Harrison Bay. Permafrost is resistive and was found to be anisotropic, likely due to interbedded layers of frozen and unfrozen sediment. Maps of

depth to permafrost and its thickness were produced from electrical resistivity inversions and results compared to borehole logs in the area. We observed elevated resistivity values offshore the Sagavanirktok River outflow, supporting the idea that fresh groundwater flow has a preserving effect on submerged permafrost. This system provides a cost effective method that could be used to further quantify permafrost extent, provide a baseline for measurements of future degradation, and provide observational constraints to aid in permafrost modeling studies.

Chapter 1

Introduction and Motivation

Conditions favorable to the formation of permafrost have been present in the Arctic since the late Pliocene (1.9 million years), and today permafrost underlies roughly 20% of land in the northern hemisphere (*Collett et al.*, 2011), (Figure 1.1). Permafrost is defined as ground that has been below 0°C for at least two years, in some areas pore fluid freezes and forms ice-bearing permafrost, and in regions of high ice-concentration the sediment grains cement together and form ice-bonded permafrost (*Osterkamp*, 2001). Onshore permafrost can be hundreds of meters thick with only a very thin active layer (order of centimeters) thawing during the summer months. The presence of ice in sediment pore spaces increases both resistivity and seismic velocity, making the combination of ice-bearing and ice-bonded permafrost detectable with geophysical methods.

Over the past 20,000 years, since the last glacial maximum, sea level has risen roughly 100 m, submerging low lying tundra with underlying permafrost. Compared to sub-freezing arctic air temperatures, ocean water imposes a relatively warm and saline

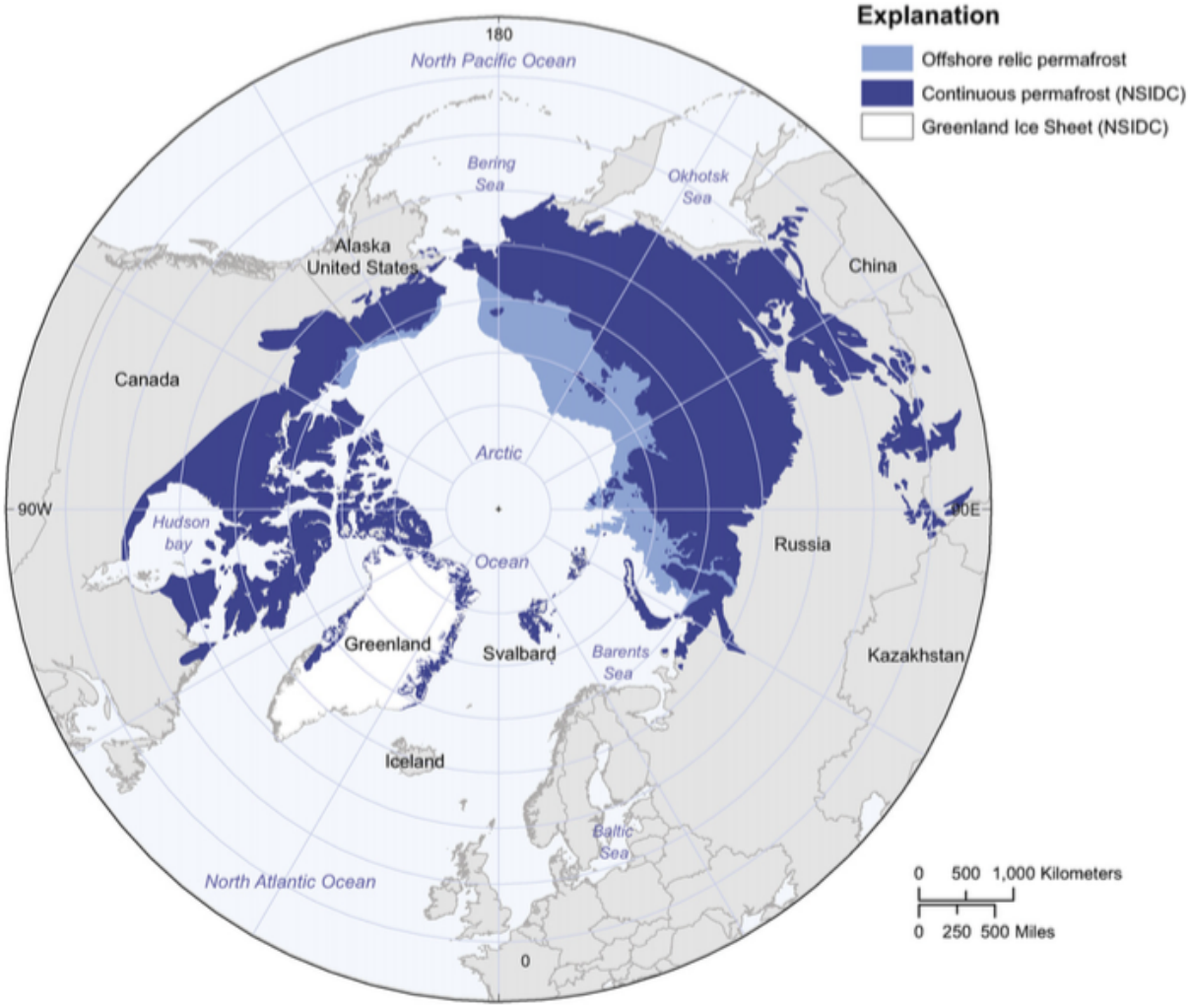

Figure 1.1: Map of permafrost in the Northern hemisphere, onshore (dark blue) and offshore (light blue), taken from (*Collett et al.*, 2011)

boundary condition on submerged permafrost that leads to its continued degradation instead of its formation. Figure 1.2 presents a schematic explaining the main mechanisms by which relict subsea permafrost degrades and an initial temperature profile through the frozen layer. Average ocean temperatures are below 0°C in the Arctic while average air temperatures are closer to -10°C, in freshly submerged permafrost the temperature gradient through the frozen layer will be approximately linear increasing from -10°C to 0°C at

permafrost's base. At the top boundary there are two forces at play that cause top-down thawing of the permafrost layer: conduction of heat and saline intrusion due to density driven convection (*Harrison and Osterkamp*, 1978). Beneath the permafrost layer there is an increase in temperature gradient, resulting in heat input from the geothermal gradient that causes bottom-up thawing of the permafrost layer (*Lachenbruch et al.*, 1982). Local hydrology also affects the extent of permafrost offshore, fresh groundwater can freshen pore fluids and heat input from large rivers can prevent permafrost formation beneath their beds (*Frederick and Buffet*, 2015, 2014).

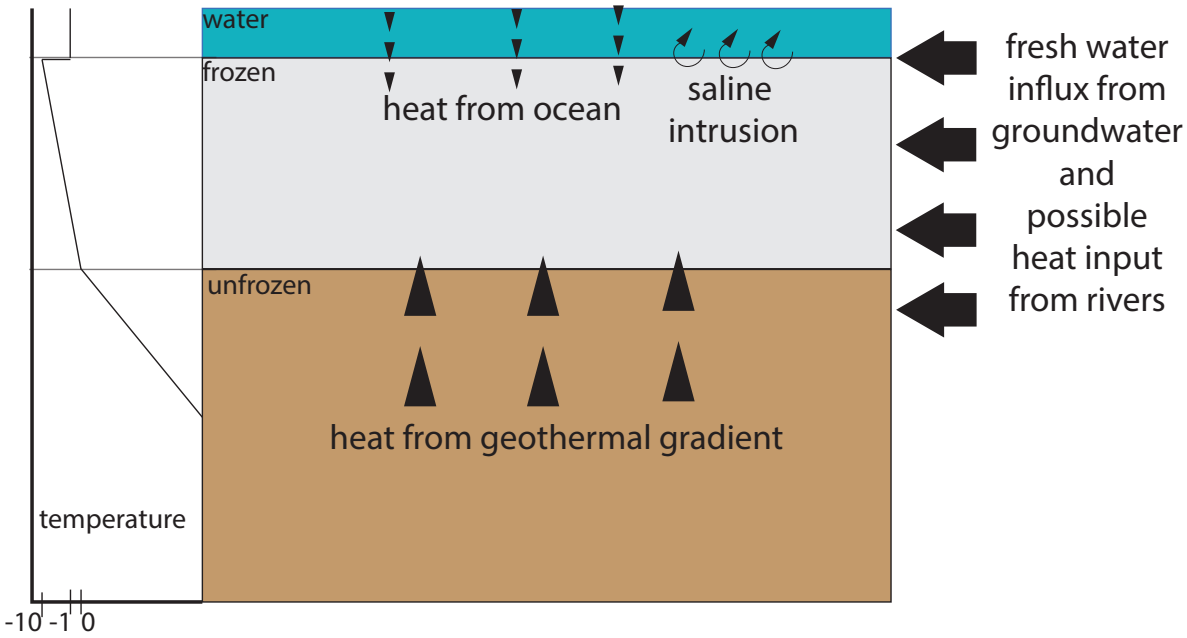

Figure 1.2: Schematic of a temperature profile through newly submerged permafrost and the main systems affecting relict subsea permafrost's degradation.

While relict subsea permafrost constitutes only a small percentage of global permafrost, submerged permafrost is more climatically unstable than its onshore counterpart (*Ruppel*, 2011). Much of the permafrost in existence today is thousands of years old,

as it warms and microbial activity resumes the stored carbon can be released and reach the atmosphere. In addition to organic carbon stored in permafrost, there are potential gas hydrates associated with ice-bearing permafrost (e.g., *Judge and Majorowicz*, 1992; *Romanovskii et al.*, 2005; *Collett et al.*, 2011). Gas hydrate occurs when gas (primarily methane) is trapped in ice crystals at high pressures and low temperatures. Hydrates are normally found under several hundred meters of water in shallow seafloor sediment, but permafrost extends the gas hydrate stability zone to land and shallow water. As the relict permafrost thaws it changes the gas hydrate stability zone, allowing underlying hydrate to dissociate and release methane, a potent greenhouse gas, which in shallow waters is likely to reach the atmosphere. Mapping permafrost extent now will allow future measurements to detect changes and monitor degradation. A map of current state of subsea permafrost will also provide a map of the gas hydrate stability zone.

Current understanding of offshore permafrost is based on seismic data (*Brothers et al.*, 2012; *Brothers et al.*, 2016; *Hunter et al.*, 1992, e.g.,) and boreholes (e.g., *Osterkamp and Payne*, 1981; *Ruppel et al.*, 2016; *Collett et al.*, 1989). Boreholes are very useful for ground-truthing geophysical surveys, but they only provide data at discrete points. Seismic data provide information over a greater spatial area, but are sensitive to strong impedance contrasts and cannot easily identify the bottom permafrost boundary. Electromagnetic (EM) methods are complementary to other geophysical techniques; their diffusive nature makes their resolving power less than for seismic refraction or reflection methods, but they are sensitive to bulk resistivity and can therefore say more about the total ice volume and thickness of permafrost.

Understanding lateral variations in permafrost due to taliks, unfrozen sections in otherwise continuous permafrost, and vertical variations due to lithology will significantly influence the baseline presence and future state as ocean warming continues, and will help us better constrain models of its future evolution. Previous modeling of permafrost degradation and methane hydrate extent has been based on a uniform layer of permafrost (*Frederick and Buffet*, 2015, 2014). While it is generally known this is not accurate, there has been no comprehensive survey determining the true lateral variation of subsea relict permafrost.

Due to the nominal 100 m sea level rise, and since the ocean presents a consistently warm and saline boundary condition compared to the sub-freezing Arctic air temperatures, the maximum extent that relict subsea permafrost could extend offshore is the 100 m isobath, shown in light blue in Figure 1.1. Recent studies, however, suggest the edge of subsea permafrost on the Alaskan Beaufort shelf is much closer to shore and does not extend beyond the 20 m isobath (*Brothers et al.*, 2012; *Brothers et al.*, 2016). The objective of this thesis is to develop a surface-towed controlled-source electromagnetic (CSEM) system capable of operating in the shallow waters of the Arctic Shelf and use this system to map the thickness and lateral variation of relict subsea permafrost on the Alaskan Beaufort Shelf.

Bibliography

Brothers, L. L., P. E. Hart, and C. D. Ruppel (2012), Minimum distribution of subsea ice-bearing permafrost on the U.S. Beaufort Sea continental shelf, *Geophys. Res. Lett.*, *39*, L15501.

Brothers, L.L., B.M. Herman, P.E. Hart, and C.D. Ruppel, (2016), Subsea ice-bearing permafrost on the U.S. Beaufort Margin: 1. Minimum seaward extent defined from multichannel seismic reflection data, *Geochem. Geophys. Geosyst.*, *17* 4354-4365

Collet, T. S., L.W. Myung, W. F. Agena, J. J. Miller, M. V. Lewis, R. Boswell, T. L. Inks (2011) Permafrost-associated natural gas hydrate occurrences on the Alaskan North Slope, *Mar. Pet. Geol.*, *28*, 279-294

Collett, T.S., K.J. Bird, K.A. Kvenvolden, and L.B. Magoon (1989), Map showing the depth to the base of the deepest ice-bearing permafrost as determined from well logs, North Slope, Alaska: USGS Oil and Gas Investigations Map 222.

Frederick, J. M., and B. A. Buffett (2015), Effects of submarine groundwater discharge on the present-day extent of relict submarine permafrost and gas hydrate stability on the Beaufort Sea continental shelf. *J. Geophys. Res. Earth Surf.*, *120*, 417432

Frederick, J. M., and B. A. Buffett (2014), Taliks in relict submarine permafrost and methane hydrate deposits: Pathways for gas escape under present and future conditions, *J. Geophys. Res. Earth Surf.*, *119*, 106 -122

Harrison, W.D., T.E. Osterkamp, (1978) Heat and mass transport processes in subsea permafrost 1. An analysis of molecular diffusion and its consequences. *J. Geophys. Res.*. *83*(C9) 4707-4712

Hunter, J.A., K.G. Neave, H.A. MacAulay and G.D. Hobson. (1978) Interpretation of subseabottom permafrost in the Beaufort Sea by seismic method.. *In*Proceedings, Third International Conference on Permafrost. National Research Council, Ottawa, p. 514-520

Judge, A.S. and J.A. Majorowicz. (1992) Geothermal conditions for gas hydrate stability in the Beaufort-Mackenzie area: the global change aspect. *Paleogeogr. Paleoclimatol. Paleoecol. (Global Planet. Change Sect. 98* p. 251-263

Lachenbruch, A.H., J. H. Sass, B.V. Marshall, and T.H. Moses, Jr. (1982) Permafrost, heat flow, and the geothermal regime at Prudhoe Bay, Alaska. *J. Geophys. Res.*, *87* (B11) 9301-9316

Osterkamp, T. E., (2001) Sub-sea permafrost in Encyclopedia of Ocean Sciences (Second Edition), pp 559-569, Academic Press.

Osterkamp, T.E., and M.W. Payne, (1981) Estimates of permafrost thickness from well logs in northern Alaska. *Cold Reg. Sci. Technol.*, *5* 13-27

Romanovski, N.N., H.W. Hubberten, A.V. Gavrilov, A.A. Eliseeva, and G.S. Tipenko. (2005) Offshore permafrost and gas hydrate stability zone on the shelf of East Siberia Seas. *Geo-Mar. Lett. 25* p. 167-182

Ruppel, C.D. (2011) Methane Hydrates and Contemporary Climate Change. *Nature Education Knowledge*, 3(10):29

Ruppel, C.D., B.H. Herman, L.L. Brothers, and P.E. Hart (2016) Subsea ice-bearing permafrost on the U.S. Beaufort Margin: 2. Borehole constraints, *Geochem. Geophy. Geosy.*, *17*, 4333-4353. doi:10.1002/2016GC006582.

Chapter 2

Background and Theory

2.1 Electromagnetic methods

Electromagnetic methods can be used in a variety of ways to infer the conductivity of Earth's subsurface and provide insights into underlying geology when a conductivity contrast is present. A magma body beneath a volcano and porous rock saturated with saltwater are conductive targets in a resistive background, while rock saturated with hydrocarbons, free gas, or freshwater are resistive targets in a conductive background. Mathematically modeling the full complexity of EM data requires iterative numerical solutions, but some fundamental principals are introduced here. A derivation and explanation of these fundamental principals can be found in a variety of other sources [e.g., *Constable* (2007)], and are repeated here for convenience.

Maxwell's equations, along with some important assumptions and constitutive relationships, are used to relate EM field measurements to Earth's conductivity. We will

start with what are often called the pre-Maxwell equations because displacement currents, along with any polarization or magnetization, can be safely ignored for the geophysical application presented in this manuscript:

$$\text{Faraday's Law} \quad \nabla \times \mathbf{E} = -\frac{\partial \mathbf{B}}{\partial \mathrm{t}} \tag{2.1}$$

$$\text{Coulomb's Law} \quad \nabla \cdot \mathbf{E} = \rho_{\mathrm{e}}/\epsilon_0 \tag{2.2}$$

$$\text{Ampere's Law} \quad \nabla \times \mathbf{B} = \mu_0 \mathbf{J} \tag{2.3}$$

$$\text{No monopoles} \quad \nabla \cdot \mathbf{B} = 0 \quad . \tag{2.4}$$

For the above equations $\mathbf{J}$ is current density in Am^{-2}, $\mathbf{E}$ is the electric field in Vm^{-1}, $\mathbf{B}$ is magnetic flux density in Teslas, which we will call the magnetic field because it is what our instruments measure, and $\mathbf{H}$ is the magnetizing field in Am^{-1}.

In a magnetic source and current free region, the following empirical relationships hold: $\mathbf{B} = \mu \mathbf{H}$ where μ is the magnetic permeability of the material and $\mathbf{J} = \sigma \mathbf{E}$ where σ is the medium's conductivity (S/m). These constitutive relationships are not fundamental laws like Maxwell's equations, but the product of observations and experiments. We can rewrite Faraday's and Ampere's laws as

$$\nabla \times \mathbf{E} = -\mu \frac{\partial \mathbf{H}}{\partial t} \tag{2.5}$$

$$\nabla \times \mathbf{H} = \sigma \mathbf{E} \quad . \tag{2.6}$$

We then take the curl of equations 2.5 and 2.6 using the vector identity, $\nabla \times (\nabla \times$

$\mathbf{A}) = \nabla(\nabla \cdot \mathbf{A}) - \nabla^2\mathbf{A}$

$$\nabla(\nabla \cdot \mathbf{E}) - \nabla^2\mathbf{E} = -\mu\frac{\partial}{\partial t}(\nabla \times \mathbf{H}) \tag{2.7}$$

$$\nabla(\nabla \cdot \mathbf{H}) - \nabla^2\mathbf{H} = \sigma(\nabla \times \mathbf{E}) \quad . \tag{2.8}$$

From Maxwell's equations we know that $\nabla \cdot \mathbf{B} = 0$, and in an area with constant σ, the divergence of the electric field is also zero. Equations 2.5 and 2.6 give values for $\nabla \times \mathbf{E}$ and $\nabla \times \mathbf{H}$, respectively, that can be substituted into equations 2.7 and 2.8. With these substitutions, the equations simplify to diffusion equations:

$$\nabla^2\mathbf{E} = \mu\sigma\frac{\partial \mathbf{E}}{\partial t} \tag{2.9}$$

$$\nabla^2\mathbf{H} = \mu\sigma\frac{\partial \mathbf{H}}{\partial t} \quad . \tag{2.10}$$

We then solve these equations for a sinusoidally varying field with an angular frequency ω. This field can be described as $\mathbf{E}(t) = \mathbf{E}_0 e^{i\omega t}$ and $\mathbf{H}(t) = \mathbf{H}_0 e^{i\omega t}$ with time derivatives $i\omega\mathbf{E}$ and $i\omega\mathbf{H}$ respectively. Substituting the time derivatives back into equations 2.9 and 2.10 we obtain

$$\nabla^2\mathbf{E} = i\omega\mu\sigma\mathbf{E} \tag{2.11}$$

$$\nabla^2\mathbf{H} = i\omega\mu\sigma\mathbf{H} \quad . \tag{2.12}$$

We will continue only with equations for the electric field. The same result can be obtained starting from equations of electric field or magnetic field, they are not independent because one can be derived from the other. We choose the electric field because in practice

this is what we measure. We will further simplify by assuming the fields are horizontally polarized and eliminating dependence in two directions, leaving z as the only independent variable.

$$\frac{\partial^2 \mathbf{E}}{\partial z^2} = k^2 \mathbf{E} = 0,$$

where k is a complex wavenumber defined as $k = \sqrt{i\omega\mu\sigma}$. This type of differential equation has solutions in the form $\mathbf{E} = \mathbf{E}_0 \mathrm{e}^{-ikz}$, which describes an exponential decay in field strength with depth. The length over which the decay occurs is characterized by the skin depth, defined as the depth at which the field strength has decayed to $1/e$ or about 37% of its original value,

$$z_s = \sqrt{\frac{2}{\sigma\mu_0\omega}}. \tag{2.13}$$

To get a skin depth in meters we can use the approximation $z_s \approx 500\sqrt{(\rho T)}$, remembering that $\omega = 2\pi/T$ and $\rho = 1/\sigma$ is resistivity in Ωm. Skin depth describes the inherent depth sensitivity of EM methods. Because each frequency attenuates at a different rate, high frequencies are only sensitive to shallow structure while long periods reach deeper into Earth. For example, in a 1 Ωm halfspace the skin depth of a 0.1 Hz signal is about 1500 m while a 0.001 Hz signal reaches 15,000 m depth. The skin depth is only valid in magnetic source free regions with constant conductivity, but is nonetheless a useful tool for understanding the depth penetration of EM methods.

There is an additional factor that comes into play for CSEM soundings. For magne-

totelluric (MT) sounding, a passive EM approach that uses natural variations in Earth's magnetic field as a source, it is assumed that the source is a plane wave. For CSEM soundings the plane wave approximation is not appropriate and source-receiver geometry becomes important. While there are no rigorous mathematics that give an equation similar to skin depth for source-receiver offsets, the conventional wisdom is that a given source-receiver offset can resolve a depth of half its length.

2.1.1 The controlled source electromagnetic (CSEM) method

The CSEM method uses electromagnetic energy from a modulated manmade source to interrogate the underlying resistivity structure. The source signal attenuates in conductive material and is preserved in resistive material, we see from equation 2.13 that skin depth increases with $\sqrt{\rho}$, making CSEM especially sensitive to resistive targets. Both source - receiver offset and broad frequency content of the transmitted waveform (e.g., *Myer et al.*, 2010) provide inherent depth sensitivity; longer periods and offsets reach further beneath the surface, while shorter periods and offsets are only sensitive to the shallower structure.

The motivation to develop the marine controlled source electromagnetic (CSEM) method came from the desire to map shallow seafloor structure, which requires high frequencies or short offsets. High frequencies are attenuated quickly in conductive seawater; therefore in deep water we tow an electric dipole transmitter at depth to maximize coupling with the seafloor. The CSEM method employed for the purposes of this manuscript uses a horizontal electric dipole source and the response of Earth's conductivity structure

to the imposed source is measured on receiver dipoles. Signal from the transmitter approaches the noise floor with increasing source-receiver offset; maximum ranges with high signal to noise ratios (SNR) are often a few kilometers, but can reach 100 km. To fill in the interstation spacing with CSEM data, fixed offset receivers can be towed behind the transmitter. Fig. 2.1 shows a schematic of the CSEM data collection system.

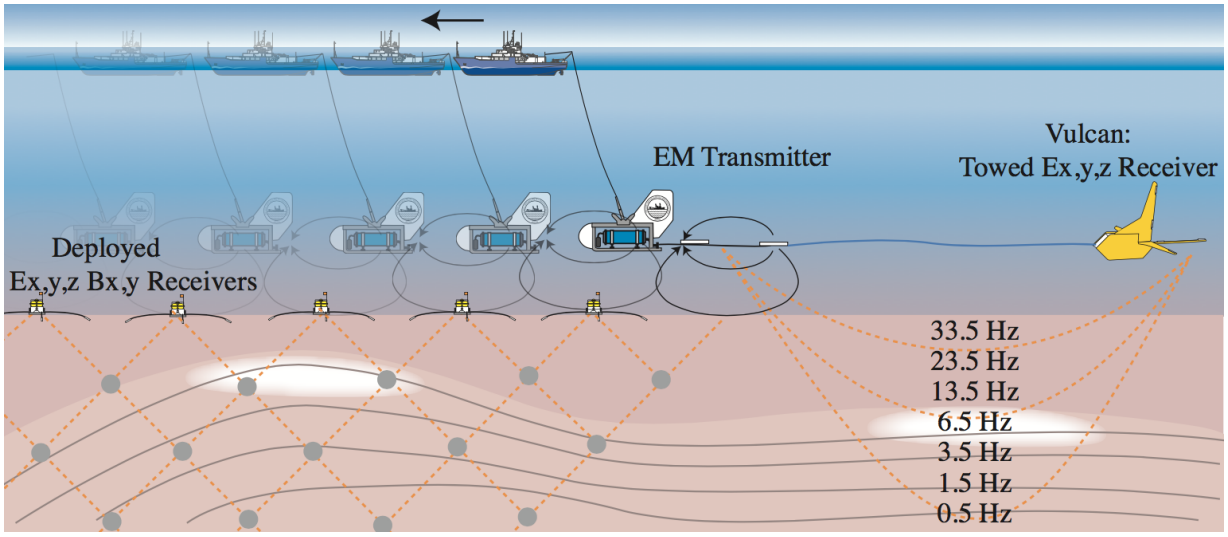

Figure 2.1: Schematic of deep-towed CSEM data collection using seafloor receivers and fixed-offset receivers.

CSEM receivers. Receivers are made in two varieties: seafloor receivers and fixed-offset towed receivers. Seafloor receivers are weighted and anchored at specific locations on the seafloor. They record electric field in two orthogonal directions and are equipped with an external compass to record orientation, which allows us to rotate electric field measurements into inline and crossline components. The biggest source of noise for CSEM data are navigation errors, especially errors in range (source-receiver offset). To fit data to 1% error, navigated positions need to be within 5 m of the truth and within 8° of the correct orientation (*Constable*, 2013). At short offsets, small errors in source or receiver

position result in large relative errors in range and within 3 transmitter dipole lengths the point-source approximation is violated. For these reasons, short offset data when using seafloor receivers are often not useable, which leads to data gaps even when using a very dense grid.

Fixed-offset towed receivers continuously record three-axis electric field data and alleviate the issue of data gaps. Towed receivers are limited in the number and maximum range values they can collect, but for shallow structure we find towing between 4 and 6 receivers in an array up to 1.5 km in length, combined with using multiple frequencies, gives us enough depth sensitivity to resolve structure to 1 km depth. Fixed-offset towed receivers improve navigation because the range is now fixed by a tow cable. Navigating the position of a towed receiver relative to the transmitter is easier than obtaining accurate absolute positions for a towed transmitter and seafloor receivers.

CSEM source instruments. CSEM source signals can be vertical or horizontal electric dipoles or magnetic loops, but in this study we use a horizontal electric dipole transmitter. Our CSEM transmitters rectify AC current and switch it to a low-frequency quasi-square waveform that is applied to an antenna, and seawater is used to complete the circuit. Strength of the output signal (size of the electric field) is determined by the dipole moment of the transmitter given by the length of dipole (L_a) and its output current (I_a). If the transmitter antenna length is 300 m and output current is 350 A the dipole moment is 1.05x10^5 Am, a small transmitter such as the one we will use in Chapter 3 has an antenna length of 45 m with an output of 40 A, giving a dipole moment of 1,800 Am.

Collection of data at multiple frequencies is possible because a square wave can be

decomposed into sinusoids at odd numbered harmonics of the fundamental frequency. We use a more complex double symmetric binary waveform, called waveform-D, that puts more power into higher harmonics and allows for strong signal at a large range of frequencies (*Myer et al.*, 2010). The fundamental frequency typically used for marine CSEM surveys is between 0.25 and 1 Hz and, depending on height above seafloor, we can process up to the 33rd harmonic.

2.1.2 Parametric versus geometric sounding

Until this point, our discussion of CSEM methods has focused on using deep-towed instruments in at least a few hundred meters of water. In this section we assume shallow water (5 m depth) and a surface-towed system that measures inline electric field 0.67 m below the surface of the water at offsets between 250 m and 1,000 m. Though both are fixed-offset receivers, deep-towed and surface-towed receivers will behave differently and results presented here should not be extrapolated to deep-towed instruments.

For MT sounding, frequency is the only parameter affecting depth sensitivity. Skin depth still provides useful information for CSEM sounding, but seems to have less of an effect on resolution than the geometry of the survey design. Choosing which frequencies and offsets to use in a CSEM survey depend on the intended target, and poor choices can result in the inability to resolve the target.

We illustrate differences between parametric sounding (relying on different frequencies for depth sensitivity) and geometric sounding (relying on source-receiver offsets) with some 1D models of a 2-layer permafrost system. The 2-layer permafrost system is based

on well logs showing two distinct frozen layers separated with a conductive layer. Layered models were made assuming 5 m deep water, random gaussian noise added, and the synthetic data inverted with varying frequencies and offsets to determine whether frequency or source-receiver offset dominates the depth sensitivity for the type of marine CSEM sounding used in this manuscript.

Data is inverted with a 1D Occam inversion, which is discussed in detail in the next section. The inversion process works backwards from collected data (in this case electric field data) and tries to determine underlying Earth structure (in this case resistivity of the seafloor) that would explain the observed data. There are many approaches to this problem, the Occam approach searches for the smoothest possible model that fits the data to a specified degree. For details see the next section.

Figure 2.2 on the left shows the results from inverting offsets of 250 m, 500 m, 750 m and 1000 m with one frequency (3 Hz, 13 Hz, or .25 Hz). Using frequencies of 3 Hz or 13 Hz with the four offsets captured the top resistive layer and has some sensitivity to, but is incapable of resolving, the deeper layer. With the lower frequency, .25 Hz, we lose resolution at shallower depths and smooth through the layered structure.

The right side of Figure 2.2 shows the reverse, we now use four frequencies, 1 Hz, 3 Hz, 7 Hz, and 13 Hz, combined with one offset (500 m, 1000 m, or 2000 m). For this model an offset of 500 m is too short, and despite the range of frequencies the data is not sensitive to the target. This is slightly remedied by increasing the frequency range to include 0.1 Hz, 0.25 Hz, 27 Hz, and 33 Hz data, a total of eight frequencies. Longer offsets of 1000 m and 2000 m do a better job of sensing the top resistive layer, though the depth

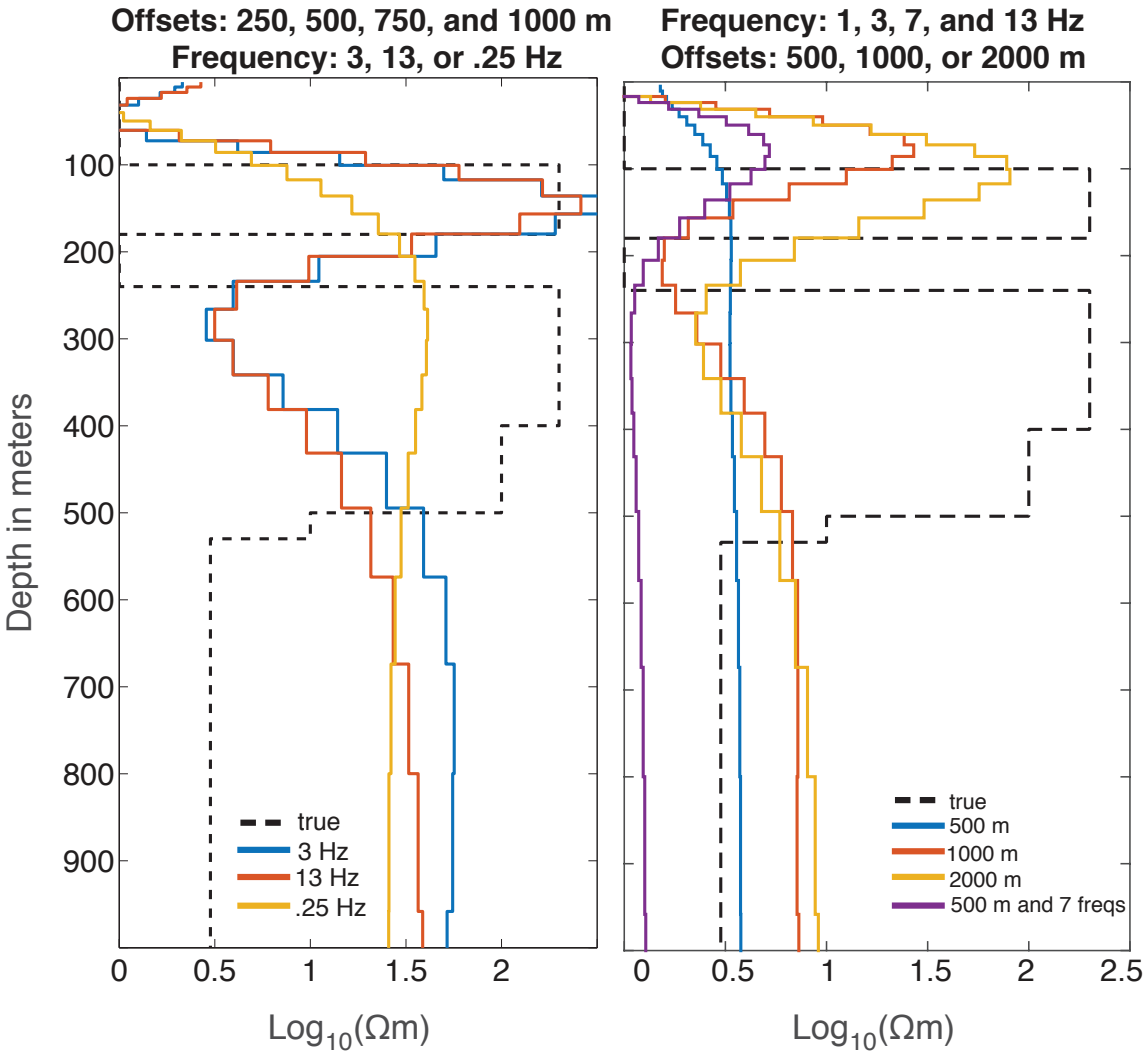

Figure 2.2: Left: Four offsets inverted at three different frequencies. Right: Four frequencies inverted at 3 different offsets. All 1D inversions were isotropic with 3% noise added to the synthetic data.

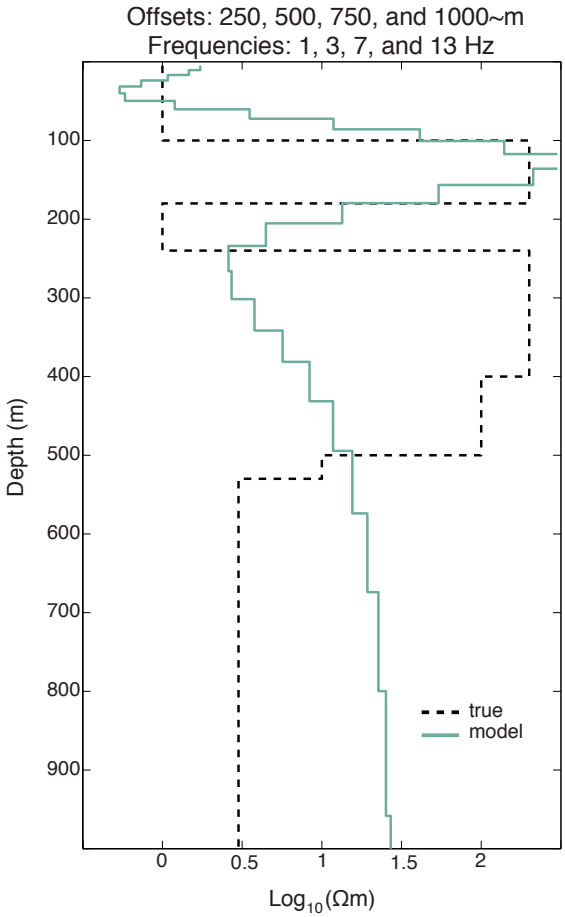

Figure 2.3: Using four frequencies and four offsets for isotropic and anisotropic models.

resolution is still poor and the layer is placed too shallow.

One frequency and one offset is not considered because it was not capable of resolving either permafrost layer. Four frequencies and four offsets, shown in Figure 2.3, resolves permafrost layers about as well as using one frequency with four offsets, indicating that multiple offsets is a more important feature than multiple frequencies for resolving layered structure.

2.1.3 Occam Inversion

The forward problem is one in which we know the conductivity structure of Earth and we calculate the electric field it produces at a given point on the surface. The forward problem changes from 1D (layered Earth) to 2D and 3D model geometry and is often not a trivial problem. It does, however, have a unique solution. The inverse problem attempts to answer the opposite question: given surface measurements of the electric field what conductivity structure produced them? Unlike the forward problem, the inverse problem is non-unique and regularization of the inversion is required to produce reasonable results.

Occam inversion is a variation on the deterministic Gauss-Newton inversion algorithm in which a desired misfit is set by the user and the inversion finds the smoothest model fitting the specified RMS. A brief introduction to Occam's inversion is given here, further details can be found in *Constable et al.* (1987). Occam typically converges quickly, produces smooth models, and gives a sense of convergence to the inverse problem. We want to minimize the functional U, which is a combination of data misfit and a penalty for rough models:

$$U = ||\partial \mathbf{m}||^2 + \mu^{-1}[||\mathbf{W}(\mathbf{d} - F(\mathbf{m}))||^2 - \chi_*^2], \tag{2.14}$$

where $\mathbf{m} \in E^N$ is a vector of model parameters in Euclidean space with dimension N, $\mathbf{d} \in E^M$ is a vector of data values in Euclidean space with dimension M, $F(\mathbf{m})$ is a forward functional describing the physics of the problem,$\mathbf{W}$ is a M x M weighting matrix of data errors, and χ_*^2 is the desired misfit. Misfit quantifies the quality of model fit to data and is defined as $\chi^2 = ||\mathbf{Wd} - \mathbf{WF}(\mathbf{m})||^2$, the traditional sum of squares.

The first term, $||\partial \mathbf{m}||^2$, is the smoothing parameter and is often chosen to be the first spatial derivative of the model $\mathbf{m}$. The derivative is approximated using a first difference where ∂ is an N x N matrix; for a 1D layered Earth model $\partial =$

$$\begin{bmatrix} -1 & 1 & 0 & 0 & \dots & 0 \\ 0 & -1 & 1 & 0 & \dots & 0 \\ 0 & 0 & -1 & 1 & \dots & 0 \\ & & & \ddots & \ddots & \\ 0 & 0 & 0 & \dots & -1 & 1 \end{bmatrix}$$

Matrix $\mathbf{W}$ is a weighting matrix consisting of $1/\sigma_i$ on the diagonals where σ_i are the standard errors on the data ($\mathbf{d}$): $W = \text{diag}\{1/\sigma_1^2, 1/\sigma_2^2, ...1/\sigma_N^2\}$.

The last term, $\mu^{-1}[||\mathbf{W}(\mathbf{d} - F(\mathbf{m}))||^2 - \chi_*^2]$, is the misfit multiplied by the inverse of μ. μ is the variable that weights the importance of fitting the data against having a smooth model. High values of μ devalue the data fit and emphasize a smooth model, while low values of μ produce a rougher model and improve the misfit. In a non-Occam inversions χ is minimized and the value of μ is arbitrarily chosen by the user to obtain the "best" model. In an Occam inversion this is reversed, the user chooses the misfit and the algorithm optimizes μ for that misfit. Misfit is a more reasonable choice to make by the user because the data quality and errors are known and a reasonable guess can be made about how well a model can fit the data.

The forward functional, $F(\mathbf{m})$, is a function of the current model and often requires an iterative solution. If $F(\mathbf{m})$ is nonlinear, as it always is for EM, we find the next iterative step by linearizing around the current model. Assuming that $\mathbf{F}$ is differentiable around

$\mathbf{m}$, we can write

$$\mathbf{F}(\mathbf{m}_1 + \Delta) = \mathbf{F}(\mathbf{m}_1) + \mathbf{J}_1\Delta + \epsilon, \tag{2.15}$$

where $\mathbf{J}$ is the Jacobian matrix given by the gradient of the current model: $J_{ij} = \frac{\partial F_i(m)}{\partial m_j}$ and ϵ is a remainder term of order $||\Delta||$. If we drop the remainder ϵ and define $\Delta = \mathbf{m}_2 - \mathbf{m}_1$, where $\mathbf{m}_2$ is now the model vector we will solve for, we can substitute (2.15) into our expression for U to obtain

$$U = ||\partial\mathbf{m}_2||^2 + \mu^{-1}[||\mathbf{W}(\mathbf{d} - F(\mathbf{m}_1) + \mathbf{J}_1\mathbf{m}_1) - \mathbf{W}\mathbf{J}_1\mathbf{m}_2||^2 - \chi_*^2]. \tag{2.16}$$

We can then solve for $\mathbf{m}_2$ and if we define $\mathbf{d}_1$ as $\mathbf{d} - \mathbf{F}(\mathbf{m}_1) + \mathbf{J}_1\mathbf{m}_1$ then we can write:

$$\mathbf{m}_2 = [\mu\partial^T\partial + (\mathbf{W}\mathbf{J}_1)^T\mathbf{W}\mathbf{J}_1]^{-1}(\mathbf{W}\mathbf{J}_1)^T\mathbf{W}\mathbf{d}_1. \tag{2.17}$$

The final step to determine our new model, $\mathbf{m}_2$, is to select μ. This happens in two parts; if the desired misfit has not been reached then a line search is conducted to find the μ producing the minimum misfit. If the desired misfit has been achieved then there will be two choices of μ that produce a model with a misfit of χ_*^2 and we will choose the smoother of these two models (model with a larger μ).

Including higher dimensions and anisotropy in model space. The Occam framework described here is general and not limited to 1D model space. The model and data vectors can be made to be any length to accommodate higher dimension models; the user just needs to keep track of how to map the vectors back to the higher dimension model space. For example, a 2D model with L x K parameters would have a model vector $\mathbf{m}$ with a length of $N = L * K$.

The same is true for including anisotropy in inversions. Electrical anisotropy allows for directionally dependent values of resistivity, which means one model element could contain up to three values of resistivity. Electrical anisotropy can be due to alignment of crystals (microscopic) that allows current to flow easier in one direction or due to layering (macroscopic) when current can flow horizontally in a conductive layer, but not vertically. When accounting for anisotropy, conductivity ceases to be a scalar value and is instead represented as a tensor with values only on its diagonal:

$$\sigma = \begin{bmatrix} \sigma_x & 0 & 0 \\ 0 & \sigma_y & 0 \\ 0 & 0 & \sigma_z \end{bmatrix}$$

Where σ is conductivity of an element, y is along strike (inline) distance, x is the crossline direction, and z is the vertical direction (depth). Triaxial anisotropy allows $sigma_x$, σ_y, and σ_z to all be different. Transverse anisotropy allows for two resistivity values in each model element, so two elements of the conductivity tensor will be equal and the third will differ, most commonly $\sigma_x = \sigma_y$, σ_z. This situation is transverse vertical anisotropy (also referred to as transverse isotropy), inversions allowing for transverse vertical anisotropy produce two values in each model element: horizontal resistivity (R_y) and vertical resistivity (R_z).

For a 1D model with L layers this would result in a model vector of length $N = 2L$. The smoothing term discussed previously, $||\partial \mathbf{m}_2||^2$, is no longer sufficient. We will call the new smoothing matrix $\mathbf{R}$ such that the smoothing term is now written $||\mathbf{Rm}||^2$ where $\mathbf{R}$ is now a $3L$ x $2L$ matrix. $\mathbf{R}$ is a concatenation of the first difference derivative approximation of $||\partial \mathbf{m}_2||^2$ for both R_y and R_z and the difference between R_y and R_z. For a simple

anisotropic four layer model the matrix $\mathbf{R}$ would be:

$$\mathbf{R} = \begin{bmatrix} -1 & 1 & 0 & 0 & 0 & 0 & 0 & 0 \\ 0 & -1 & 1 & 0 & 0 & 0 & 0 & 0 \\ 0 & 0 & -1 & 1 & 0 & 0 & 0 & 0 \\ 0 & 0 & 0 & 0 & -1 & 1 & 0 & 0 \\ 0 & 0 & 0 & 0 & 0 & -1 & 1 & 0 \\ 0 & 0 & 0 & 0 & 0 & 0 & -1 & 1 \\ -p & 0 & 0 & 0 & p & 0 & 0 & 0 \\ 0 & -p & 0 & 0 & 0 & p & 0 & 0 \\ 0 & 0 & -p & 0 & 0 & 0 & p & 0 \\ 0 & 0 & 0 & -p & 0 & 0 & 0 & p \end{bmatrix}$$

The difference between horizontal and vertical resistivities is weighted by the anisotropic penalty weight p in the smoothing matrix. Low values of p result in low penalty for anisotropy and allows the model to have very different values of vertical and horizontal resistivity in the same model element. High values of p introduce strong penalties as the model moves away from the isotropic model. The anisotropic penalty weight is a user chosen value, and often multiple models with different degrees of anisotropy can be found. Anisotropic models therefore create an additional element of subjectivity in model interpretation (*Constable et al.*, 2015).

2.2 History of using EM methods to map permafrost

The majority of surveys using electromagnetic methods to map permafrost have employed a CSEM approach. These have been done on land by *Hoekstra* (1978) who mapped discontinuous permafrost to help build the Alyeska pipeline, *Daniels et al.* (1976) made multiple soundings along the Alaskan coast, *Todd and Dallimore* (1998) mapped permafrost across the Mackenzie River delta, and *Minsley et al.* (2012) used airborne electromagnetic data to image discontinuous permafrost in the Yukon.

Similar techniques have been employed to measure offshore permafrost by drilling through sea ice during the winter to make soundings. This was done by *Koshurnikov et al.* (2016) over the permafrost table in the Laptev Sea and by *Edwards et al.* (1988) near the Prudhoe Bay area. Direct current (DC) methods have also been used in Alaska to map permafrost in Elson Lagoon near Barrow (*Overduin et al.*, 2012).

Daniels et al. (1976) describes resistivity ratios between frozen and unfrozen ground between 10 and 1000 Ωm, for fine-grained and coarse-grained rock respectively. They also distinguish between two idealized cases, in the first case the permafrost is laminated and made up of many layers of frozen and unfrozen sediment, and in the second case is one massive layer with a sharp transition at the base (*Daniels et al.*, 1976). Of these two, only the laminated case would produce an anisotropic layer.

Across the Mackenzie River Delta, Canada, permafrost resistivity values were found to be between 30 and 300 Ωm for ice-bonded permafrost, between 10 and 40 Ωm for ice-bearing permafrost and sediment less than 10 Ωm. Inverted airborne EM data yield

resistivity values for frozen sections ranging from hundreds to thousands of Ωm (*Minsley et al.*, 2012).

In the subsea environment *Overduin et al.* (2012) used DC resistivity inversions from Elson Lagoon identified resistivities as high as 200 Ωm. The other two offshore EM soundings used time-domain EM methods, which result in discrete soundings instead of the continuous 2D profiles collected by the frequency domain method used in this manuscript, and are collected through holes on winter sea-ice. One survey was done by *Koshurnikov et al.* (2016) offshore Siberia and found the permafrost layer to have a resistivity between 300 Ωm and 500 Ωm, depending on sediment grain size. Lastly, the ICE-MOSES experiment tested a vertical transmitter system during winter offshore Prudhoe Bay, AK. With a maximum of 300 m source-receiver offset they were able to detect the top of permafrost and noted macro-anisotropy in well logs and their phase data, but were unable to accurately capture its true value due to unexpected power line noise (*Edwards et al.*, 1988).

Well logs have been collected onshore and offshore in the Prudhoe Bay area during oil exploration decades ago. Many of these measured resistivity through the permafrost layer and beneath. Values of resistivity within frozen sections varied from 10's of Ωm to over 2,000 Ωm (*Osterkamp and Payne* , 1981; *Collett et al.*, 1989; *Ruppel et al.*, 2016).

2.2.1 How interstitial ice affects bulk sediment properties

As indicated by the studies summarized above, permafrost is a resistive target. Factors affecting resistivity include porosity, salinity of pore fluid, and moisture saturation.

Assuming a fully saturated rock, replacing pore fluid with ice increases its resistivity, this is described mathematically below.

The model of *King et al.* (1988) idealizes unconsolidated permafrost as a matrix of spherical quartz grains, ice, and water. It was found that ice first starts forming in larger pore spaces and progressively freezes into smaller pore spaces as temperature continues to decrease. The total volume of ice formed depends temperature, water content, pore shapes and sizes, pore-water chemistry, and stress state of sediment and pore fluid. Archie's law for resistivity can be used to model the effect of freezing pore fluids on resistivity,

$$R = aR_w\phi^{-m}S_w^{-n}$$

where R_w is pore fluid resistivity, S_w is water saturation, ϕ is porosity, and a, m, and n are empirically determined constants. As water in the pore spaces freezes S_w decreases because ice is replacing water and R_w decreases because ions are excluded from the forming ice. The ratio of resistivity of a partially frozen sample (R_f) to its previous unfrozen state (R_i) is equal to $S_w^{(1-n)}$, which shows resistivity increasing with ice content. This equation is used to convert resistivities to ice saturations in the discussion section.

In summary, we take advantage of the bulk resistivity increase caused by replacing pore water with ice and use the resistivity contrast between frozen sediment and unfrozen sediment to image ice-bearing permafrost. To this end we use a surface-towed controlled-source electromagnetic system that measures inline electric field at four offsets (250 m, 500 m, 750 m and 1000 m) over frequencies ranging from 1 Hz to 33 Hz. Short offsets and high frequencies give us sensitivity to shallow sediment while long offsets and low

frequencies are sensitive to deeper sediment. We use our data, complex electric field measurements represented as amplitude and phase, as inputs to an inversion algorithm. The inversion mathematically finds the smoothest (simplest) model of resistivity structure (depth and thickness of frozen layers) that explains the collected data. The following chapters will discuss the survey area, provide more details on the surface-towed system, and present model results from the inversion process.

Bibliography

Collett, T.S., K.J. Bird, K.A. Kvenvolden, and L.B. Magoon (1989), Map showing the depth to the base of the deepest ice-bearing permafrost as determined from well logs, North Slope, Alaska: USGS Oil and Gas Investigations Map 222.

Constable, S., R. L. Parker, and C. Constable (1987) Occam's inversion: A practical algorithm for generating smooth models from electromagnetic sounding data. *Geophysics 52*(3) 289-300.

Constable S., (2007). Geomagnetism, in Treatise on Geophysics, *5.7*, 237-276

Constable, S.C. (2013) Review paper: Instrumentation for marine magnetotelluric and controlled source electromagnetic sounding, *Geophys. Prospect.*, *62* 573-593

Constable, S. C., A. Orange, and K. W. Key (2015) And the geophysicist replied:"Which model do you want?", *Geophysics*, *80*(3) 197-212

Daniels, J. J., G.V. Keller, J.J. Jacobson. (1976). Computer-assisted interpretation of electromagnetic soundings over a permafrost section. *Geophysics. 41*(4) 752-765

Edwards, R.N., P.A. Wolfgram, and A.S. Judge. (1988). The ICE-MOSES experiment: mapping permafrost zones electrically beneath the Beaufort Sea. *Mar. Geophys. Res.. 9* 265-290

Hoekstra, P., (1978). Electromagnetic methods for mapping shallow permafrost. *Geophysics. 43*(4) 782-787

King, M.S., R.W. Zimmerman, R.F. Corwin (1988) Seismic and electrical properties of unconsolidated permafrost, *Geophys. Prospec.*, *36*, 349-364

Koshurnikov, A.V., V.E. Tumskoy, N.E. Shakhova, V.I. Sergienko, O.V. Dudarev, A.Y. Gunar, P.Y. Pushkarev, I.P. Semiletov, and A.A. Koshurnikov. (2016). The first ever application of eletromagnetic sounding for mapping the submarine permafrost table on the Laptev Sea Shelf. *Geophysics. 469*(2) 860-863

Minsley, B.J., J.D. Abraham, B.D. Smith, J.C. Cannia, C.I. Voss, M.T. Jorgenson, M.A. Walvoord, B.K. Wylie, L. Anderson, L.B. Ball, M. Deszcz-Pan, T.P. Wellman, and T.A. Ager. (2012). Airborne electromagnetic imaging of discontinuous permafrost. *Geophys. Res. Lett.. 39* L02503

Myer, D., S. C. Constable, K. W. Key (2010), Broad-band waveforms and robust processing for marine CSEM surveys. *Geophys. J. Int.*, *184*, 689-698.

Osterkamp, T. E., and M.W. Payne. (1981) Estimates of permafrost thickness from well logs in northern Alaska. *Cold Reg. Sci. Technol.*, textit5, 13-27

Overduin, P.P., S. Westermann, K. Yoshikawa, T. Haberlau, V. Romanovsky, and S. Wetterich. (2012). Geoelectric observations of the degradation of nearshore submarine permafrost at Barrow (Alaskan Beaufort Sea). *J. Geophys. Res.. 117* F02004

Ruppel, C.D., B.H. Herman, L.L. Brothers, and P.E. Hart (2016) Subsea ice-bearing permafrost on the U.S. Beaufort Margin: 2. Borehole constraints, *Geochem. Geophy. Geosy.*, *17*, 4333-4353. doi:10.1002/2016GC006582.

Todd, B.J., and S.R. Dallimore. (1998). Electromagnetic and geological transect across permafrost terrain, Mackenzie River delta, Canada. *Geophysics. 63*(6) 1914-1924

Chapter 3

Survey Area

Our survey area is the Alaskan Beaufort Shelf from Harrison Bay in the west to east of the Sagavanirktok River outflow, a span of about 200 km of coastline. The area is located on the Arctic Alaska plate, which is composed of a metasedimentary (aged Precambrian to Middle Devonian) and volcanic rock basement overlain by various sedimentary sequences (*Bird and Bader*, 1987). All known and inferred gas hydrate reservoirs are found in the Brookian sequence (*Collett et al.*, 2011), a passive margin sequence (Cretaceous and Tertiary aged) mostly from orogenic highlands of the Brooks Range to the south (*Bird and Bader*, 1987). Interest in this area began in the 70's after oil was discovered and production plans began. Emphasis on the study of permafrost in this area has therefore been through the lens of production and most of the data available comes from boreholes and well logs drilled onshore for production purposes. Comparatively little is known about the offshore environment, but as concerns about climate change and interest in exploring offshore increase, the offshore extent and degradation rate of permafrost become more

relevant.

The Beaufort shelf is 80-100 km wide and shallow, maintaining water depths of less than 20 m up to 20 km offshore. Shallow water combined with a relatively recent inundation history gives rise to the possibility of extensive relict subsea permafrost offshore. The entire North Slope, including parts of the Beaufort Shelf, were exposed to freezing subaerial temperatures during the late Pleistocene and formed permafrost hundreds of meters thick. In the Prudhoe Bay area this layer of permafrost is anomalously thick, with ice-rich frozen ground routinely extending to depths over 600 m, due to coarse-grained sediment with high porosities (*Collett et al.*, 1989). Permafrost measured to the west of Prudhoe Bay thins to depths less than 300 m near Harrison Bay and in Barrow (*Collett et al.*, 1989), which is consistent with a decrease in porosity and a transition to finer-grained sediment (*Collett et al.*, 1989).

There has been a nominal rise of 100-120 m sea level since the last glacial maximum, about 20,000 years ago. In a paper by *Clark et al.* (2009) they determine the last global sea-level low stand lasted for roughly 5,000 years, which limits the thickness of permafrost formed near the current 100 m isobath to about 300 m (*Osterkamp*, 2001) because the depth to the 0°C isotherm increases with time exposed to subfreezing temperatures. No detailed inundation history of the Arctic Beaufort shelf has been done, but an attempt was made in the neighboring Canadian Arctic (*Hill et al.*, 1985) using radiocarbon-dated peat and peaty clay samples and seismic profiles. In the assessment of *Hill et al.* (1985) there has been a recent sea level rise of 40 m in the last 7,500 years, precluding the presence of Holocene sediments over the shallow portion of the shelf. Instead Tertiary and Quaternary

aged sediments are exposed across our entire survey area.

Our survey area lies almost entirely in the Prudhoe Bay area, bordered by the National Petroleum Reserve, Alaska (NPRA) to the west and the Arctic National Wildlife Refuge (ANWR) on the east. The NPRA is characterized by more shale and finer grained sediments than the coarse grains of the Sagavanirktok formation characteristic of the Prudhoe Bay area. The Colville River is the border separating the NPRA and the Prudhoe Bay area, because the Colville River Delta is diffuse and data we collected in Harrison is offshore part of the delta, it is unclear if sediment in Harrison Bay is finer than Prudhoe Bay. If there are finer sediments in Harrison Bay, we would expect our data to show a smaller resistivity contrast between frozen and unfrozen layers because smaller pore spaces impede ice formation and lower porosity, which increases the bulk resistivity of the fully saturated rock.

Prudhoe Bay is known to have multiple oil and gas deposits and most development in the area is energy related infrastructure. There has been recent, though aborted, interest in exploring prospects offshore. There are therefore some industry well logs, onshore and offshore, available (*Collett et al.*, 1989; *Ruppel et al.*, 2016) that we will use for comparison with our EM results.

3.1 Current understanding of permafrost on the North Slope

Osterkamp and Harrison of the University of Alaska, along with Lachenbruch and others at the USGS, give us a basic understanding of permafrost distribution on the North Slope and a theoretical understanding of its formation and degradation (*Bird and Bader*, 1987; *Lachenbruch et al.*, 1982; *Osterkamp*, 2001; *Osterkamp and Payne*, 1981; *Collett et al.*, 2011, 1989). Most of their work was done in the late 1970s and early 1980s and key components of it is summarized here.

3.1.1 Permafrost distribution from borehole logs

Osterkamp and Payne (1981), were among the first to differentiate between permafrost (defined by temperature conditions) and ice-bearing permafrost (defined by presence of ice). They looked at a total of 150 well logs, about half of which had a detectable base of ice-bearing permafrost, and determined that there is strong lithological control, due to varying thermal conductivity, on permafrost presence. In contrast, tectonic setting, such as folding and faulting, did not exert regional control over ice-bearing and ice-bonded permafrost. For convenience I will refer to a combination of ice-bearing and ice-bonded permafrost using the acronym IBPF.

Three main lithological groups are identified in *Osterkamp and Payne* (1981): the Nanushuk Group, Colville Group, and Sagavanirktok formation. The oldest is the Lower Cretaceous Nanushuk Group made up of sandstones, shales, and conglomerates

with low porosity and permeability. Second is the Colville Group which is similar to Nanushuk Group, but younger, Upper Cretaceous, with higher porosities. Tertiary sediments, poorly consolidated sandstones and shales, of the Sagavanirktok formation have the highest porosities and water content, along with thin upper layer of newly deposited clays, sands and gravels prevalent over the Prudhoe Bay area, and has the most easily recognized IBPF layer. IBPF is thickest in Tertiary sediments of the Prudhoe Bay area and thinnest in Lower Cretaceous sediments further west. Our survey took place over Tertiary sediments of the Sagavanirktok formation, except where we may have crossed into Colville formation when collecting data in Harrison Bay.

Based on the boreholes studies by *Osterkamp and Payne* (1981), there is typically a 10-60 m transition zone at the base of IBPF where frozen and unfrozen pore fluids coexist; this zone is thicker in finer grained sediments. In a few well logs gas hydrate was seen beneath IBPF, where gas was trapped by the impermeable ice-bonded permafrost. In the Sagavanirktok River Delta some boreholes, specifically Gull Island and Niakuk Island, displayed two layers of frozen sediments with what is interpreted to be warm and salty frozen gravel down to 180 m meters, a 30-60 m thick layer of unfrozen sediment with saline pore fluid and resistivities between 1 and 5 Ωm, and then another layer of frozen sediments that is colder and fresher than the top layer.

Tim Collett produced a map of onshore permafrost distribution based on well logs in 1989 (*Collett et al.*, 1989) and concluded that the Prudhoe Bay area was composed of coarse-grained sediment with high porosities and low geothermal gradients consistent with a thick layer of IBPF, while the National Petroleum Reserve Alaska (NPRA), which begins

west of the Colville River, is characterized by finer-grained sediments with low porosity and correspondingly high geothermal gradients within the permafrost layer, indicating a thinner IBPF layer. He looked at all 440 publicly available well logs and determined 156 were able to detect a base of IBPF. In the coarse-grained lithology of the Prudhoe Bay area, thick layers of high saturation IBPF are observed from the surface down to over 600 m and the base of IBPF is very near the 0°C isotherm.

Lachenbruch et al. (1982) observed a discontinuity in geothermal gradient at the base of IBPF due to the presence of ice in the Prudhoe Bay area; this discontinuity is not present further west in the NPRA, and the 0°C isotherm does not coincide with the base of IBPF. A shift in lithology from high porosity sandstones and conglomerates in the Prudhoe Bay area to siltstones and shale in the NPRA is likely responsible for the observed thinning of IBPF to the west of Prudhoe Bay. While shallow shale still has a high porosity, the pore water is ionically bonded to clay which inhibits ice formation. More deeply buried shale is compacted and has lower porosity. *Lachenbruch et al.* (1982) also notes that where permafrost is detected on the North Slope there are often multiple freeze - thaw horizons.

More recently, *Ruppel et al.* (2016) published a companion paper to *Brothers et al.* (2016) using offshore borehole data to constrain permafrost. Resistivity logs from the upper 800 m of 32 boreholes were analyzed as well as temperature and core samples from 20 geotechnical borings. High-saturation ice-bonded permafrost was defined as resistivities >100 Ωm, which is almost certainly detectable by geophysical methods. Intermediate-saturation ice-bonded permafrost, between 10 and 100 Ωm, may be detectable by geophys-

ical methods. Zones of low-saturation ice-bonded permafrost were identified in regions of slightly elevated resistivity not exceeding 10 Ωm; they may contain remnants of ice-bearing permafrost, but are not easily detectable. This data set provides virtually no evidence for permafrost presence beyond the barrier islands, consistent with the seismic surveys, which suggests that the small barrier islands may support permafrost preservation. Data abstracted from this paper are compared to maps of permafrost distribution derived from results of a pilot CSEM survey in the discussion section.

3.1.2 Prior seismic surveys

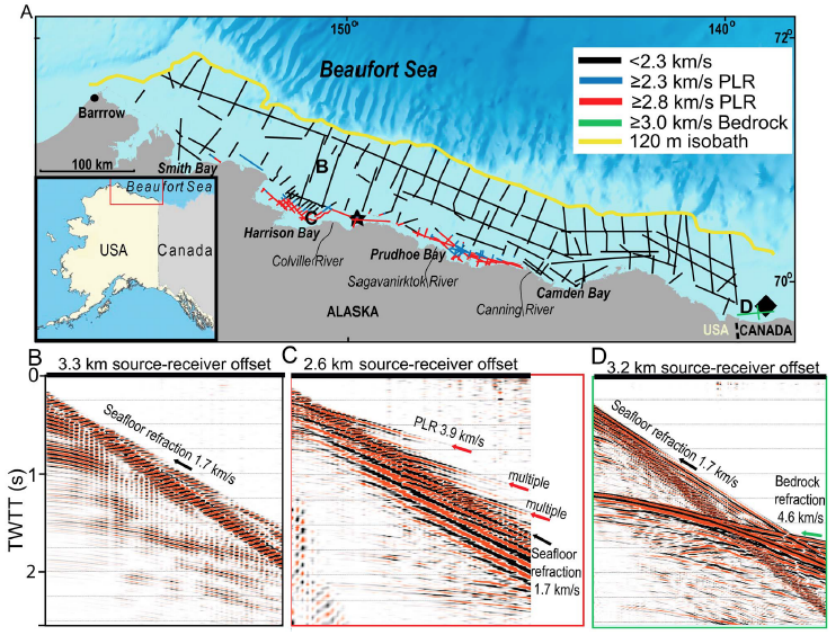

Figure 3.1: A. Map of the Beaufort shelf with seismic lines plotted in red if velocities were >2.8 km/s, blue if velocities were >2.3 km/s, and black when there were no elevated velocities. The presumed coastline before the 120 m rise in sea level is shown in yellow. B. Example of seafloor refraction. C. Example of a permafrost layer refraction and multiples. D. Example of seafloor and bedrock refractions. Figure taken from (*Brothers et al.*, 2012).

There have been a limited number of seismic surveys covering the Beaufort Shelf. *Brothers et al.* (2012) used seismic refraction to determine presence of ice-bonded permafrost using permafrost layer refractions (PLRs), which were not detected beyond the 20 m isobath. This is less permafrost than on the Canadian side of the Beaufort shelf, where permafrost extends nearly to the shelf edge (*Taylor et al.*, 1996; *Morack et al.*, 1983). Additionally, this seismic refraction survey inferred a nearly uniform distribution of ice-bonded permafrost, with the exception of a region of lower saturation ice-bonded permafrost just east of the Sagavanirktok River (*Brothers et al.*, 2012).

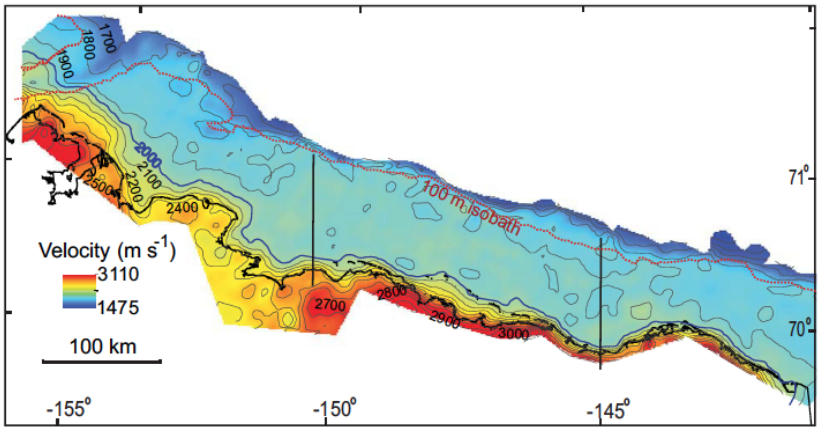

Figure 3.2: Seismic velocity map from (*Brothers et al.*, 2016). 2000 m/s velocity contour considered end of offshore permafrost extent.

A map of the *Brothers et al.* (2012) survey area can be found in Figure 3.1. Seismic velocities greater than 2.8 km/s indicate the presence of ice-bonded permafrost, velocities less than 2.3 km/s indicate no significant presence of ice, and velocities between 2.3 and 2.8 km/s suggest a low saturation of ice-bonded permafrost. These three possibilities are shown in Figure 3.1 in red, black, and blue lines respectively.

The *Brothers et al.* (2012) paper not only suggested that permafrost is limited in

lateral extent offshore, but that in many places the top thawed layer is already hundreds of meters thick. PLRs were seen between 5 and 470 m below the seafloor, with a mean depth of 195 m and standard deviation of 102 m, which implies a more rapid degradation of the relict permafrost than previously thought.

More recently, legacy industry seismic reflection data were reprocessed and used to produce a seismic velocity map, shown in Figure 3.2, that is meant to be a regional-scale picture of permafrost extent with 2 km resolution (*Brothers et al.*, 2016). Seismic velocities fall off sharply away from shore; the 2000 m/s velocity contour is determined to be the edge of detectable permafrost and is consistent with results from the earlier seismic refraction study of *Brothers et al.* (2012).

3.2 The CSEM survey

Our CSEM survey was based out of West Dock in Prudhoe Bay, AK. Field operations were conducted over a two year period, 7 days in late July, 2014 and 10 days in August 2015. Initially we intended to tow five shore-perpendicular lines from the coast past the seismically inferred edge of permafrost; however, in 2014 we were thwarted by the summer sea ice pack which lingered nearshore. We scheduled operations a few weeks later in the season in 2015 in the hopes that the ice pack would be further offshore, but it was in fact closer to shore. Due to the ice barrier, we focused on expanding data coverage along the coast, collecting a dense data set from both years near Prudhoe Bay and the Sagavanirktok River, as well as along the coast to Harrison Bay.

A few moored seafloor receivers were deployed to supplement the towed data with longer offsets in a few locations. Only the locations on Tow 4 proved to be useful because other sites were moved around by ice and occasionally snagged by our own tow line. Though we could record the start and end position of the instruments, we had no way of knowing when they were moved and most of our compasses had limited storage capacity and only recorded orientation once an hour for 18 hours. Without a record of orientation we are limited in the data we can use from these sites.

Previous studies of permafrost in the Alaskan Arctic indicate that the Prudhoe Bay region has thick permafrost (down to nearly 700 m depth) due to it coarse-grained lithology and that the finer-grained sediments further west host less ice-bearing permafrost. We expect trends seen onshore to extend to the offshore environment because subsea per-

mafrost was formed in subaerial conditions. The presence of multiple freeze-thaw horizons, as seen in some well logs, would lead to electrical anisotropy in which vertical resistivity is greater than horizontal resistivity, as introduced in chapter 2. Previous geophysical surveys in this section of the Beaufort Sea infer a limited extent of IBPF on the shelf (within the 20 m isobath), which is less IBPF than measured offshore Canada or Siberia and less than would be assumed on the basis of basic thermal models. Although sea ice prevented us from collecting data beyond the 20 m isobath, the furthest offshore thickness mapped with our CSEM data corroborates the seismic interpretation that there is less IBPF on the Alaskan Beaufort Shelf than previously thought. This is discussed more in chapter 6.

Bibliography

Bird, K.J. and J.W. Bader. (1987) Petroleum geology of the northern part of the Arctic National Wildlife Refuge, northeastern Alaska: Chapter 3: Regional geologic setting and history of petroleum exploration. *USGS Bulletin* 1778

Brothers, L. L., P. E. Hart, and C. D. Ruppel (2012), Minimum distribution of subsea ice-bearing permafrost on the U.S. Beaufort Sea continental shelf, *Geophys. Res. Lett.*, *39*, L15501.

Brothers, L.L., B.M. Herman, P.E. Hart, and C.D. Ruppel, (2016), Subsea ice-bearing permafrost on the U.S. Beaufort Margin: 1. Minimum seaward extent defined from multichannel seismic reflection data, *Geochem. Geophys. Geosyst.*, *17* 4354-4365

Clark, P.U., A.S. Dyke, J.D. Shakun, A.E. Carlson, J. Clark, B. Wohlfarth, J.X. Mitrovica, S.W. Hostetler, and A.M. McCabe. (2009) The last glacial maximum. *Science. 325* 710-714

Collet, T. S., L.W. Myung, W. F. Agena, J. J. Miller, M. V. Lewis, R. Boswell, T. L. Inks (2011) Permafrost-associated natural gas hydrate occurrences on the Alaskan North Slope, *Mar. Pet. Geol.*, *28*, 279-294

Collett, T.S., K.J. Bird, K.A. Kvenvolden, and L.B. Magoon (1989), Map showing the depth to the base of the deepest ice-bearing permafrost as determined from well logs, North Slope, Alaska: USGS Oil and Gas Investigations Map 222.

Hill, P.R., P.J. Mudie, K. Moran and S.M. Blasco (1985) A sea-level curve for the Canadian Beaufort Shelf, *Can. J. Earth Sci.*, *22*(1) 1383-1393

Lachenbruch, A.H., J. H. Sass, B.V. Marshall, and T.H. Moses, Jr. (1982) Permafrost, heat flow, and the geothermal regime at Prudhoe Bay, Alaska. *J. Geophys. Res.*, *87* (B11) 9301-9316

Morack, J.L., H.A. MacAulay, and J.A. Hunter. (1983) Geophysical measurements of sub-bottom permafrost in the Canadian Beaufort Sea. *In* Proceedings, Permafrost, Fourth International Conference, national Academy Press, Washington, D.C., p. 866-871

Osterkamp, T. E., (2001) Sub-sea permafrost in Encyclopedia of Ocean Sciences (Second Edition), pp 559-569, Academic Press.

Osterkamp, T.E., and M.W. Payne, (1981) Estimates of permafrost thickness from well logs in northern Alaska. *Cold Reg. Sci. Technol.*, *5* 13-27

Ruppel, C.D., B.H. Herman, L.L. Brothers, and P.E. Hart (2016) Subsea ice-bearing permafrost on the U.S. Beaufort Margin: 2. Borehole constraints, *Geochem. Geophy. Geosy.*, *17*, 4333-4353. doi:10.1002/2016GC006582.

Taylor, A.E., S.R. Dallimore, and S.I. Outcalt. (1996) Late quarternary history of the Mackenzie- Beaufort region, Arctic Canada, from modeling of permafrost temperatures. 1. The onshore-offshore transition. *Can. J. Earth Sci. 33* p. 52-61

Chapter 4

Methodology

This chapter is the paper describing the surface-towed CSEM system published in EPSL reprinted in full. Some information in the introductory paragraphs is repeated, but for completeness the entire paper is included.

4.1 Introduction and Motivation

Temperatures cold enough to form permafrost have been present in the Arctic since the end of the Pliocene (about 1.9 Ma) and as a result permafrost underlays roughly 20% of land in the northern hemisphere (*Collett et al.*, 2011). Permafrost is defined as ground that has been held at or below 0°C for at least two years, "ice-bearing" specifies that the pore spaces contain a mixture of ice crystals and pore fluid while "ice-bonded" describes cementation of the sediment grains in the permafrost (*Osterkamp*, 2001). For the remainder of the manuscript we will use "permafrost" to describe a combination of

ice-bearing and ice-bonded permafrost.

Over the last 20,000 years sea level has risen 120 m and submerged portions of Arctic coastline and permafrost. The warm, saline conditions introduced by sea level rise are causing the relict subsea permafrost to thaw (*Osterkamp*, 2001). The maximum extent of permafrost offshore, therefore, is the 120 m isobath (*Collett et al.*, 2011), but current seismic studies suggest that permafrost does not extend beyond the 20 m isobath (*Brothers et al.*, 2012). The reason for discrepancy is uncertain (*Collett et al.*, 2011), and a number of offshore measurements of permafrost with simple and effective ways are required.

Permafrost often has associated gas hydrate, which requires low temperature and high pressures to be stable and typically exists beneath the deep ocean floor. However, consistent cold ground temperature in the presence of ice-bearing permafrost allows gas hydrate to currently exist on land and in shallow water environments. Without the permafrost cap to thermally stabilize them, hydrates could dissociate and release their bound methane gas. Methane is a potent greenhouse gas and its release from beneath subsea permafrost would influence current and future warming trends (*Ruppel*, 2011).

A map of our survey area can be found in Figure 4.5. Prior studies conducted on the Beaufort Shelf, Alaska, have used the seismic refraction method to infer extent of permafrost. Seismic refraction uses the increase in P-wave velocity (V_p) due to ice in pore spaces to determine the presence of permafrost. Theory predicts a V_p of 2.5 - 2.8 kms^{-1} for sands with less than 40% ice saturation, and above 40% saturation a sharp jump in seismic velocity to between 3.4 and 4.35 kms^{-1} due to the onset of cementation of sediment grains (*Johansen et al.*, 2003). In the Beaufort Sea velocities varied between 1.7 - 4.6 kms^{-1}

with all permafrost layer refractions (PLRs), defined as $V_p > 2.3$ kms^{-1}, occurring within 30 km of the coast and shallower than 20 m water depth (*Brothers et al.*, 2012).

Although PLRs can be used to define the lateral extent of permafrost, the seismic method has difficulty determining depth boundaries and bulk properties of permafrost (*Brothers et al.*, 2012). The velocity contrast at the top boundary is so large that most of the seismic energy does not propagate beneath it. The bottom permafrost boundary is likely diffuse and is a velocity decrease, both of which result in a weak or non-existent refraction signal. As a consequence, the seismic method can image the top of the permafrost layer at best. Additionally, the refraction method cannot differentiate between frozen and unfrozen fine grained sediments, which means the depth obtained from this method may not be the top of the permafrost layer if fine sediments overly coarse ones (*Brothers et al.*, 2012).

Electromagnetic methods complement seismic data by resolving the top and bottom boundaries, as well as estimating the volume fraction of permafrost (e.g., *Hauck*, 2016; *Todd and Dallimore*, 1998). CSEM is sensitive to the resistivity increase caused by ice forming in pore spaces, as well as to the resistivity decrease below the permafrost as the sediments transition to an unfrozen state. Onshore boreholes have measured ice-bonded permafrost with resistivities from 100 Ωm to over 1000 Ωm to depths of 660 m near the coast of Prudhoe Bay (*Collett et al.*, 1989; *Jorgenson et al.*, 2008). Below the permafrost layer resistivities drop to between 5 and 15 Ωm (*Collett et al.*, 1989). We expect the resistivity of offshore ice-bearing permafrost to be lower than the measured onshore values because of intrusive saline pore fluids (*Daniels et al.*, 1976). Land borehole measurements

of hydrate beneath permafrost in the Eileen accumulation, located near the coastline just west of Prudhoe Bay, reach 2000 Ωm at a depth of about 600 m (*Collett et al.*, 2011). Gas hydrate occurs at greater depths and has a higher resistivity than permafrost, and so with careful interpretation one might be able to distinguish between the two.

4.2 Methodology

Shallow seafloor resistivity, a good proxy of marine geological settings, is effectively mapped using a fixed-offset towed array (e.g., *Constable et al.*, 2016). Towed systems have been used extensively in deep water and are faster to use than deploying seafloor CSEM receivers. However, shallow water depths on the Arctic shelf make using a deep-towed system unfeasible and make a surface towed system more appropriate.

4.2.1 Instrument Design

We had previously developed a deep-towed fixed-offset CSEM system to map gas hydrates, the "Vulcan" system of *Constable et al.* (2016). This design was adapted for a surface-towed system by repackaging our Vulcan deep-tow receivers in buoyant PVC cases. We call the assembly a "Porpoise" since they occasionally appear to leap from the water when encountering ice. The data logger within the plastic case records inline electric field, acceleration in three directions, and a timing pulse sent from an external GPS receiver. Inline electric field is measured using a 2 m dipole held 0.67 m underwater. As with the Vulcan instruments, we chose rigid antennas instead of cable arrays to avoid motional noise

associated with cable motion through Earth's magnetic field (*Constable et al.*, 2016). The Vulcan system is equipped with the ability to receive real-time data and telemetry from the receivers. These features are necessary for maintaining a steady receiver depth, and to prevent unwanted contact with the seafloor, as well as monitoring data quality during tows lasting many days. Neither of these concerns affect Porpoises because their positions can be verified by sight and they are typically only towed for hours at a time, allowing for frequent data quality checks without the real-time capabilities. A schematic of the Porpoise system is shown in Figure 4.1 and pictures of the instrument can be found in Figure 4.2.

GPS receivers are attached to the top of the Porpoises on short masts and a serial data logger within the logger package records time and location. A second serial data logger records pitch, roll, and heading from a compass/tiltmeter every second. Conductivity, temperature, and depth (CTD) were continuously measured in the top meter of sea water by towing a CTD package alongside the vessel. When towing into deeper water, the CTD system was lowered to the bottom once the vessel was stopped and the Porpoises were on deck to measure a conductivity profile. A total of twelve conductivity profiles were collected and reached a maximum depth of 10 m.

The transmitter operates off 110 - 240 VAC power and can output up to 50 A on a 50 m antenna in the form of an arbitrary GPS stabilized ternary waveform. Data were collected over two years, in the first year a 50 m antenna was used with between 30 and 40 amps output. In the second year, the transmitter was upgraded to produce a current controlled output of 40 amps on a 45 m antenna.

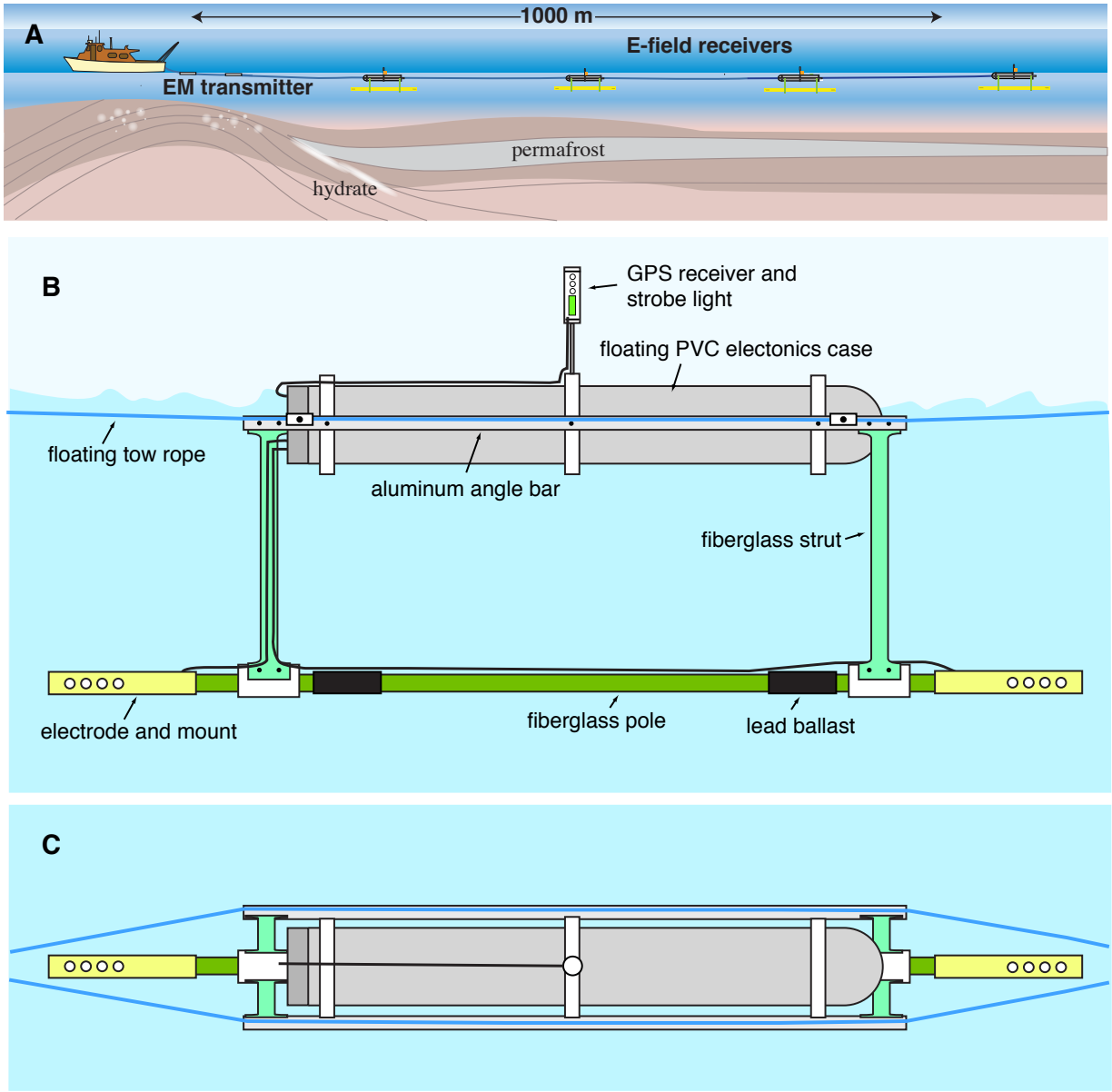

Figure 4.1: A: Surface-towed Porpoise array. Multiple receivers are easily clipped into the tow rope during deployment. B: Side view schematic of a Porpoise receiver. C: Plan view of a Porpoise receiver.

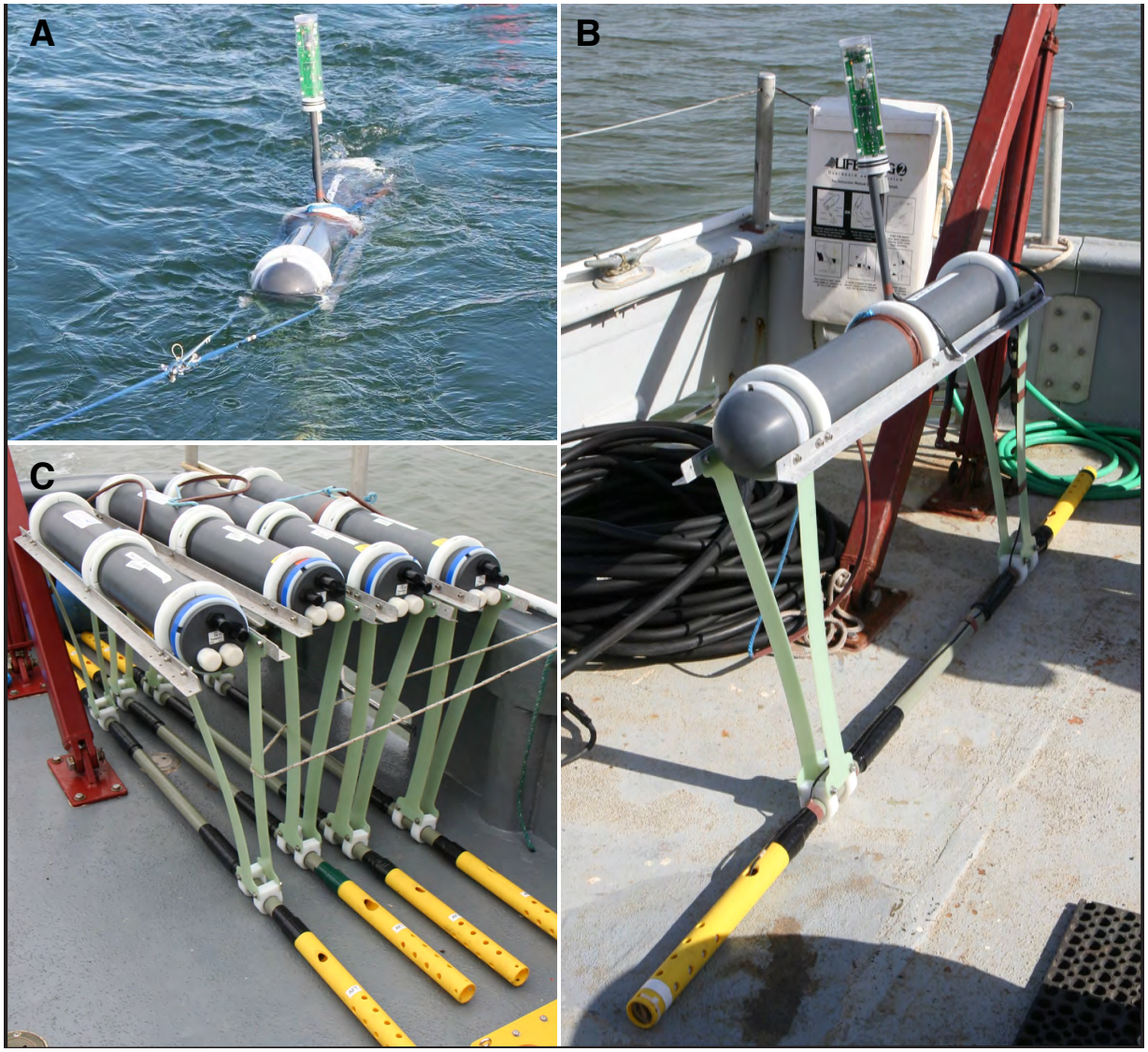

Figure 4.2: A: Porpoise floating on the surface after being deployed. B: Porpoise ready to be deployed. C: All four Porpoises stored on deck, electrodes and GPS receivers still need to be attached.

The entire Porpoise system is light and small enough to be easily air freighted, transported in one load using a utility vehicle, and operated off a small (16 m) fishing boat. This makes it a relatively easy and inexpensive system to operate, and while designed to operate in the shallow Arctic shelf, it has already been used for a number of other applications including groundwater and geothermal exploration in the Atlantic and Gulf of California, respectively (e.g., *Martin*, 2015).

Shown in Figure 4.3 are noise spectra of Porpoises at three offsets compared with published noise spectra of a Vulcan deep-tow instrument and an ocean bottom electromagnetic (OBEM) receiver (*Constable et al.*, 2016). At 1 Hz noise levels are on the order of a few microvolts and at 30 Hz the noise contributes tens of nanovolts. The peak centered around 0.3 Hz is due to wave noise or strumming of the instrument. Porpoise receiver noise is higher than that of the Vulcan because of increased wave and environmental noise on the surface. The noise floor of the OBEM is the lowest because it is subject to fewer motional noise sources.

4.2.2 Sensitivity to target

We conducted synthetic forward modeling to determine the offsets and frequencies most sensitive to permafrost, modeled as a 200 m thick layer of 100 Ωm material buried at a depth of 200 m in 1 Ωm marine sediment. This model was intentionally chosen to be conservative and was constructed based on modeling and well log data (*Osterkamp*, 2001). Forward responses were calculated for the permafrost model as well as a halfspace of pure sediment. In both cases water depth was 5 m and the calculation was done for offsets of

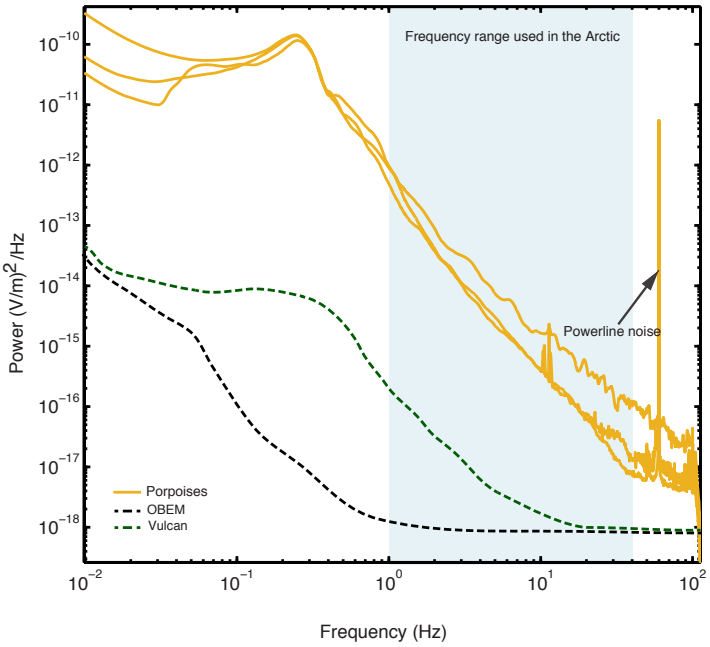

Figure 4.3: Power spectra of various EM receivers. Porpoise data were collected on a test cruise offshore San Diego in May of 2014. Vulcan and OBEM spectra are from *Constable et al.* (2016) and are shown as broken lines.

100 to 1100 m and frequencies of 1 to 40 Hz. Figure 4.4 shows (A) the amplitude of the permafrost model response normalized by the halfspace response and (B) the difference in model phases. Largest sensitivity to a permafrost layer occurs at offsets longer than 500 m and at frequencies less than 30 Hz.

In our survey design Porpoises were towed at offsets of 250, 500, 750 and 1000 m. We find that including a shorter range Porpoise helps constrain the shallow sediment and ultimately helps resolve permafrost in inversions of the data. The array was kept at 1 km in length for logistical reasons, but we experimented with moored seafloor receivers that measured two orthogonal directions of the horizontal electric field. Moored receivers were weighted and marked with a buoy so that they could be deployed and recovered by hand. Source receiver offsets of up to 6 km were obtained using these receivers. We transmitted

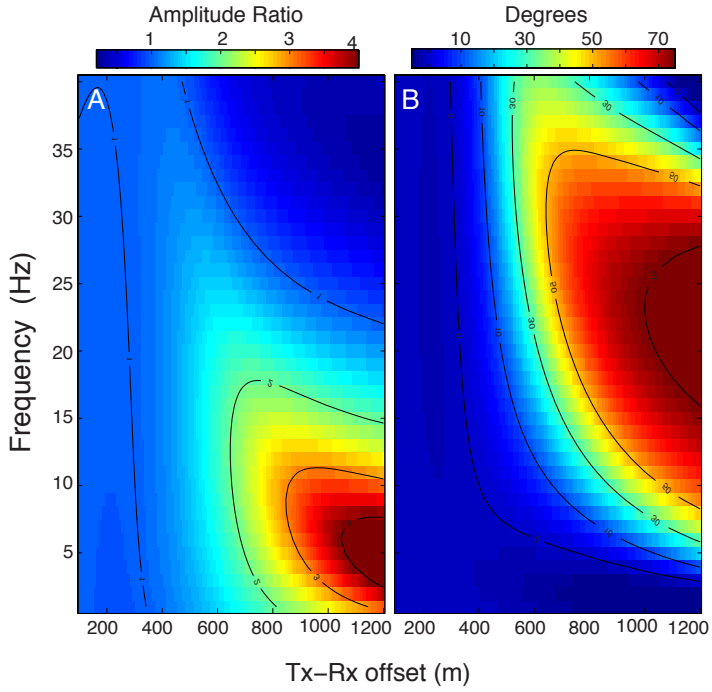

Figure 4.4: A: Amplitude anomaly or permafrost model amplitude normalized by a 1 Ωm halfspace amplitude. An amplitude anomaly of 1 indicates no difference. B: Phase anomaly or phase difference between the two models. The permafrost model was a 200 m thick permafrost layer with 100 Ωm resistivity buried at a depth of 200 m in 1 Ωm sediments.

a 1 Hz fundamental of Waveform-D, a modified square wave that spreads power from the fundamental frequency into higher odd harmonics spanning at least one decade (*Myer et al.*, 2010).

4.3 Survey Area

The surface towed Porpoise system was used in the summers of 2014 and 2015 on the Beaufort Shelf off the north coast of Alaska, with operations based out of Prudhoe Bay on the North Slope. The Beaufort shelf is 80 - 100 km wide with water depths less than 20 m to more than 20 km offshore. The shelf was not glaciated during the

late Pleistocene, rather was exposed to subfreezing temperatures and formed permafrost hundreds of meters thick. Holocene sediments are missing over much of the Beaufort shelf because of the recent (7.5ky) 40 m sea level rise (*Hill et al.*, 1985). Instead, Tertiary and Quaternary sand, silt, and clay make up the bulk of shallow shelf sediments (*Houseknecht and Bird*, 2011). Sedimentary rocks in this region can be divided into 4 sequences: the Franklinian (Cambrian to Devonian), Ellesmerian (Mississippian to Jurassic), Beaufortian (Jurassic-Lower Cretaceous), and Brookian (Cretaceous-Holocene) (*Hubbard et al.*, 1987). All known and inferred gas hydrate on North Slope is found in the Brookian sequence (*Collett et al.*, 2011).

Our surveys were conducted off the R/V Ukpik during late July/early August in 2014 and 2015, shortly after the ice pack broke away from shore. In total we towed 12 days and covered 365 km, on average 30 km per 12-hour day (compare this to 6 km per 24-hour day when using deployed receivers (e.g., *Weitemeyer et al.*, 2006)). Initially the plan was to tow shore perpendicular lines coincident with seismic data collected by the U.S. Geological Survey. However, the annual sea ice pack limited how far offshore we were able to collect data and so instead we focused our efforts on expanding coverage along the shoreline. In 2014 the edge of the sea ice was near the 20 m isobath, where seismic data indicates the edge of the permafrost lies. Although in 2015 we returned later in the season in hopes of collecting data farther offshore, the sea ice was in fact closer to shore and prevented us from towing past the seismically determined edge of permafrost. Harrison Bay was the one location where we successfully collected data across the presumed edge of permafrost. Tow lines for both years are shown in Figure 4.5.

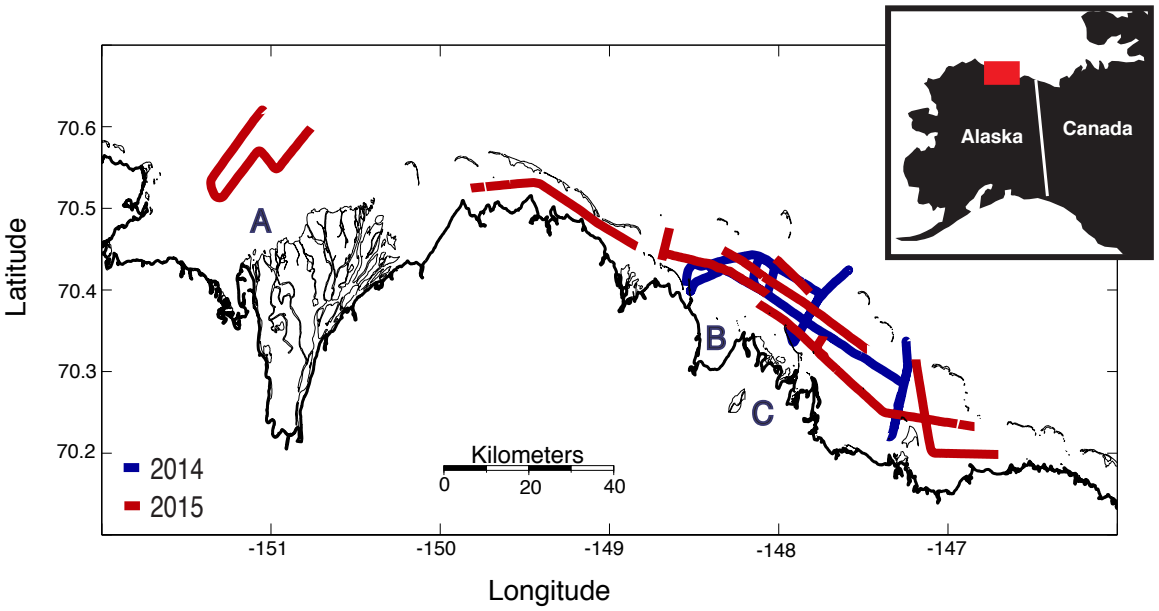

Figure 4.5: Ship tracks from both years of data collection. A: borehole near Harrison Bay. B: borehole near Prudhoe Bay. Both years the edge of the ice pack was near the barrier islands. An inversion of Tow 3 is shown in Figure 4.8.

4.4 Results and Discussion

The inline electric field time series measured on each Porpoise was Fourier transformed and stacked into 60 second windows (*Myer et al.*, 2010). Stacking the data increases its statistical reliability and provides estimates of errors. Processing was done for eleven harmonics of Waveform-D, from the 1 Hz fundamental to 33 Hz. We created pseudosections by calculating the forward solution for 1D models, including appropriate water depth from an echosounder and seawater conductivity from CTD measurements, underlain by halfspaces ranging from 0.1 to 1000 Ωm and interpolating to find the best apparent-resistivity for each value of stacked amplitude. Appropriate skin depths at each frequency can be used to create a frequency pseudosection at one source-receiver offset

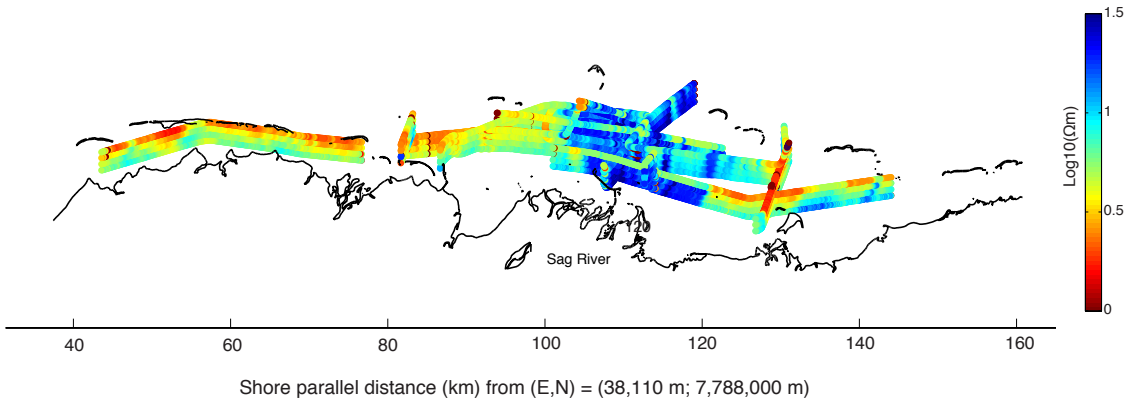

Figure 4.6: Fence diagram of offset apparent-resistivity pseudosections offshore Prudhoe Bay and the Sagavanirktok (Sag) river outflow for both years computed for 3 Hz amplitudes. Blue corresponds to higher resistivity values (up to 30 Ωm) while red is more conductive (down to 1 Ωm).

(e.g., *Weitemeyer and Constable*, 2010), but with four different offsets we can create the more conventional offset pseudosection for each frequency (*Hallof*, 1964). Pseudosections are useful for displaying the lateral variability of a data set, but have limited ability to determine depths (*Weitemeyer et al.*, 2006). The pseudosections for a frequency of 3 Hz are shown in Figures 4.6 and 4.7, short offsets are plotted as shallow structure and long offsets as deeper structure.

The offset pseudosections (Figures 4.6 and 4.7) show significant lateral variability in permafrost extent. Harrison Bay appears very conductive with highest resistivities near 10 Ωm, which is unexpected given that permafrost is seismically inferred in this area (*Brothers et al.*, 2012). However, it is consistent with well logs that show thinning of the ice bearing permafrost layer onshore to the west of Prudhoe Bay (*Collett et al.*, 1989). Onshore at Harrison Bay a well log (labelled A in Figure 4.5) measures maximum resistivity near 100 Ωm down to 120 m, where resistivity drops to over 10 Ωm and the base

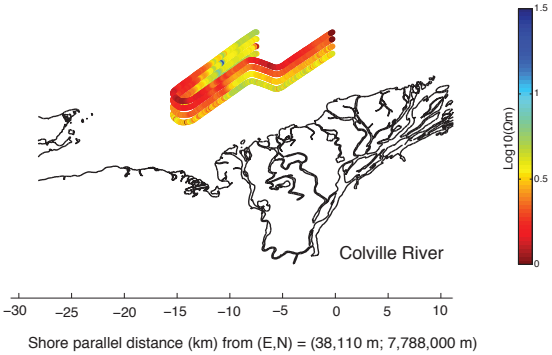

Figure 4.7: Fence diagram of offset apparent-resistivity pseudosection in Harrison Bay and near the Colville river outflow computed for 3 Hz amplitudes.

of the ice-bearing layer is seen at 300 m (*Collett et al.*, 1989). If most of the 120 m thick resistive layer has thawed, the underlying permafrost would be consistent with resistivity values in the pseudosection. Along the coast between Harrison Bay and Prudhoe Bay there is a clear layer of conductive sediments overlying a buried layer of more resistive material, interpreted as permafrost. Just east of Prudhoe Bay there is an increase in resistivity at all depths, implying that permafrost is pervasive in the area near the Sagavanirktok (also called the Sag) river outflow. Because of freshwater influx from rivers and melting of sea ice, sea water conductivity was variable across the entire survey area. In the top meter ocean conductivity ranged from 0.3 to 0.5 Ωm, but at depth remained more constant near 0.4 Ωm. Seawater conductivity variations and water depth were included in the 1D model layers used for pseudosections and therefore do not cause the apparent resistivity variations.

Inversions were done using the MARE2DEM adaptive refinement finite element code (*Key*, 2016). Two dimensional (2D) inversion of CSEM data is computationally

expensive, and many inversions must be carried out to fully understand error structure and the trade off between misfit and model complexity (e.g., *Constable et al.*, 2015). We present one preliminary inversion in Figure 4.8 to illustrate the difference between pseudosections and actual inversion. The inversion shown is for Tow 3, indicated in the map of the survey area in Figure 4.5, and is limited to amplitude, the three largest harmonics of Waveform-D (3, 7, and 13 Hz) for the first three Porpoises (offsets of 250, 500, and 750 m) and the largest two harmonics (3 and 7 Hz) for the last 1000 m offset Porpoise. The inversion grid size ranged from quadrilaterals 150 m wide by 10 m deep in the shallowest region up to 250 m by 50 m at greater depths. The increasing grid size is meant to mimic the loss of spatial resolution with depth as well as decrease computational resources. The inversion results are shown in Figure 4.9 as a contour plot with contours at 3, 20, and 100 Ωm to better differentiate the likely ice-bonded permafrost layer. Due to the variation in water conductivity across this region, we allowed a 2-layer ocean model be free parameters in the inversion, bounded by the maximum and minimum values that were measured with our towed CTD. The inversion chose 0.5 Ωm for the top layer and 0.45 Ωm for the bottom, which are consistent with the upper range of the CTD measurements.

On the northwestern end of Tow 3, in the section before the Sag River outflow, we see conductive sediments overlying two resistive patches. The southeastern side of the inversion shows a thin layer of conductive marine sediments at the surface, underlain by a non-uniform layer of resistive material. Below the resistive layer the inversion returns to higher conductivities consistent with freshwater sediments. The peak resistivity in the tow 3 inversion is over 300 Ωm, which we consider consistent with ice-bonded permafrost.

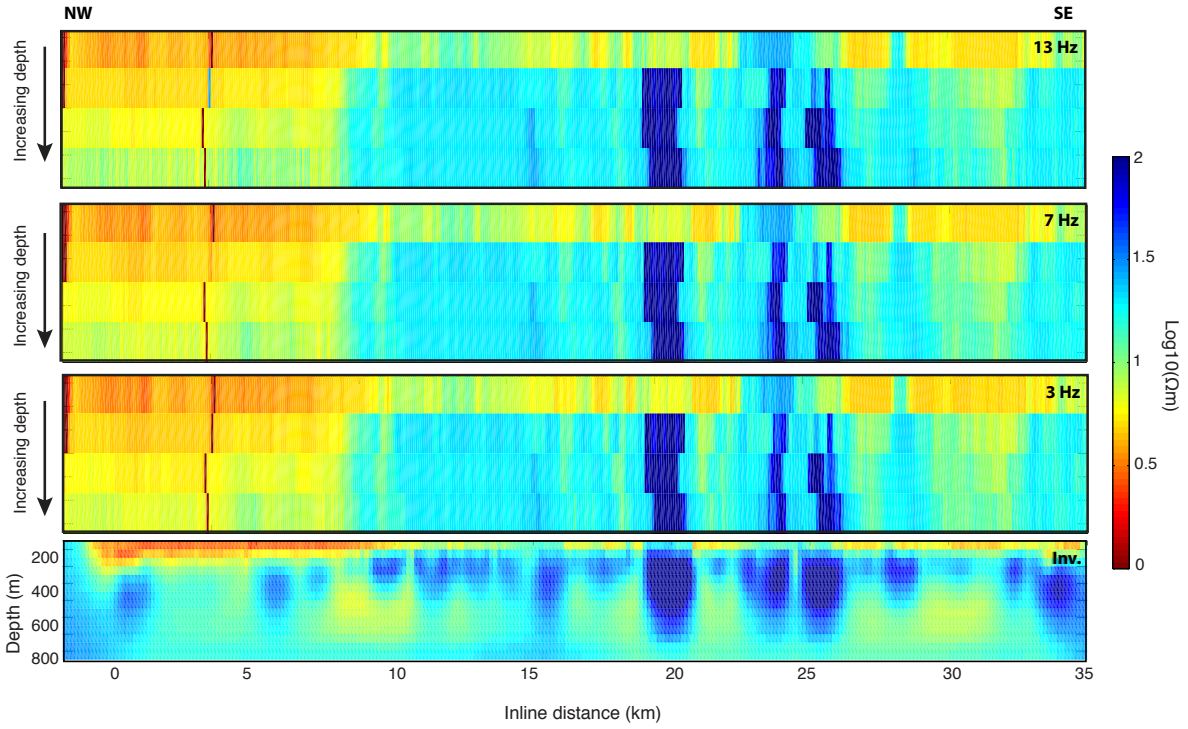

Figure 4.8: Inversion of Tow 3, a line spanning the Sag River outflow (bottom). The river outflow begins about 8 km inline distance. Pseudosections for 3, 7 and 13 Hz, the three inversion frequencies, are plotted above in order of increasing depth penetration. Note that data contributing to the conductive artifact present in the pseudosections near 3 km inline distance have been removed in the inversion. The inversion fits to an RMS of 1.5 with an error floor of 3%.

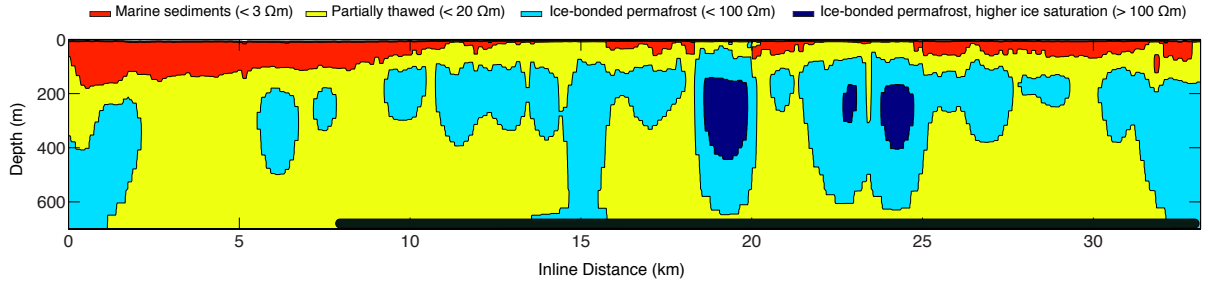

Figure 4.9: Same inversion of Tow 3 shown in Figure 4.8, but plotted with four major contours colored with the same colorscale as Figure 4.8. The first regime is for marine sediments with resistivities <3 Ωm, followed by resistivities <10 Ωm which could be partially thawed ice-bearing permafrost or freshwater pore fluids, and the threshold for ice-bonded permafrost was set at >20 Ωm (*Collett et al.*, 1989) with over 100 Ωm indicating regions of exceptionally high ice saturation. The dark bar at the bottom of the figure indicates the region of the Sag River outflow.

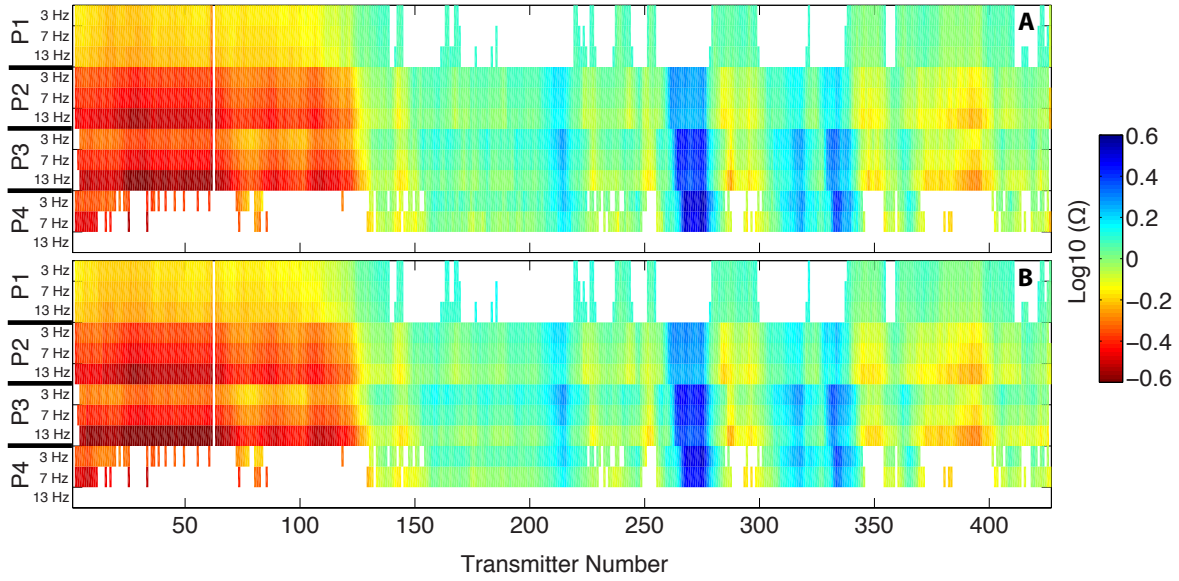

Figure 4.10: A: Amplitude at each frequency and offset for data inverted in Figure 4.8, normalized by the median amplitude of each offset. B: Inverted amplitude for each frequency and offset, normalized by the same values as the data amplitudes. Gaps show data that has been filtered out due to poor signal to noise ratio or from amplifier clipping.

The pseudosections for the 3 inverted frequencies of Tow 3 are plotted above the inversion result, and results are consistent with the inversion. The inversion fits the data to an RMS of 1.3 with a 3% noise floor and a comparison of data and model amplitudes is shown in Figure 4.10.

Because CSEM and seismic refraction methods are sensitive to different physical phenomena, we do not expect them to yield identical information, and indeed if they did it would be redundant to conduct both surveys. Strong seismic refractions occur when there is a sharp velocity increase while the CSEM method is more sensitive to the total ice fraction. In the region of the Sag River outflow, a seismic refraction survey (*Brothers et al.*, 2012) measured an increased p-wave velocity ($V_p > 2.8$km/s) where the CSEM pseudosections show resistive anomalies over 30 Ωm. Together, these observations

indicate an extensive amount of permafrost correlated with the river outflow. Seismic refraction data continues to see elevated p-wave velocities (V_p>2.8 km/s) from northwest of the Sag River through Harrison Bay, while the resistivity values decrease. Resistivity still provides a positive indication of permafrost, but lower resistivity implies that there is less total ice volume, and is again in agreement with the thinning trend from Prudhoe Bay to Harrison Bay seen in onshore permafrost. The pseudosections would not resolve a thin layer of ice-bonded permafrost and are likely producing an average resistivity of ice-bonded permafrost and surrounding marine sediments.

In contrast, to the immediate southeast of the Sag River, seismic refraction data detected lower velocity increases ($V_p > 2.3$ km/s) consistent with ice-bearing, but not ice-bonded permafrost. CSEM pseudosections show continued elevated resistivity (>10Ωm) before transitioning to higher conductivities at short offsets (shallow) and resistivities of 8-10 Ωm at long offsets (deeper). Either the ice-bearing permafrost has a stronger resistivity signature than velocity increase or the resistivity anomaly in this area is from a different source, i.e. freshening of porewater fluids. Ice-bonded permafrost is impermeable to water, so any ground water needs to flow under or around the ice-bonded permafrost. The southeast side of the Sag River is the side without ice-bonded permafrost (*Brothers et al.*, 2012) and therefore where fresh groundwater can flow and freshen the pore fluid. Beneath the permafrost layer should be water saturated sediment, offshore this may be brine or fresh, but onshore it will likely be fresh. Borehole measurements taken beneath the permafrost layer onshore show resistivities up to 20 Ωm (*Collett et al.*, 2011), which implies that freshening of pore fluids offshore cannot increase resistivity beyond about

20 Ωm. Therefore, we infer that the very high resistivity values offshore Sag River are from increased ice content. Fresh ground water flowing beneath this permafrost layer, however, may affect our ability to detect the base of permafrost in this area.

Modeling suggests that groundwater flow preserves permafrost by freshening the porewater fluid and raising the freezing temperature above the ambient ocean temperature (*Frederick and Buffet*, 2015). By definition, permafrost is ground that is below the freezing point of water. Therefore, when groundwater is flowing into areas where permafrost exists it is flowing into a temperature regime where it will freeze, turning to ice and preserving the thickness of the permafrost layer. Using a synthetic model of the continental shelf, *Frederick and Buffet* (2015) calculated the offshore extent of subsea permafrost in the presence of a ground water flow which ranged from 0 to over 140 $m^3yr^{-1}m^{-1}$ over many glacial cycles. They concluded that local hydrology is as important as paleoclimate conditions and sea level rise in determining current permafrost extent. While this model is consistent with the presence of permafrost offshore the Sag River, the same results are not seen offshore the Colville River. *Brothers et al.* (2012) also note that larger rivers can act as a heat source and prevent permafrost from forming when exposed to sub-freezing temperatures (*Frederick and Buffet*, 2014). Taliks, or unfrozen regions in otherwise continuous permafrost, occur in paleo river channels, such as the Colville River which has a talik extending hundreds of feet beneath its bed (*Williams*, 1970). The Colville is larger than the Sag and may be an example of the latter effect of local hydrology and be acting as a heat source rather than a preserving force.

4.5 Conclusions

Our surface towed CSEM system was successful at characterizing resistivity to a depth of about 800 m in 0-8 m water depths offshore Prudhoe Bay. Apparent resistivity in the region ranged from 1 Ωm, a value typical of marine sediments, to over 100 Ωm, which we interpret as ice-bonded permafrost. In areas with seismically interpreted permafrost, apparent resistivity varied from 10 Ωm to over 100 Ωm, indicating that there is both ice-bearing and ice-bonded permafrost offshore Prudhoe Bay and that EM methods may be capable of distinguishing between the two. Inverted base of offshore permafrost is near 600 m, consistent with well logs measuring an onshore permafrost layer of 660 m at Prudhoe Bay. Pseudosections and initial inversions both show increased resistivity at the Sag River outflow, offering support to the idea that groundwater preserves permafrost. Future work will include carrying out inversions on all lines, integrating seismic horizons into the inversions, and further exploring the role of local hydrology in permafrost preservation.

The text in Chapter 4, in part or in full, is a reprint of material from its publication in *Earth and Planetary Science Letters* (*Sherman et al.*, 2017). The dissertation author was the first author of the published work; coauthors on the publication were Peter Kannberg and Steven Constable. Peter Kannberg aided in data collection and initial processing. Steven Constable supervised the research.

Bibliography

Brothers, L. L., P. E. Hart, and C. D. Ruppel (2012), Minimum distribution of subsea ice-bearing permafrost on the U.S. Beaufort Sea continental shelf, *Geophys. Res. Lett.*, *39*, L15501.

Collet, T. S., L.W. Myung, W. F. Agena, J. J. Miller, M. V. Lewis, R. Boswell, T. L. Inks (2011) Permafrost-associated natural gas hydrate occurrences on the Alaskan North Slope, *Mar. Pet. Geol.*, *28*, 279-294

Collett, T.S., K.J. Bird, K.A. Kvenvolden, and L.B. Magoon (1989), Map showing the depth to the base of the deepest ice-bearing permafrost as determined from well logs, North Slope, Alaska: USGS Oil and Gas Investigations Map 222.

Constable, S. C., A. Orange, and K. W. Key (2015) And the geophysicist replied:"Which model do you want", *Geophysics*, *80*(3) 197-212

Constable, S. C., P. Kannberg, K. A. Weitemeyer (2016) Vulcan: A deep-towed CSEM receiver, *Geochem. Geophy. Geosy.*, *17*, 1042-1064

Daniels, J.J., G.V. Keller, and J.J. Jacobson (1976) Computer-assisted interpretation of electromagnetic soundings over a permafrost section. *Geophysics. 41*(4) 752-765

Frederick, J. M., and B. A. Buffett (2015), Effects of submarine groundwater discharge on the present-day extent of relict submarine permafrost and gas hydrate stability on the Beaufort Sea continental shelf. *J. Geophys. Res. Earth Surf.*, *120*, 417432

Frederick, J. M., and B. A. Buffett (2014), Taliks in relict submarine permafrost and methane hydrate deposits: Pathways for gas escape under present and future conditions, *J. Geophys. Res. Earth Surf.*, *119*, 106 -122

Hallof, P. G. (1964) A comparison of the various parameters employed in the variable-frequency induced-polarization method. *Geophysics. 29*(3) 425-433

Hauck, C. (2016) Frozen ground monitoring using DC resistivity tomography. *Geophys. Res. Lett.. 29*(21)

Hill, P.R., P.J. Mudie, K. Moran and S.M. Blasco (1985) A sea-level curve for the Canadian Beaufort Shelf, *Can. J. Earth Sci.*, *22*(1) 1383-1393

Houseknecht, W., and K. J. Bird (2011) Geology and petroleum potential of the rifted margins of the Canada Basin, in *Arctic Petroleum Geology, Geol. Soc. Mem.*, vol. 35, edited by A.M. Spencer et al., 509-526, Geol. Soc., London

Hubbard, R. J., S. P. Edrich, and R. P. Rattey (1987) Geologic evolution and hydrocarbon habitat of the 'Arctic Alaska Microplate'. *Mar. Pet. Geol.*, *4*(1) 2-34

Johansen, T. A., P. Digranes, M. van Schaack, and I. Lonne (2003), Seismic mapping and modeling of near-surface sediments in polar areas, *Geophysics*, *62*(2), 1-8

Jorgenson, T., K. Yoshikawa, M. Kanevskiy, Y. Shur, V. Romanovsky, S. Marchenko, G. Grosse, J. Brown, and B. Jones (2008), Permafrost characteristics of Alaska, Institute of Northern Engineering, University of Alaska Fairbanks, 1 p.

Key, K. W. (2016). MARE2DEM: a 2-D inversion code for controlled-source electromagnetic data. *Geophys. J. Int.*, *207*, 571-588

Martin, T. P. (2015). Mapping Porosity Structure Offshore Torrey Pines State Natural Reserve and Del Mar, California Using a Surface Towed EM System. UC San Diego: b8887341. Retrieved from: http://escholarship.org/uc/item/45p0062c. Accessed on May 2, 2016.

Myer, D., S. C. Constable, K. W. Key (2010), Broad-band waveforms and robust processing for marine CSEM surveys. *Geophys. J. Int.*, *184*, 689-698.

Osterkamp, T. E., (2001) Sub-sea permafrost in Encyclopedia of Ocean Sciences (Second Edition), pp 559-569, Academic Press.

Ruppel, C.D. (2011) Methane Hydrates and Contemporary Climate Change. *Nature Education Knowledge*, 3(10):29

Sherman, D., P. Kannberg, and S. Constable, (2017), Surface towed electromagnetic system for mapping of subsea Arctic permafrost, *Earth Planet. Sci. Lett.*, *460* 97-104

Todd, B. J., S. R. Dallimore (1998) Electromagnetic and geological transect across permafrost terrain, Mackensie River delta, Canada. *Geophysics*, *63*(6), 1914-1924

Weitemeyer, K. A., and S. C. Constable (2010) Mapping shallow geology and gas hydrate with marine CSEM surveys. *First Break*, *28*, 97-102.

Weitemeyer, K. A., S. Constable, K. W. Key, J. P. Behrens, (2006) First results from a marine controlled-source electromagnetic survey to detect gas hydrates offshore Oregon, *Geophys. Res. Lett.*, *33*, L03304

J. R. Williams (1970) Ground Water in the Permafrost Regions of Alaska. *Geological Survey Professional Paper 696*

Chapter 5

CSEM Results

To process CSEM Porpoise inline electric field time series, it is Fourier transformed and stacked into 60-second windows to increase statistical reliability and signal to noise ratio (*Myer et al.*, 2010). These complex Fourier coefficients are typically shown as amplitude normalized to the source electric dipole moment (in V/Am^2) and phase (in degrees). The CSEM transmitter outputs a symmetric quasi-square wave, known as waveform-D, that spreads power from the fundamental frequency into odd harmonics across about a decade of frequencies (*Myer et al.*, 2010). The 3rd, 7th, and 13th harmonics are the most powerful and are the frequencies used in this analysis.

In 2014 a timing fault in the transmitter operation led to rapidly drifting phase, which when stacked also distorted the amplitude data. Because the phase drift was mostly linear, it could be removed to salvage the amplitude data, but not the phase data. As a result, we do not use phase data from this year. In 2015, the transmitter was improved and a timing pulse was sent from the GPS clock to the Porpoise receiver to improve our

clock-drift correction. The timing pulse was processed the same way as other Porpoise channels to obtain a direct point by point phase correction.

After data processing the easiest and fastest way to assess resistivity structure is to create apparent-resistivity pseudosections, which were shown in Chapter 3 as part of the EPSL paper. Pseudosections do not produce any information about depth of anomalies, but serve to give an idea of the range of resistivity values encountered and their map locations. Obtaining depth information requires inversions, some select inversions are presented and discussed in this chapter and the rest can be found in the appendices A and B. All inversions include data at three frequencies, 3 Hz, 7 Hz, and 13 Hz, and four offsets, 250 m, 500 m, 750 m and 1000 m. Data used in inversions are also filtered on signal to noise ratio (SNR), and for some lines the SNR dips below the minimum threshold of 20 for the longest offset and highest frequency data.

5.1 Inversion results and anisotropy

Inversions were done using Kerry Key's MARE2DEM code (*Key*, 2016), which uses a goal-oriented adaptive refinement forward algorithm and the Occam approach for inversions. Due to the timing issue in the data in the first year (2014) that rendered the phase data useless, isotopic amplitude-only inversions were run for lines from both years before including phase in the 2015 data. Our only shore-perpendicular tows near Prudhoe Bay were collected in 2014 and are therefore amplitude only.

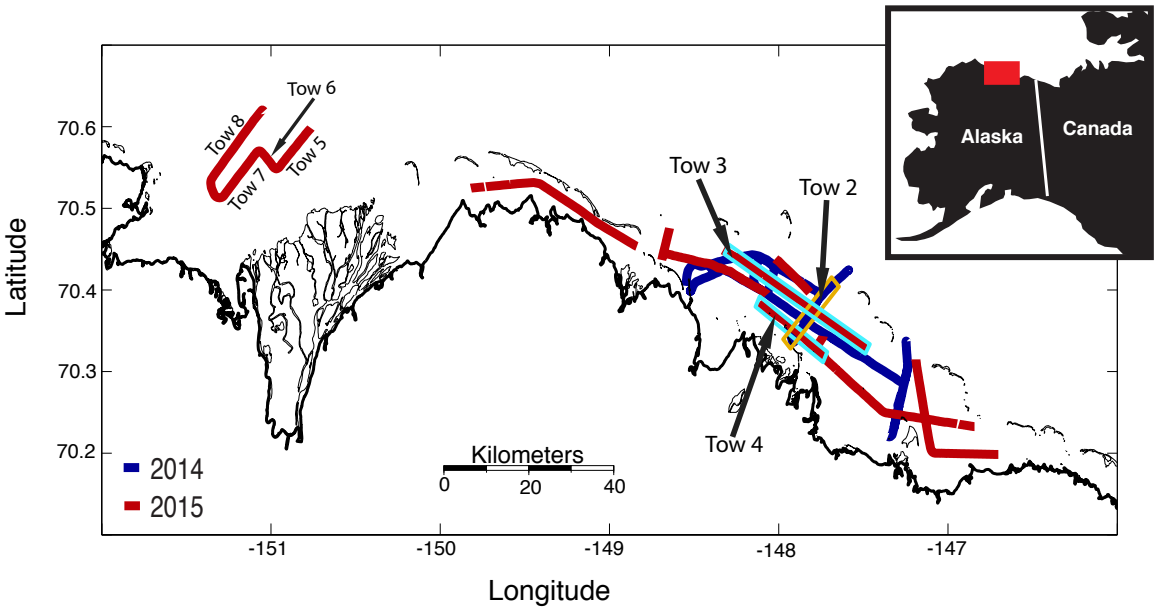

Figure 5.1: Map of all CSEM tow lines collected in 2014 (purple) and 2015 (red). Tows whose inversions are presented in this chapter are labeled.

5.1.1 Inversions near Prudhoe Bay

Prudhoe Bay is underlain by multiple oil and gas reservoirs and has anomalously thick permafrost onshore compared to surrounding areas (*Collett et al.*, 1989). This is likely due to coarser grained lithologies found in the Prudhoe Bay region when compared to the National Petroleum Reserve, Alaska (NPRA) to the west (*Osterkamp and Payne*, 1981).

Shore perpendicular isotropic inversion from amplitude. In Figure 5.2 the inversion from the shore perpendicular 2014 Tow 2 is plotted on a linear scale to highlight areas with resistivities high enough to be considered intermediate to high ice saturation permafrost. The location of Tow 2 is highlighted in orange in Figure 5.1. Following the lead of *Ruppel et al.* (2016), over 100 Ωm can be considered high saturation ice-boned

permafrost and over 10 Ωm indicates the presence of a lesser saturation of ice-bonded permafrost. In Figure 5.2, 0 km inline is nearest shore, 7 km is further from shore and just short of the barrier islands.

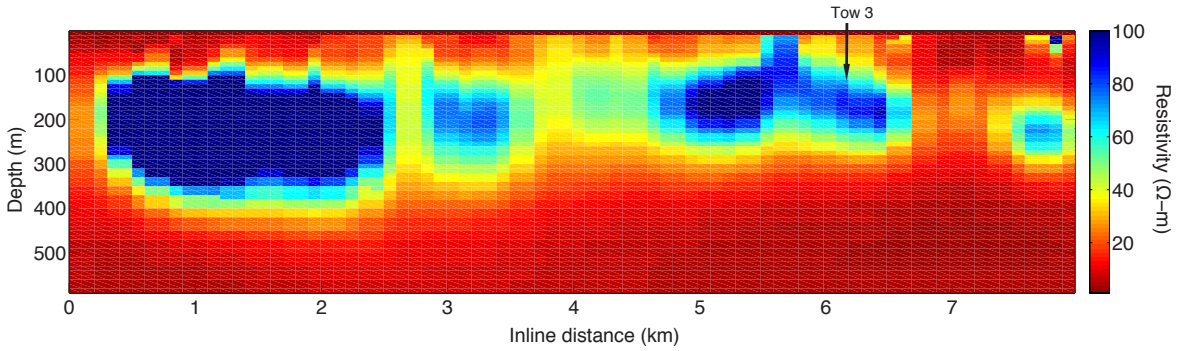

Figure 5.2: Tow 2 from 2014, shore perpendicular from the Sag River. 0 km inline is nearest shore, 7 km is further from shore and just shy of the barrier islands.

The peak resistivity is 1500 Ωm and it occurs near shore where permafrost is thickest. Out to about 6 km the predominant thinning trend is from the base up while the top remains close to 100 m depth, after 6 km the depth to permafrost increases and it appears to become more discontinuous; this occurs a few kilometers short of the barrier island chain. Inversion fits to an RMS of 1.5 with a 3% noise floor on all four porpoises at frequencies of 3 Hz, 7 Hz, and 13 Hz. Model fit to data is shown in Figure 5.10 for all offsets at 7 Hz.

Inversions and anisotropy from 2015. Another line of particular interest is Tow 3 from 2015, whose location is labeled and highlight in cyan in Figure 5.1. This line is shore parallel, begins just offshore the east side of Prudhoe Bay, and terminates roughly inline with the eastern side of the Sag River outflow. Figure 5.4 shows the amplitude-only isotropic inversion of this line.

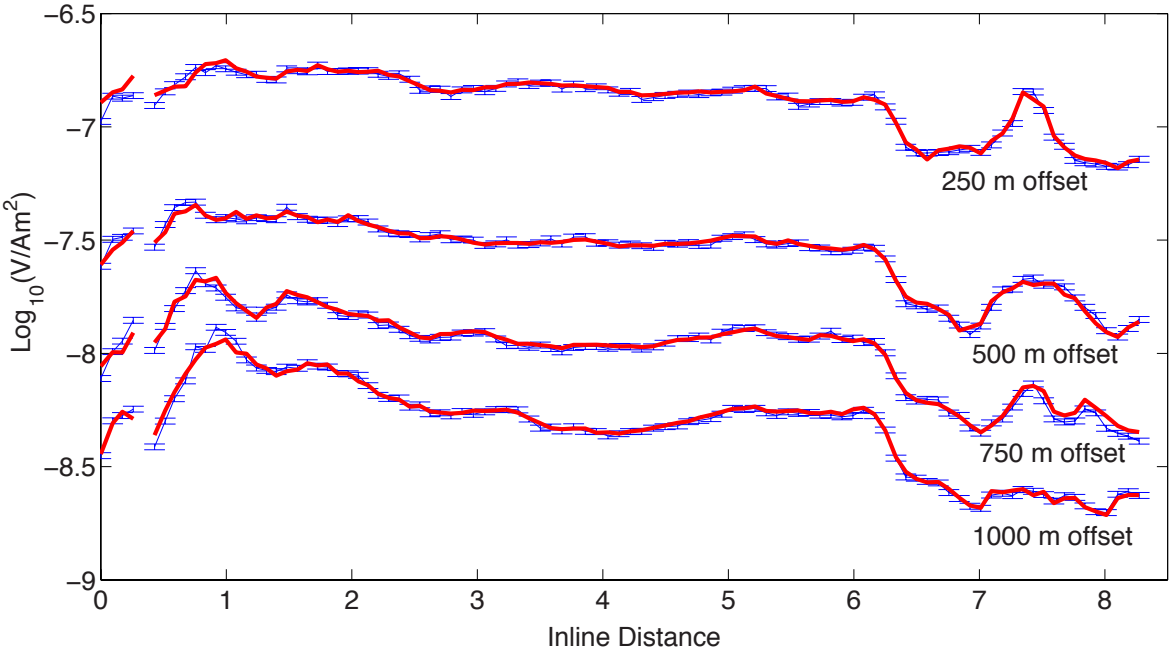

Figure 5.3: Model fit to data at 7 Hz and all offsets for the inversion shown in Figure 5.2, model is shown in red and data with error bars in blue.

The 17 km inline point on Tow 3, an area of lower resistivity between two highly resistive patches, crosses perpendicularly at the 6 km inline point of Tow 2, the start of a region of lower resistivities after a continuous section with high resistivities. Inversion fits to an RMS of 1.5 with a 3% noise floor on all four Porpoises used at frequencies of 3 Hz, 7 Hz, and 13 Hz, with the exception of Porpoise 4 which did not have a high enough SNR at 13 Hz. Highly resistive features on Tow 3 occur after the start of the Sag River outflow (8 km inline) and near the surface ($<$ 100 m depth), which suggests that the freshwater influx of river water may prevent saline intrusion from thawing the top portion of the permafrost layer.

Resistive structure on this line in particular is very patchy. The resistive blocks tend to be 500 m to a few kilometers wide. Ice wedge polygons are much smaller than

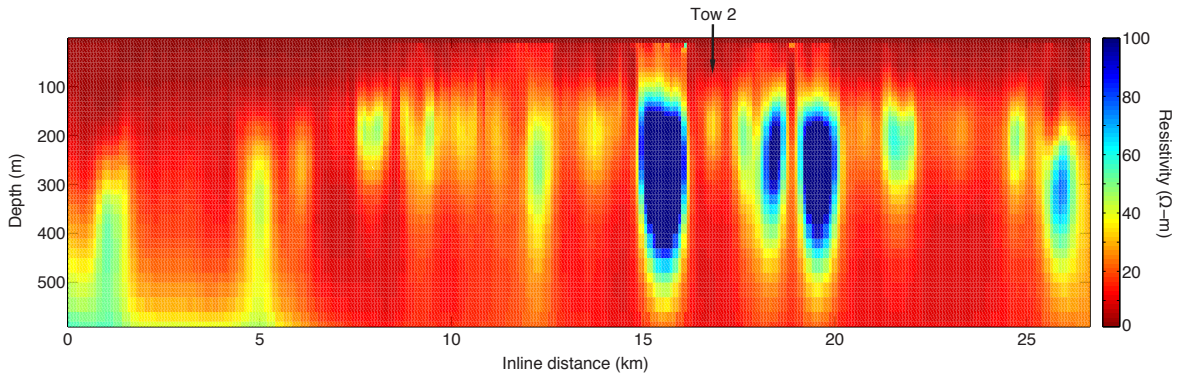

Figure 5.4: Tow 3 from 2015, shore parallel across the Sag River outflow. River begins at about 8 km inline.

this, 5-50 m wide, but larger surface features such as pingos are over 100 m and up to 900 m across, and thermokarst lakes vary widely in size and can also be hundreds of meters across. However, thermokarst lakes would lead to taliks, not resistive zones, and pingos are not very common and are unlikely to account for the row of patches seen here. The patchy appearance of this inversion is significantly smoothed once phase is included and an anisotropic model used.

Once phase was included in the inversions of Tow 3 2015 data, an isotropic model was not able to fit amplitude and phase simultaneously and an anisotropic model was required. The isotropic model would not fit amplitude and phase data with a 3% noise floor better than an RMS of 2.6. Additionally, the phase residuals were systematically biased and increased with both offset and frequency up to an offset of 8 error bars. For this reason we included transverse vertical anisotropy in the modeling, where vertical resistivity is allowed to be different from horizontal resistivity. Through trial and error while inverting Tow 3, it was found that an anisotropic penalty weight of p =0.1 was needed to obtain a

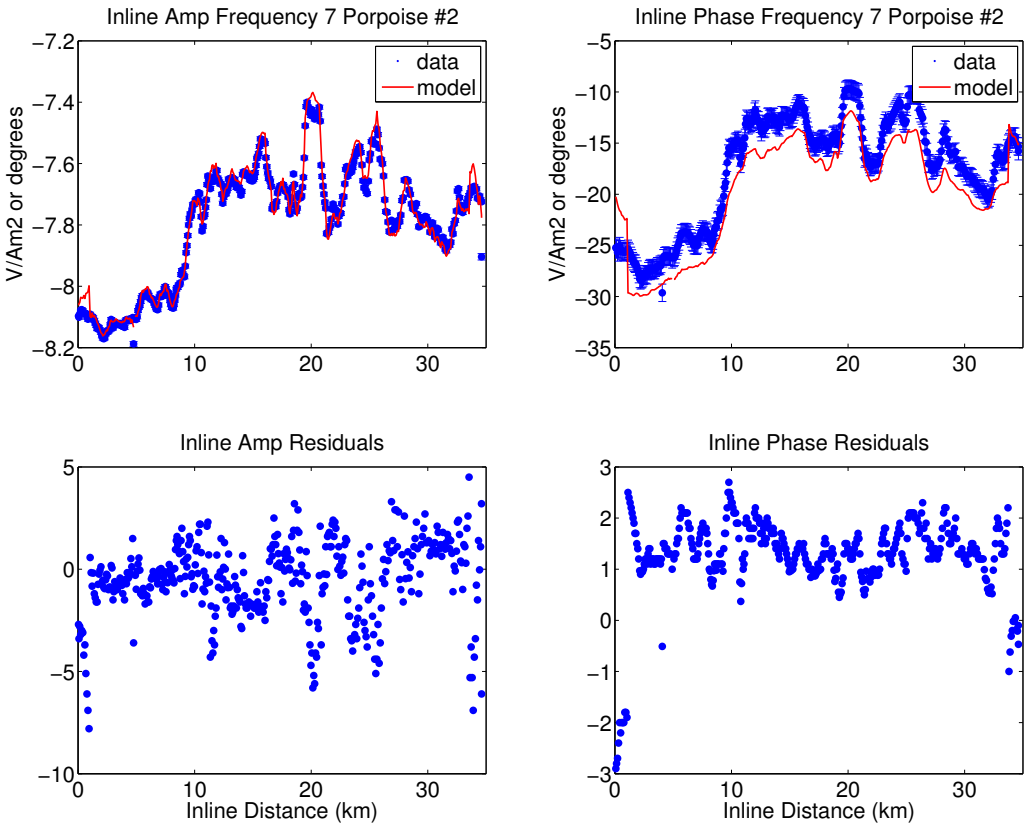

Figure 5.5: Data fit for the 8^{th} iteration of an isotropic inversion of Tow 3. An RMS of 2.6 was achieved for a 3% noise floor and the inversion could not further decrease the RMS.

reasonable data misfit and agreement between data and model response. Figure 5.7 shows the anisotropic inversion of Tow 3. Even though more data has been added (inclusion of phase), the anisotropic inversion fits the data better, to an RMS of 1.3 at the same 3% noise floor.

Figure 5.5 shows an example of data fit to an isotropic inversion of amplitude and phase data for the 500 m offset Porpoise at 7 Hz of Tow 3. The inversion did not converge, but completed 8 iterations and reached a minimum RMS of 2.5 with a 3% noise floor.

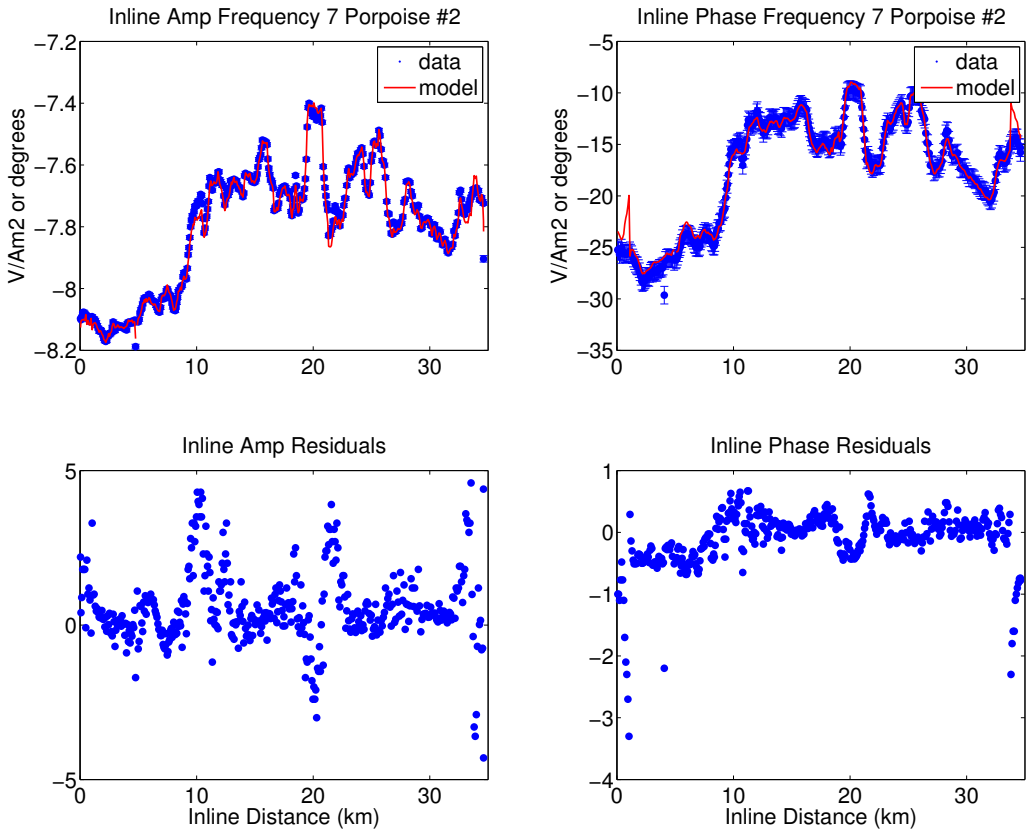

Figure 5.6: Data fit for the 8^{th} iteration of an anisotropic inversion of Tow 3. An RMS of below 2 has already been reached with a 3% noise floor and the inversion continued until converging with an RMS of 1.3.

In contrast, after 8 iterations an anisotropic inversion with an anisotropy penalty weight (APW) of 0.1 has already reached an RMS below 2 and the phase residuals are not biased as in the isotropic inversion. Data fits for the same Porpoise and frequency are shown in Figure 5.6 for the eighth iteration of the anisotropic inversion.

Anisotropy is generally either due to intrinsic microscopic properties of a material or macro-scale layering in a material. Inherent microscopic anisotropy of ice crystals is unlikely because we have no reason to think they would be aligned. Bulk anisotropy due

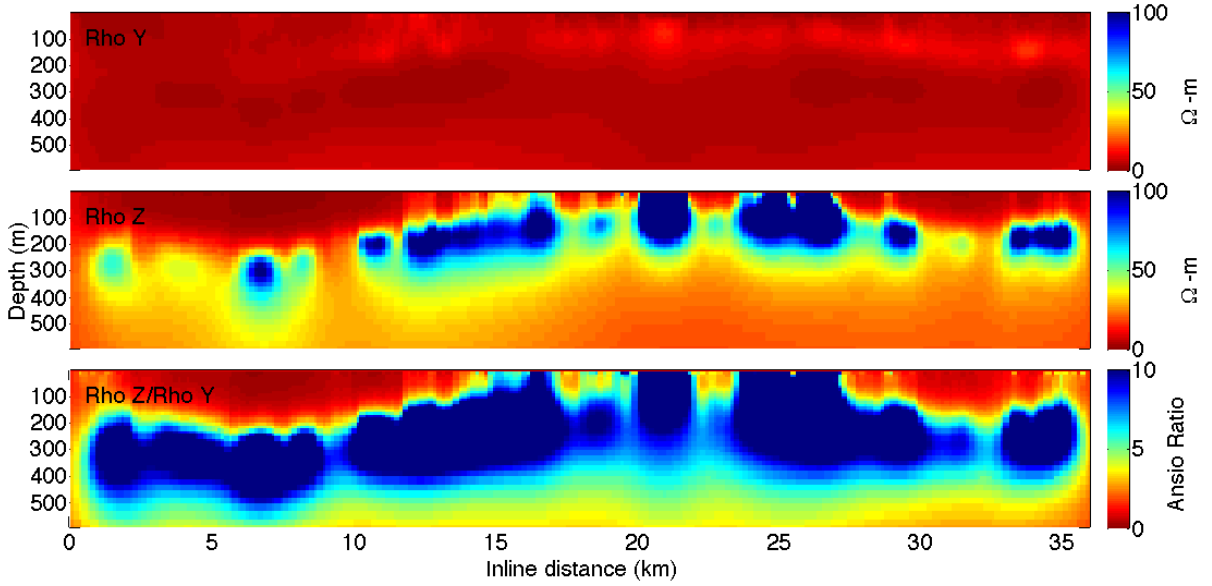

Figure 5.7: Tow 3 from 2015, anisotropic inversion, shore parallel across the Sag River outflow. River begins at about 8 km inline. Top: Horizontal Resistivity. Middle: Vertical resistivity. Bottom: anisotropy ratio, vertical/ horizontal resistivity.

to layers of resistive and conductive material below the resolution limit of our CSEM technique (about 10% of depth) is the most likely cause of anisotropy in our inversions. If a horizontally layered section of permafrost is thought of as a circuit, the vertical resistance would be the resistance of the horizontal layers added in series and the horizontal resistance would add in parallel. Therefore, vertical resistivity is more sensitive to the resistive structure because current flows through every resistive layer, and horizontal resistivity is more sensitive to conductive layers because current can flow horizontally in a conductive layer without much interference from the resistive layers. The result is an anisotropy ratio, defined as the ratio of vertical to horizontal resistivity, of greater than one in cases with horizontally bedded layers.

Hydrates have been found to be electrically anisotropic in practice (*Constable et al.*,

2016; *Cook et al.*, 2012), and in theory have been modeled as 25 m thick layers every 75 m (*Frederick and Buffet*, 2014) because they preferentially form in coarse grained lithologies. Because hydrate is mostly ice, it is not unreasonable to think that similar lithologies would preferentially freeze during the formation of permafrost while extruding brine into bordering layers, creating the kind of inter-bedding that would produce electrical anisotropy.

As mentioned, various values of APW were tried for Tow 3 and an APW of 0.1 found to be the highest penalty weight that allowed the inversion to reach the desired misfit. Due to the computational expense of running 2D CSEM inversions, the same amount of experimentation was not done on all lines to determine the best APW, instead Tow 3 was used as a test case. All anisotropic inversions therefore use an APW of 0.1 and with few exceptions isotropic inversions were not attempted with phase data.

Bulk resistivity values from our inversions can be used to estimate ice-saturation of the sediment using Archie's law (*Archie*, 1942). The details of the calculation of ice-saturation are given in the next chapter (see Equation 6.1) and is based on the method presented by *Ruppel et al.* (2016). Archie's law is an empirical formula used to approximate host rock saturation given a resistivity measurement and porosity of the host rock, and it assumes an isotropic medium. Applying this equation we find ice-saturations from Tow 2 of over 50 % in the IBPF section, with peak values over 90% saturated. For Tow 3 we assume all anisotropy is due to interbedded layers of isotropic material, then we take vertical resistivity from Tow 3 to be the isotropic resistivity of frozen sediment and horizontal resistivity to be isotropic resistivity of unfrozen sediment. We find horizontal resistivity gives about 20% ice saturation in top 200 m, and no ice saturation below 200 m

while vertical resistivity gives ice-saturations of over 60% in IBPF layer with a peak of over 90% in the highest resistivity regions. We cannot, however, comment on what percentage of the IBPF layer is frozen.

Calculation of ice-saturation assumes that the host rock was 100% saturated with water at the start of freezing, and that the only increase in resistivity is due to an increase in ice content. However, resistivity of sediments can increase for many reasons, in this Arctic environment the most likely explanation is the presence of IBPF both because of the ground temperatures and evidence from well logs. The shallow resistivity increases near the Sagavanirktok River outflow, however, make the determination of the cause of resistivity increase more difficult to discern because the river could be freshening pore fluids enough to create a resistive anomaly or the pore fluids could be freshened enough to freeze. Using Archie's law and assuming the same porosity and constants as for our calculation of ice-saturation (*Ruppel et al.*, 2016) presented in the section 6.2, we calculate that Tow 3 would require low salinity pore water with resistivity over 20 ohm-m to produce the vertical resistivity values in our models, a reasonable resistivity value for freshwater. However, anisotropy is not explained by freshwater saturated sediment. The top 200 m of Tow 3 are less anisotropic than the rest of the resistive layer because the horizontal resistivity is higher. This could be because the top 200 m has been freshened by the fresh water influx from the Sagavanirktok River and then only partially frozen.

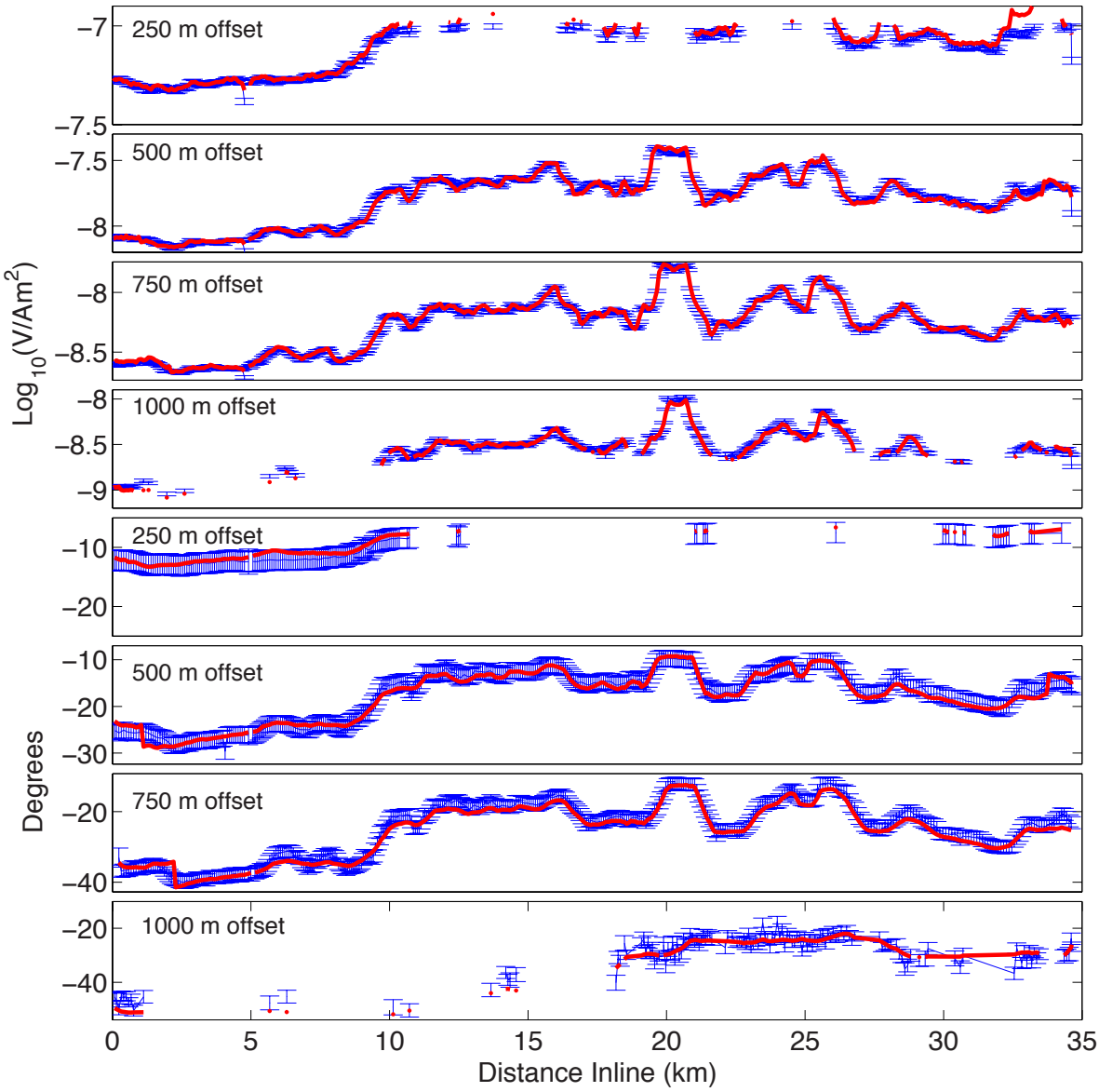

Figure 5.8: Model fit to data at 7 Hz and all offsets for the inversion shown in Figure 5.7, model is shown in red and data with error bars in blue.

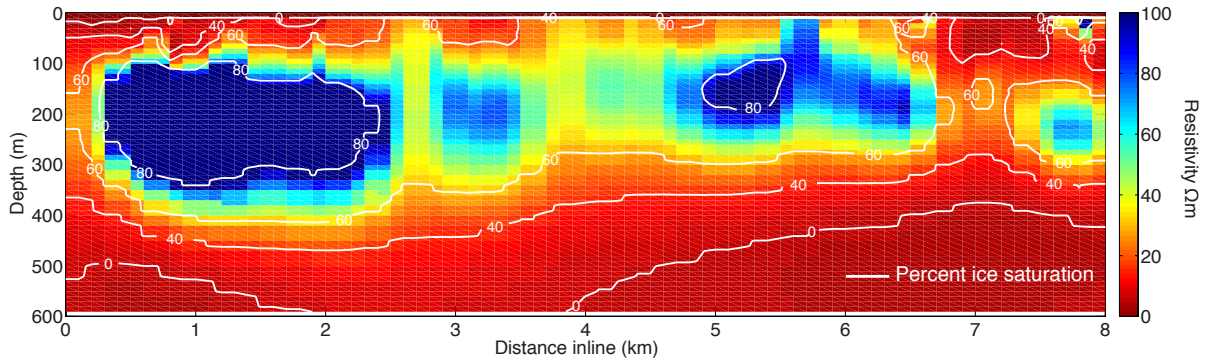

Figure 5.9: Contour lines indicating percent ice-saturation as calculated by Equation 6.1 plotted on top of Tow 2 inversion.

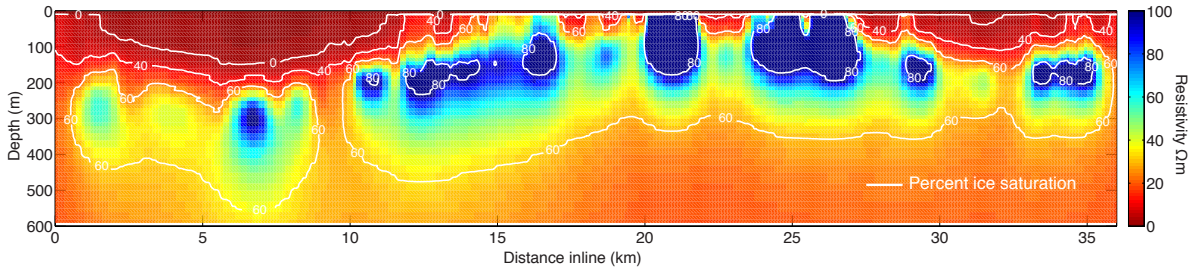

Figure 5.10: Contour lines indicating percent ice-saturation within frozen sections as calculated by Equation 6.1 plotted on top of vertical resistivity from the anisotropic Tow 3 inversion.

5.1.2 Including seafloor receivers

Tow 4 from 2015 is the only line that was able to fit both amplitude and phase with an isotropic inversion. This tow is shoreward of Tow 3, is directly offshore the Sagavanirktok River outflow, and has three seafloor receivers with useable data.

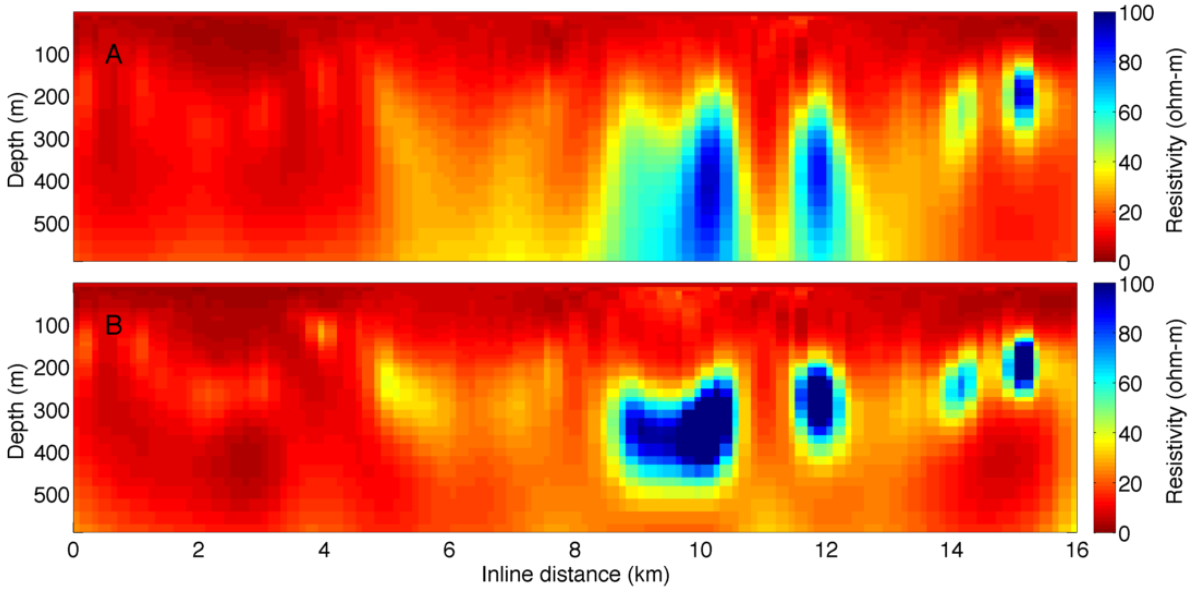

Figure 5.11: Tow 4 from 2015. A. Amplitude only isotropic inversion fits to RMS 1 with 3% noise floor. B. Amplitude and phase isotropic inversions fits to RMS 1 with 3% noise floor.

Both isotropic inversions, shown in Figure 5.11, fit the data equally well to an RMS of 1 with a 3% noise floor. The addition of phase data increased the inversion's ability to resolve the base of resistors and decreased vertical smearing.

Anisotropic inversion of Tow 4 is shown in Figure 5.12, and indicates structure reasonably similar to the isotropic inversion. Allowing for anisotropy does however increase horizontal continuity of resistors in the model, and the anisotropy ratio highlights structure on the far left that is resistive enough to be permafrost. That resistor is not obvious from

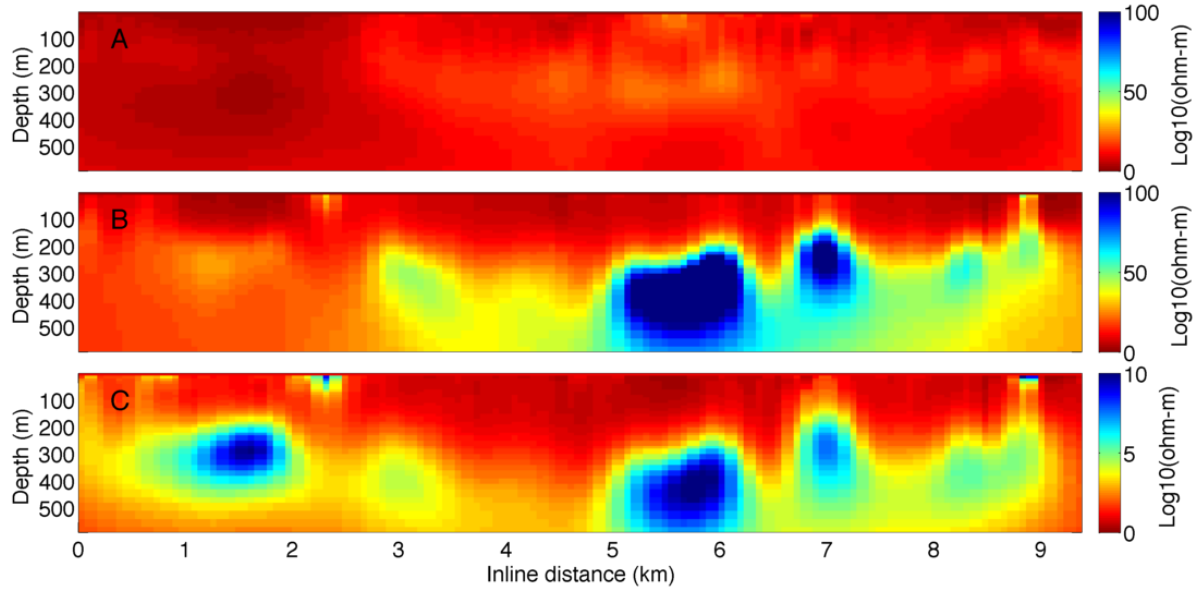

Figure 5.12: Tow 4 form 2015, amplitude and phase anisotropic inversion fit to RMS 1 with 3% noise floor. A. Horizontal resistivity. B. Vertical resistivity. C. Anisotropy ratio, vertical resistivity divided by horizontal resistivity

the isotropic inversion, and the vertical resistivity in the anisotropic model is only modestly elevated over background. Part of the anisotropy comes from decreased resistivity values in horizontal resistivity.

The Porpoise data on Tow 4 were high in amplitude, which is consistent with a resistive section. The high amplitude resulted in the majority of the data from the short offset Porpoise being removed because of amplifier clipping. The SNR on the long offset Porpoise was not good for most of the line, so the inversion relies mostly on the 500 m and 750 m offset Porpoises. This significantly reduces our depth sensitivity, from 500 m to 375 m, using the rule of thumb that depth is equal to half the source receiver offset. This raises the question of whether the depth seen by the Porpoises is the true depth of permafrost. On this line we can answer that question with moored seafloor receivers.

Three moored seafloor receivers were deployed along Tow 4 in 2015 and useable SNR was recovered for offsets up to 6 km at low frequencies and up to 4 km at higher frequencies. Each seafloor receiver is equipped with two orthogonal 5 m dipoles measuring electric field in two directions, the Scripps data logger system (*Constable*, 2013), and an external compass to record orientation. Instruments are weighted and dropped to the seafloor, location noted, and position marked with an orange buoy. They are recovered by hand at the end of the day and nothing is left behind on the seafloor. Seafloor receivers do not replace the Porpoise system in terms of mapping resolution of nearshore structure, but they provide complementary information about deeper resistivity structure.

Given that the deepest permafrost on land in Prudhoe Bay is just less than 700 m, resistors deeper than this are likely associated hydrate. Resolving the transition to unfrozen sediments beneath the permafrost will help clarify the meaning of resistive anomalies by giving us a better sense of the resistivity of unfrozen sediment offshore. Recording two orthogonal directions of the electric field and orientation allows us to rotate the data to inline and crossline electric fields. Only the inline field has been used in inversions here. Figure 5.13 shows an isotropic inversion of seafloor receiver amplitude that has converged to an RMS of 2.0 with a 3% noise floor as well as the anisotropic inversion of the same data that fits to an RMS of 1.3 with the same 3% noise floor. Seafloor receivers are located at about 6 km, 10 km, and 14 km inline.

Not surprisingly, the isotropic model does not fit the data as well and has introduced layering into the model. This is common in inversions when anisotropy is necessary; the isotropic model will create interbedded layers to effectively create bulk anisotropy.

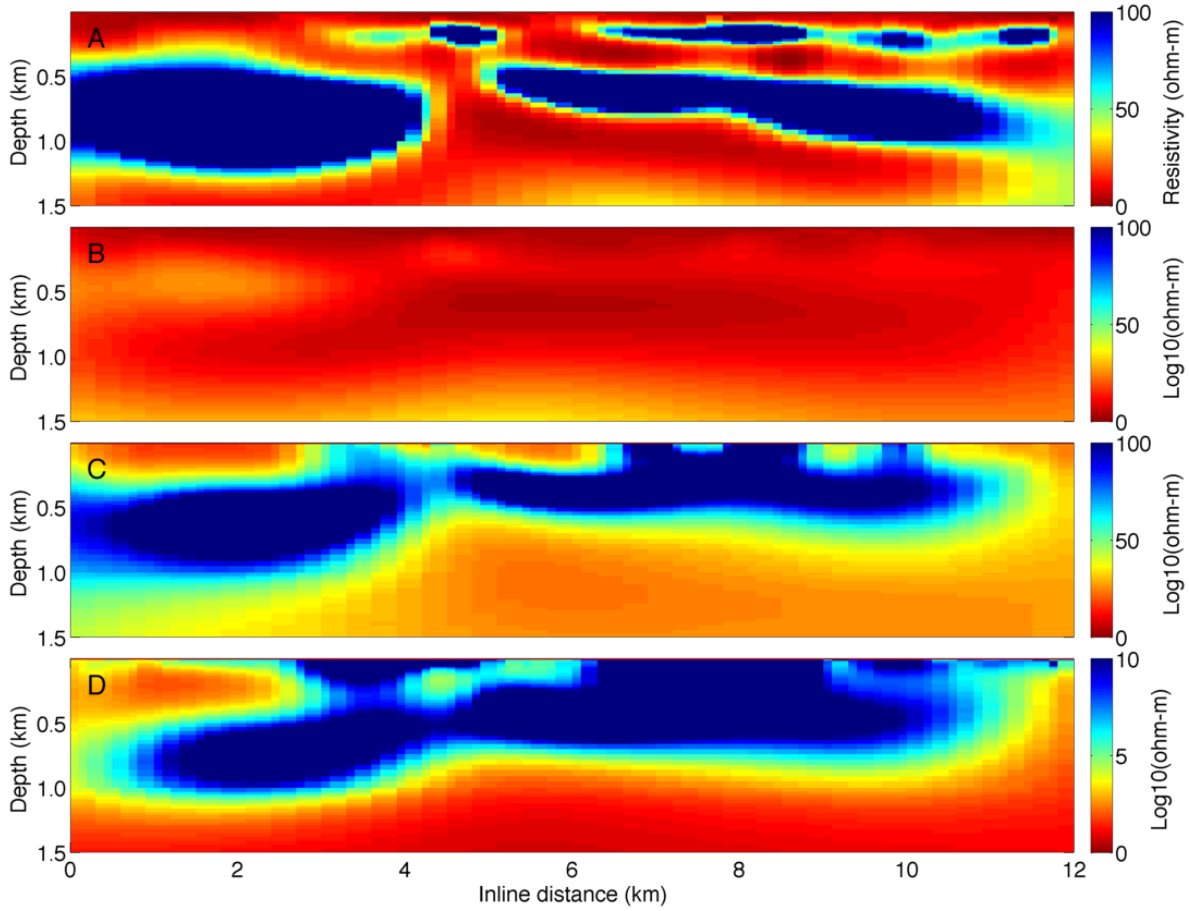

Figure 5.13: Tow 4 from 2015, seafloor receivers only. A. Isotropic amplitude only inversion of seafloor receivers only. Fit to an RMS of 2.0 with a 3% noise floor. B. Horizontal resistivity from anisotropic inversion with amplitude and phase, fits to an RMS of 1.3 with a 3% noise floor. C. Vertical resistivity. D. Ratio of vertical to horizontal resistivity.

However, given that the anisotropy recovered in this data is likely due to interbedded layers of frozen and unfrozen sediment, it is possible that an isotropic inversion could resolve these layers if they are thick enough. Anisotropy necessarily takes over when the layering is too fine to resolve.

We get a better data fit with a highly anisotropic inversion. However, when compared to the Porpoise-only inversion, the isotropic seafloor receiver only inversion seems

more consistent. The shallow layer between 100 m and 400 m depth looks fairly similar to the resistive structure seen by the Porpoise inversion. The anisotropy seems to smooth through these features and create one thick layer of anisotropic material that looks very different from what the Porpoise data is providing. In nearby well logs a similar 2-frozen layer system is seen (*Osterkamp and Payne*, 1981; *Ruppel et al.*, 2016), where there is a layer of IBPF followed by a layer of brine saturated sediment and then another layer of IBPF. If this is the case over much of Tow 4, the porpoise system alone is resolving the top layer only and the addition of seafloor receivers attempts to resolve both. As we saw in Figure 2.2 in section 2.1.2, the porpoise system is typically most sensitive to the top frozen layer and does a poor job of imaging the deeper layer.

Porpoise and seafloor receiver data were combined and inverted jointly, the anisotropic results are shown in in Figure 5.14. We do not have any converged results for an isotropic inversion with both Porpoise and seafloor receiver data. MARE2DEM is not yet set up to evenly weight towed data and seafloor receiver data. Because there are typically more data points associated with a towed array, the Porpoise data will tend to dominate the model. However, in this case there are only about twice as many Porpoise data points and all short offset (<1000 m) data were removed from the seafloor receiver to minimize competition between the two data sets and allow the Porpoises to constrain the shallow portion and seafloor receivers to constrain deeper sections.

Addition of the Porpoise data added more detail in the shallow section, better constrained the conductive marine sediments, and produced a more consistent and shallow base. All inversions including seafloor receivers can resolve structure down to 2 km depth,

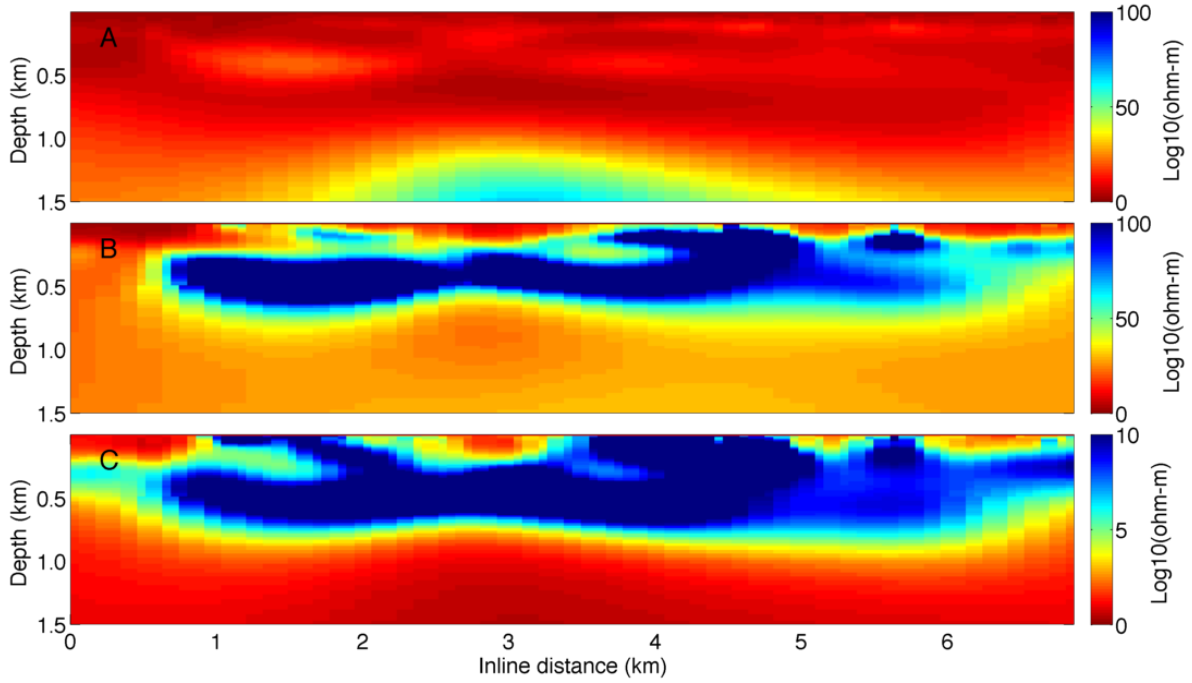

Figure 5.14: Tow 4 from 2015. A. Horizontal resistivity from anisotropic inversion with amplitude and phase from both Porpoise data and seafloor receiver data, fits to an RMS of 1.5 with a 3% noise floor. B. Vertical resistivity. C. Anisotropy ratio of vertical to horizontal resistivity

which means this base near 600 m is well within the bounds of confidence. It has been observed in joint MT and CSEM inversions that better constraining the shallow sections with more data also improves the fit and resolution of features at depth, this is what we see with the base in the joint inversion compared to the seafloor only inversion.

5.1.3 Inversions from Harrison Bay.

A total of four lines were towed in Harrison Bay. Figure 5.15 shows a fence plot of vertical resistivity for all four lines to demonstrate their relative locations. Results in the fence plot are plotted on a logarithmic scale with the same absolute bounds (0 Ωm to 100 Ωm) as the linear scale used previously. Complete anisotropic inversions results from all four lines are in Figures 5.16 and 5.17, all fit to an RMS of 1.0 with a 3% noise floor. Figures 5.16 and 5.17 use a linear scale for resistivity, but because the overall resistivity values are lower in this region the bounds of the color scale have been decreased to 0 Ωm to 20 Ωm.

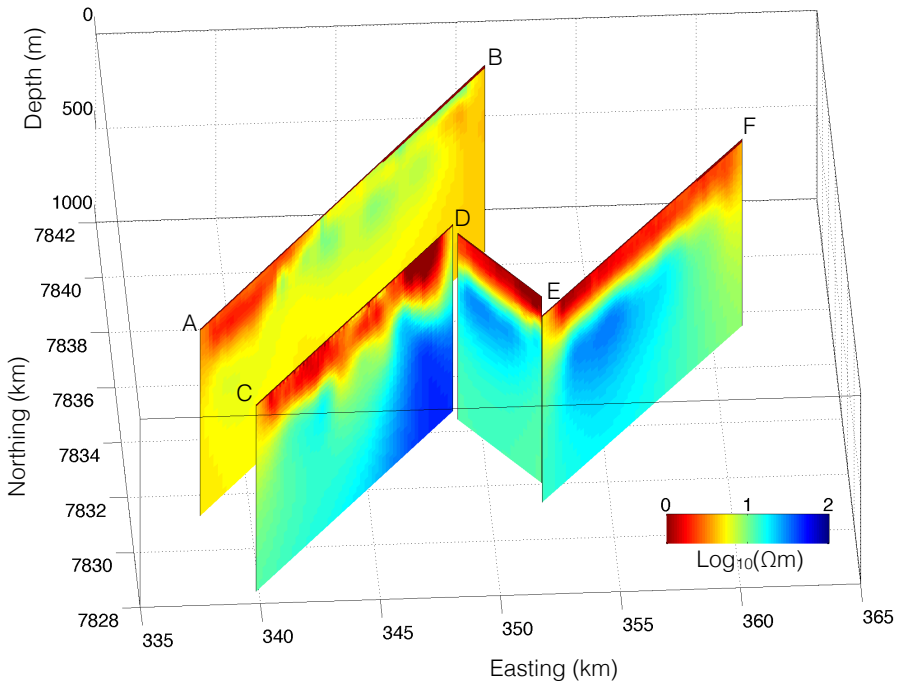

Figure 5.15: Vertical resistivity on a log scale from anisotropic inversion with amplitude and phase of four lines from Harrison Bay. AB is Tow 8, CD is tow 7, DE is Tow 6, and EF is Tow 5.

Examining Figure 5.16 we see that horizontal resistivity is low in shallow regions and increases with depth. It is likely that the increase in horizontal resistivity at depth is driven by the inversion regularization. The preferred anisotropy ratio is 1, which means as the inversion loses resolution the vertical and horizontal resistivity are driven towards the same value. The most horizontally resistive part in Tow 7 corresponds with the deeper resistive feature in the vertical resistivity.

Note the lack of resistive features in Tow 8; there is no point on this line that reaches above 10 Ωm, implying that there is no or only low saturation ice-bonded permafrost present. Lines 5-7 peak between 20 and 30 Ωm, which is still dramatically lower than the peak values of over 1000 Ωm seen in inversions from the Prudhoe Bay region. Depth to top of permafrost is also deeper here. Differences in peak resistivity and depth to the top of permafrost between here and the Prudhoe Bay region suggest there is less permafrost here, which could be due to finer sediment grains preventing ice formation or due to heat input from the Colville River.

This section of Harrison Bay is near the Colville River outflow, but offset to the west of the main confluence. We do not see the same dramatic increase in resistivity and shallowing of permafrost as we did offshore the Sag River, and in fact see the opposite effect, a decrease in permafrost presence. This could mean we collected data over a talik, an unfrozen section in otherwise continuous permafrost, in a paleo river channel of the Colville, which is a large enough river to prevent permafrost formation beneath its bed. The data we collected in Harrison Bay, including where no IBPF was detected, is near the location of increased methane venting measured by *Pohlman et al.* (2012). This lends support to

modeling done that suggests taliks in paleo river channels provide venting pathways for methane gas in otherwise continuous, and therefore impermeable, ice-bonded permafrost (*Frederick and Buffet*, 2014).

All inverted lines are presented in Appendix A and B.

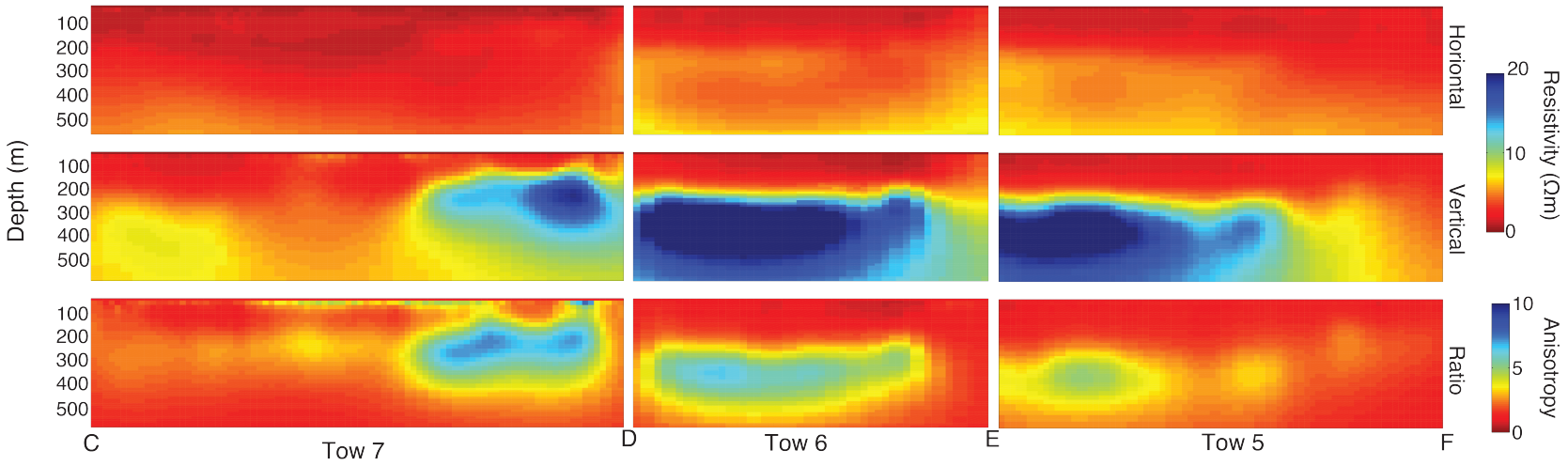

Figure 5.16: Tows 5, 6, and 7 from Harrison Bay. Resistivity is on a linear scale, note the color scale is now from 0 to 20 Ωm instead of to 100 Ωm.

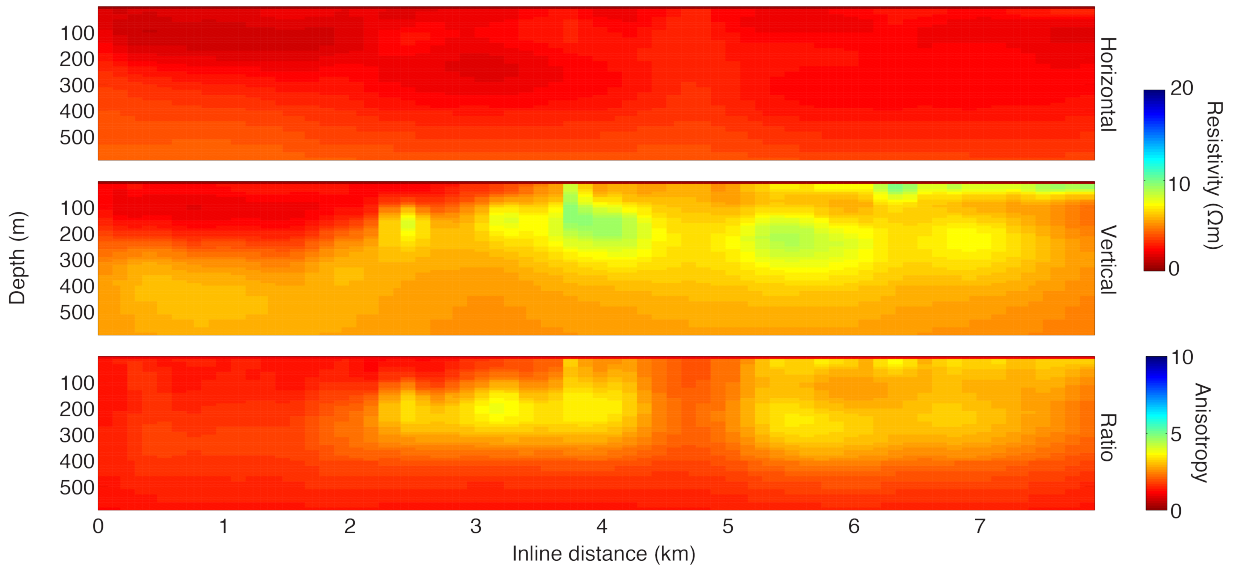

Figure 5.17: Tows 8 from Harrison Bay. Resistivity is on a linear scale and the maximum resistivity is less than 10 Ωm. Note the color scale is now from 0 to 20 Ωm instead of to 100 Ωm

5.2 Perturbation analysis

Assigning appropriate uncertainties to data is a key part of allowing the inversion to create a model without being too influenced by outliers. To understand the noise structure of the Porpoise system we conducted a perturbation analysis using the DIPOLE1D forward code (*Key*, 2009). For a given halfspace we calculate changes in the electric field for variations of navigation and environmental parameters: azimuth, crossline distance, range, antenna dip, sea water conductivity, transmitter depth, pitch, roll, and heading. Results for a 1 Ωm halfspace are plotted in Figure 5.18.

Errors are higher at shorter offsets and tend towards a constant value after 1500 m for a 1 Ωm halfspace. Biggest contributors to errors are variation in range and seawater conductivity. The resulting error in amplitude from a 10 m change in range is an order of magnitude larger than any other parameter, note that range error has been divided by ten for plotting in Figure 5.18. Seawater conductivity was divided into two layers, based on our ocean conductivity measurements the top two meters varied between .3 and .5 Ωm with the bottom layer maintained at .4 Ωm. Ten degree changes in pitch, roll, and heading have no effect on phase and a mostly constant error in amplitude near 1.5%.

A towed system offers a few advantages in terms of navigation errors. One is that the parameter inducing largest errors, range, is fixed by a rope. Another is though the Porpoises dive up and down with wave motion, pitch averages to zero. Based on the 1 Ωm halfspace, maximum errors are within 4% of amplitude and 2° phase, which supports the 3% noise floor we used in our inversions. As the resistivity of the halfspace increases the

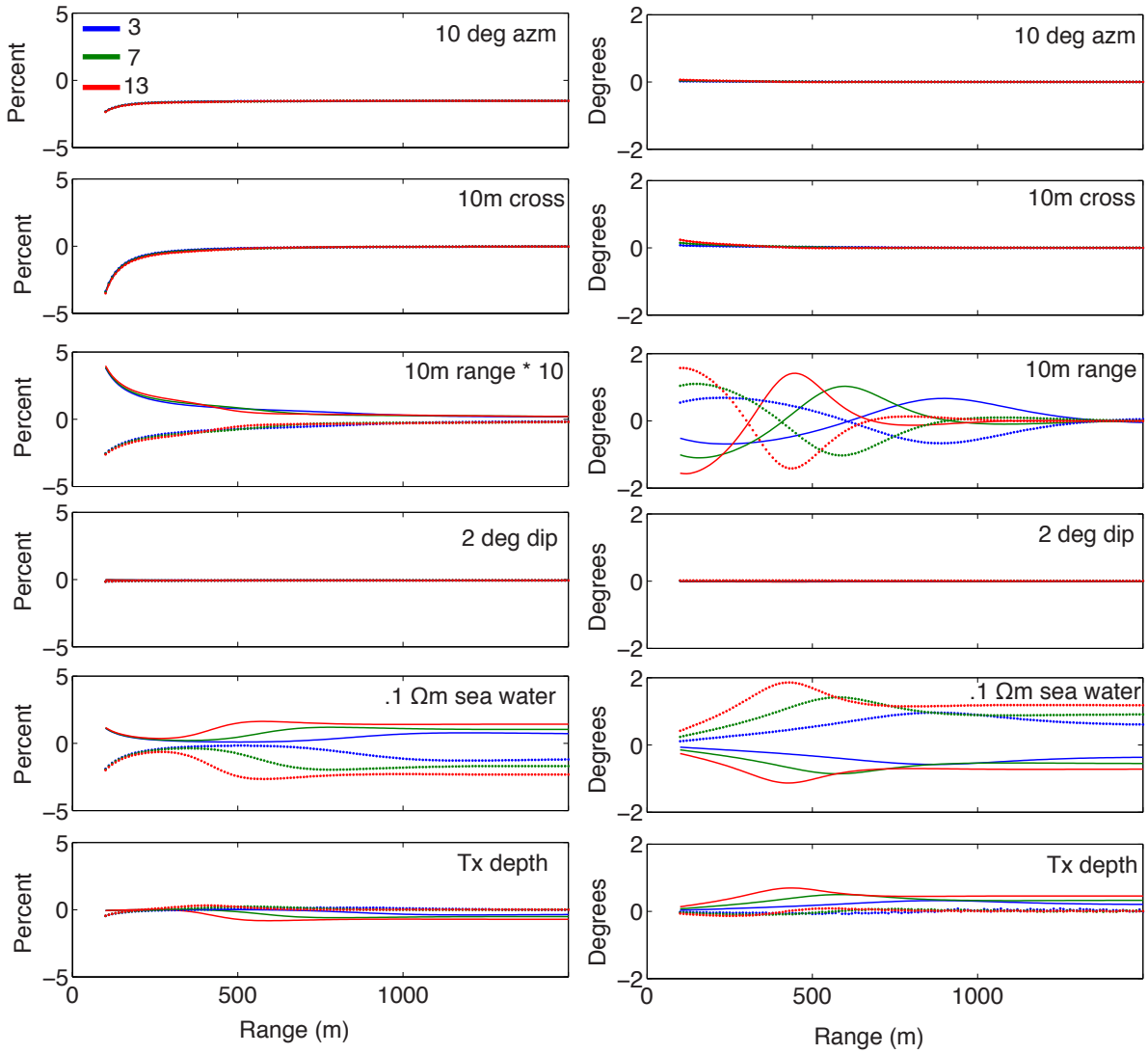

Figure 5.18: At three frequencies the percent error or degree error introduced to amplitude and phase data, respectively, for each parameter.

impact of the seawater conductivity grows, while range variations decrease. We continually measured seawater conductivity at the surface, but due to shallow water depths, the thin ocean layer in the inversion was difficult to efficiently mesh. For inversions, we therefore let the ocean conductivity be a free parameter bounded by our measured conductivity.

5.3 Effects of anisotropy on resolution

As with all inversions, the question of resolution and sensitivity are paramount to understanding the results. There is a distinct difference between the two; data may be sensitive to structure at depth but without the ability to resolve its size and location. In the anisotropic inversions presented in the previous section, anisotropy ratio provides a clear base to the permafrost layer. However, this may be largely data driven or mostly driven by the model regularization. In an attempt to understand how anisotropy influences depth resolution, we conducted a 1D synthetic study.

A series of 3-layer permafrost models were made, all buried 100 m deep under 1 Ωm marine sediments, with a permafrost layer resistivity of 100 Ωm and thicknesses ranging from 100 m to 800 m. Forward calculations were run for these isotropic models, gaussian noise added, and the data inverted. The data structure was chosen to represent the Porpoise system, only one transmitter was used with four receivers at offsets of 250 m, 500 m, 750 m, and 1000 m and at three frequencies, 3 Hz, 7 Hz, and 13 Hz. The isotropic results are shown in Figure 5.19 and the 1D inversion can detect the permafrost base down to 700 m (thickness of 600 m), which is deep enough to detect all offshore permafrost. After

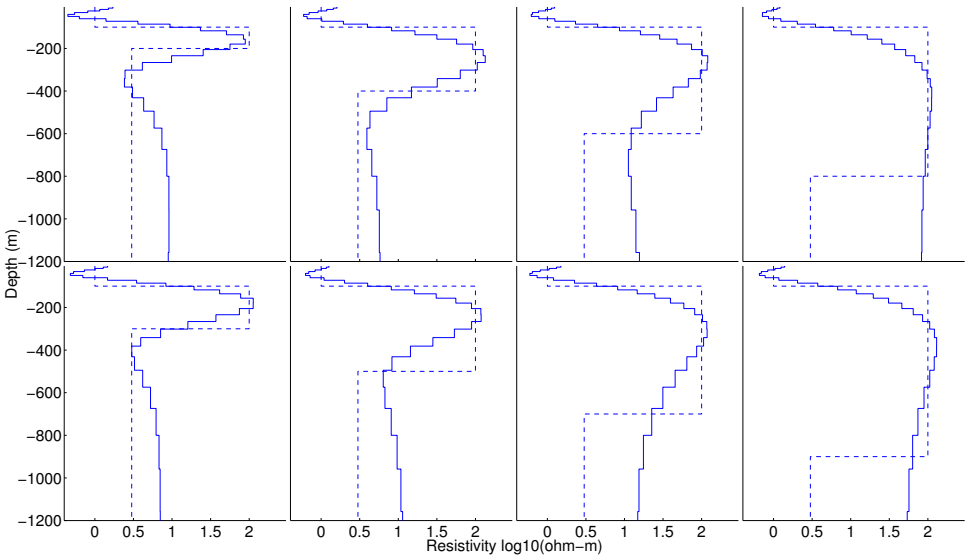

Figure 5.19: 1D Occam inversion results for an isotropic model with increasing permafrost layer thicknesses from 100 m to 800 m.

resolution is lost in isotropic models, the regularization maintains high resistivity values well past the base of permafrost. Therefore, if a base is detected with an isotropic model it is likely real and not an artifact of inversion regularization.

The same process was used with anisotropic inversions, the true models now have an anisotropic permafrost layer with a vertical resistivity of 100 Ωm and horizontal resistivity of 5 Ωm. Results are shown in Figure 5.20 and they imply that the anisotropy reduces our ability to resolve the base. The anisotropy ratio consistently resolves the sharp top boundary better than the isotropic inversions, but does a poorer job of capturing the other characteristics of the permafrost layer.

A summary of both studies is shown in Figure 5.22, which plots true base depth against final inversion model base depth with a "perfect" model shown as a dashed line. We defined the base for isotropic models as the transition to 10 Ωm beneath the resistive

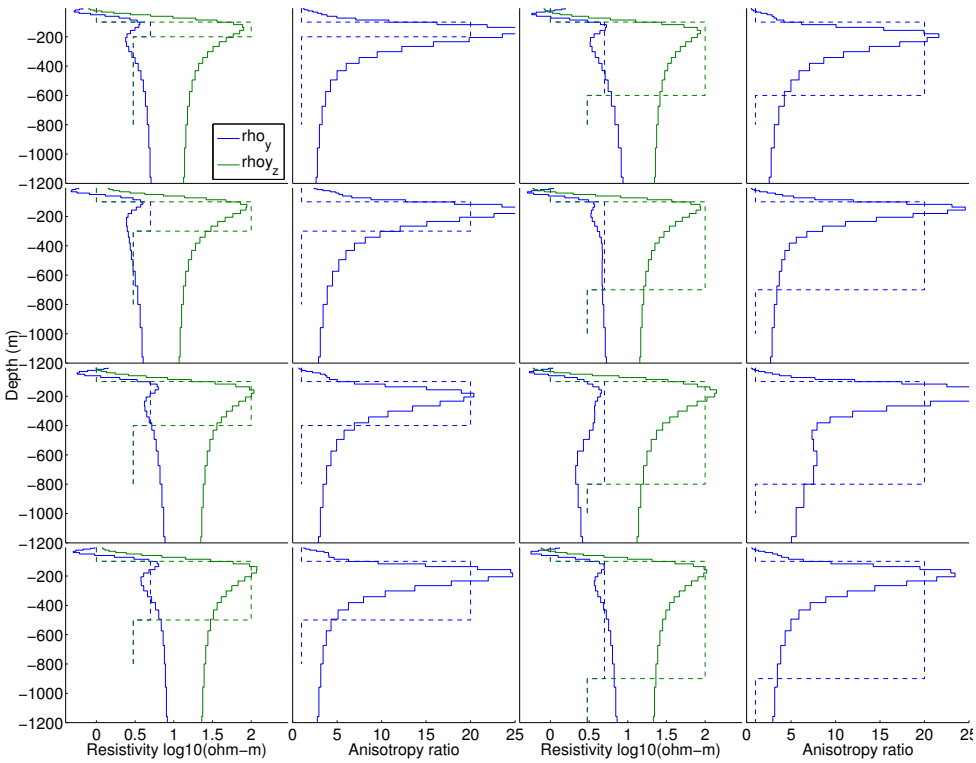

Figure 5.20: 1D Occam inversion results for an anisotropic mode with increasing permafrost layer thickness from 100 m to 800 m. Vertical (blue) and horizontal (green) resistivity is plotted along with the true model, anisotropy ratio is plotted along with the true model in a separate panel.

layer. Base for anisotropy inversions was defined using the anisotropy ratio, an anisotropy ratio of 10 was used based on behavior we observed in our EM inversions from Prudhoe Bay. Isotropic inversions detect a correct base depth through 400 m, and then begins to underestimate the base until it can no longer detect any base at 800 m. Anisotropy produces a consistent 200 m thick layer (base of 300 m) regardless of the models true thickness.

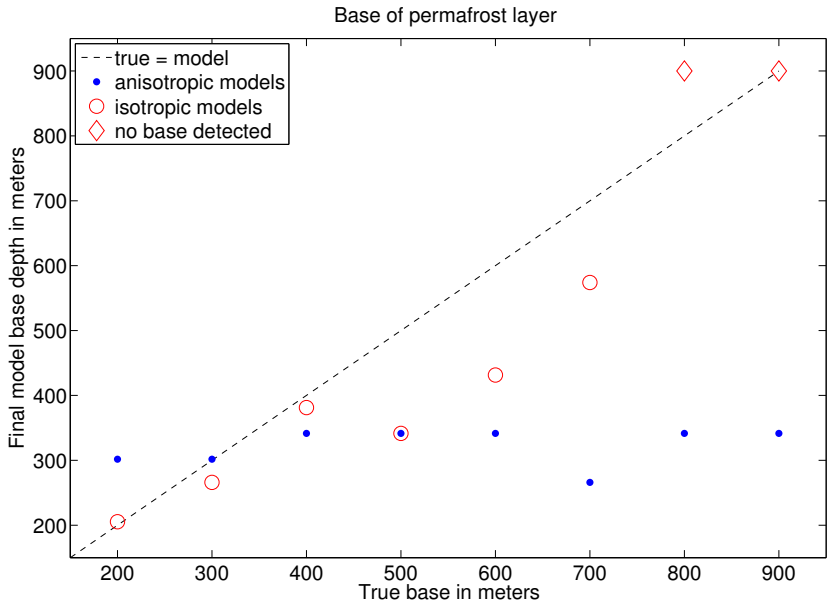

Figure 5.21: Bases detected for both anisotropic and isotropic 1D synthetic models.

Even though our 1D synthetic models indicate anisotropic inversions detect an initial resistivity contrast only, 2D anisotropic results of real data suggest otherwise. As has been seen in previous results, the 2D models detect different thicknesses and degrees of permafrost. The different behavior between 1D and 2D modeling is most likely because the 1D synthetic inversions used very little data (12 points), as opposed to the hundreds or thousands of data points in a 2D problem. Additionally the data points in a 2D problem

are not entirely independent, allowing for better resolution of a 1D model with a 2D inversion. Possibly due to these reasons, or some other flaw in the 1D model, the 1D synthetic study is not capturing the information provided by 2D inversions and is not a good representation of resolution in 2D. To demonstrate this, a similar set of 3-layer models was put together as 2D models and inverted after adding random gaussian noise to the forward problem solution.

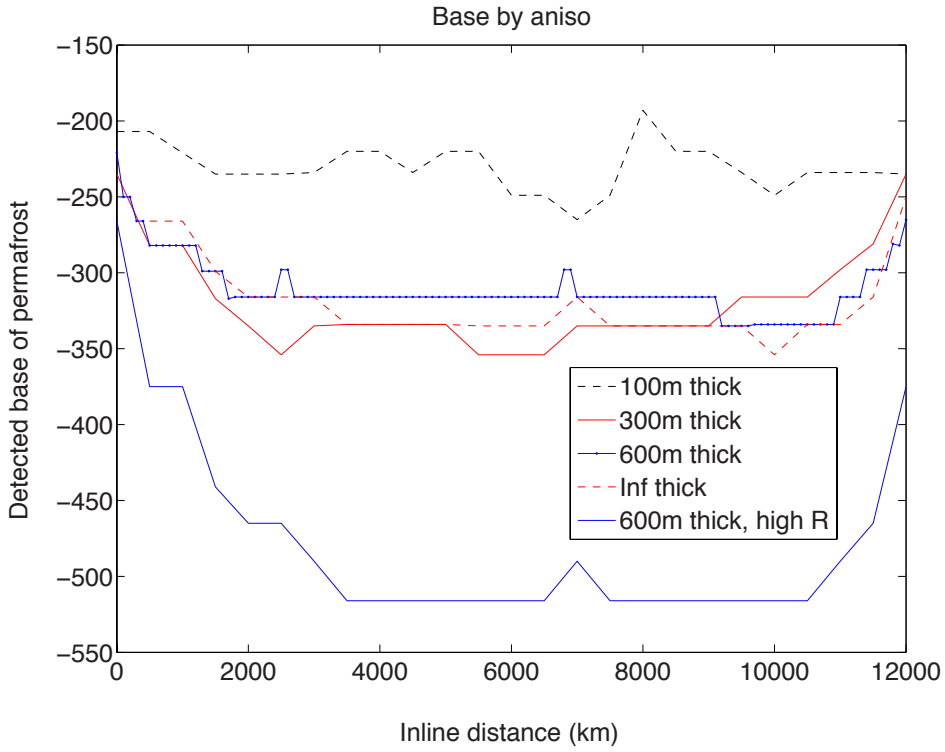

Figure 5.22: Bases detected for anisotropic 2D synthetic models.

For a permafrost layer with vertical resistivity of 100 Ωm and horizontal resistivity of 5 Ωm, a 2D inversion can differentiate between layers 100 m and 200 m thick (base depths of 200 m and 300 m respectively). Thicknesses of 600 m and an infinitely thick layer both produce a base of also 300 m, suggesting 300 m is the maximum depth of sensitivity of the

Porpoise system. Changing the resistivity of the permafrost layer to 600 Ωm in the vertical direction and 100 Ωm in the horizontal direction dramatically alters this base depth. For the 600 m thick model the increase in resistivity produces a base of 550 m (when the true base is 700 m), a value much closer to the truth. As would be expected because of skin depth, the maximum depth of resolution is highly dependent on the resistivity. However, further increases in resistivity of the permafrost layer does not improve the resolution of the 600 m base, suggesting that geometry (source-receiver offsets) control the absolute maximum depth we can resolve.

Our CSEM data produced models indicating permafrost is highly resistive, reaching resistivities over 1,000 Ωm, and anisotropic, most likely due to the presence of multiple freeze-thaw horizons. Shallow and highly resistive permafrost was indicated offshore the Sagavanirktok River outflow just east of Prudhoe Bay, while Harrison Bay was characterized by lower resistivities. We used a perturbation analysis to estimate reasonable errors for Porpoise data and used this to inform our inversion noise floor and decision to let the ocean layer be a bounded free parameter. Synthetic studies indicate that anisotropy reduces the Porpoise systems ability to resolve the base of IBPF.

Portions of the text in Chapters 5 and 6, are being prepared for publication. The dissertation author is the first author of the work preparation; the coauthor on the publication is Steven Constable who supervised the research.

Bibliography

Archie, G. E. (1942). The Electrical Resistivity Log as an Aid in Determining Some Reservoir Characteristics. *J. Petrol. Tech. 146*(1)p. 54-62

Collett, T.S., K.J. Bird, K.A. Kvenvolden, and L.B. Magoon (1989), Map showing the depth to the base of the deepest ice-bearing permafrost as determined from well logs, North Slope, Alaska: USGS Oil and Gas Investigations Map 222.

Cook, A.E., B.I. Anderson, J. Rasmus, K. Sun, Q. Li, T.S. Collett, and D.S. Goldberg. (2012) Electrical anisotropy of gas hydrate-bearing sand reservoirs in the Gulf of Mexico. *Mar. Petrol. Geol. 34*, 72-84

Constable, S.C. (2013) Review paper: Instrumentation for marine magnetotelluric and controlled source electromagnetic sounding, *Geophys. Prospect.*, *62* 573-593

Constable, S. C., P. Kannberg, K. A. Weitemeyer (2016) Vulcan: A deep-towed CSEM receiver, *Geochem. Geophy. Geosy.*, *17*, 1042-1064

Frederick, J. M., and B. A. Buffett (2015), Effects of submarine groundwater discharge on the present-day extent of relict submarine permafrost and gas hydrate stability on the Beaufort Sea continental shelf. *J. Geophys. Res. Earth Surf.*, *120*, 417432

Frederick, J. M., and B. A. Buffett (2014), Taliks in relict submarine permafrost and methane hydrate deposits: Pathways for gas escape under present and future conditions, *J. Geophys. Res. Earth Surf.*, *119*, 106 -122

Key, K. W. (2016). MARE2DEM: a 2-D inversion code for controlled-source electromagnetic data. *Geophys. J. Int.*, *207*, 571-588

Key, K. (2009) 1D inversion of multicomponent, multifrequency marine CSEM data: Methodology and synthetic studies for resolving thin resistive layers, *Geophysics*, *74*, F9-F20

Myer, D., S. C. Constable, K. W. Key (2010), Broad-band waveforms and robust processing for marine CSEM surveys. *Geophys. J. Int.*, *184*, 689-698.

Osterkamp, T.E., and M.W. Payne, (1981) Estimates of permafrost thickness from well logs in northern Alaska. *Cold Reg. Sci. Technol.*, *5* 13-27

Pohlman, J., C. Ruppel, C. Maue, L. Brothers, J.Kessler, and C. Worey. (2012). Real-time mapping of seawater and atmospheric methane concentrations offshore of Alaska's North Slope. *USGS Sound Waves*, 140, 4-5

Ruppel, C.D., B.H. Herman, L.L. Brothers, and P.E. Hart (2016) Subsea ice-bearing permafrost on the U.S. Beaufort Margin: 2. Borehole constraints, *Geochem. Geophy. Geosy.*, *17*, 4333-4353. doi:10.1002/2016GC006582.

Chapter 6

Maps and logs

Inversions results were presented in the last chapter and are used in this chapter to produce plan maps of permafrost extent. Results are compared in detail to borehole measurements and thermal implications of our observations are discussed.

6.1 Maps of permafrost distribution

The Occam inversion approach described in Section 2.2 can be used to create smooth interpolated maps of irregularly spaced data. This is a linear inversion problem where the forward solution is simply the data values. We opted to use the mechanics of an Occam inversion instead of using other interpolation algorithms because the Occam approach allows for uneven distribution of data, repeated values, and user control over what areas in the model have assigned values and how well the model fits the data. A target RMS, errors assigned to data values, size of model grid, and distance from nearest data

point to extrapolate are all user chosen. We use first derivative roughness to regularize the inversion which makes the model go flat in areas with no data.

Using the EM inversion model resistivities and this Occam mapping approach, we create maps of permafrost characteristics to better picture the lateral changes. Depth to the 10 Ωm contour is chosen to represent the top of frozen sediments. We chose this value because *Ruppel et al.* (2016) has defined offshore borehole resistivity measurements of over 100 Ωm as high saturation ice-bonded permafrost, we also know that marine sediments are about 1 Ωm, which means given our inversion regularization 10 Ωm is the transition point between the two values. Additionally, with few exceptions, the resistivity value below the base of permafrost is below 10 Ωm, and areas of 10-50 Ωm are interpreted by Ruppel as intermediate saturated ice-bonded permafrost. This suggests that depth to 10 Ωm contour is a reasonable place to indicate the start of permafrost.

Depth values were derived from inversion results for all lines, and resulting easting, northing, and depth points were interpolated to find a smooth map on a grid showing the depth to permafrost, Figure 6.1. In this map the model grid is 700 m by 700 m, data errors are 10 m, and data is fit to an RMS of 2.0. Range of depth is from 0 to 465 m, with an average of 169 m. This is comparable to the range of 5 m to 470 m with an average of 195 m found in refraction seismic data of *Brothers et al.* (2012).

Plotted on top of the map are depth to the top of permafrost seen in boreholes offshore or on the barrier islands, taken from *Ruppel et al.* (2016). West of Prudhoe Bay there is a discrepancy between the borehole logs indicating IBPF starting near the surface on two barrier islands while the shoreward EM data indicates IBPF under 150 m - 220 m

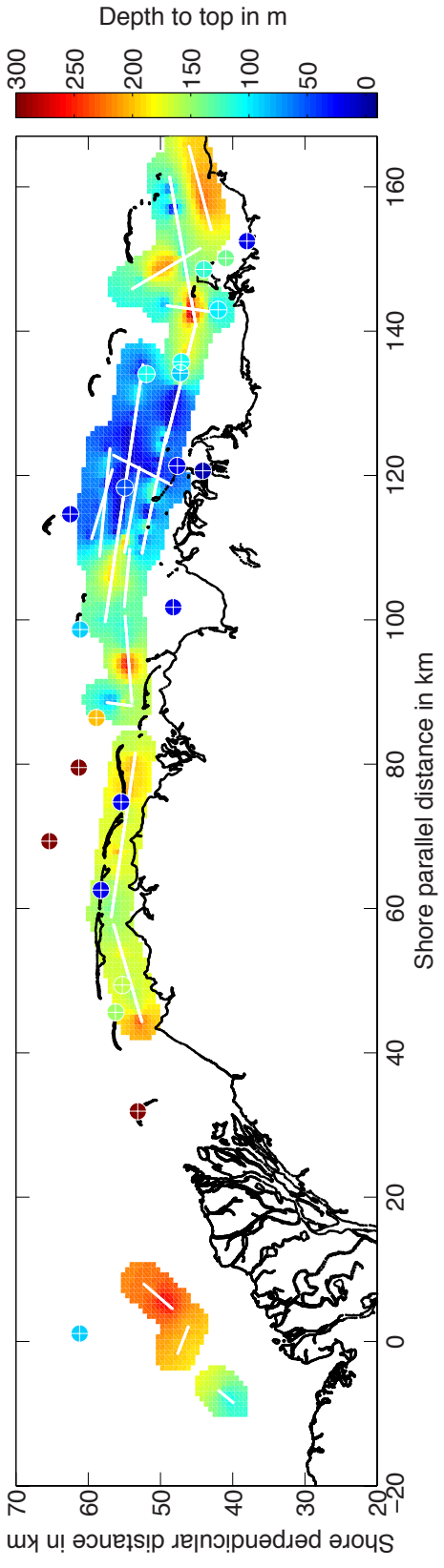

Figure 6.1: Map of depth to top of permafrost as defined by the 10 Ωm contour. Blue indicates shallower permafrost and red is deeper. On top of the map derived from EM results, depths to top of permafrost as seen in well logs (*Ruppel et al.*, 2016) are plotted as circles on the same color scale with white crosshairs.

of unfrozen sediment. This difference is likely due to the fact that islands provide some atmospheric coupling and may preserve very shallow permafrost. Long Island (further east) has a thin layer of intermediate-saturation IBPF then a gap of no IBPF until 210 m depth, which is consistent with the EM data. Jones Island (further west) also has a thin layer of high-saturation IBPF right at the surface with intermediate-saturation IBPF not starting until 80 m depth. If these thin surface layers are due to exposure to air then they would not be present in the submerged IBPF, bringing the EM results and well logs into better agreement at these two locations.

Logarithmic peak resistivity values from inversions are mapped in Figure 6.2. The map used an RMS of 10 with 3% errors and the same 700 m by 700 m model grid as Figure 6.1. A higher RMS was chosen for this map because the data required more smoothing to not appear overfit. Mean peak resistivity is 70 Ωm with a standard deviation of 102 Ωm and minimum and maximums of 4 Ωm and 1500 Ωm respectively.

Note the presence of an extra line in Harrison Bay, these data did not contribute to the Figure 6.1 because the peak resistivity is below 10 Ωm, indicating that there is no permafrost on this line. From both of these maps we see that permafrost tends to be less resistive and deeper east of Prudhoe Bay towards Harrison Bay. Permafrost in the region of the Sag River outflow is shallower than the highly resistive section further west. This is consistent with what is known about the lithology of the area, Prudhoe Bay and the ANWR have younger and coarser sediments than the NPRA and the younger sediment sequences thin from Prudhoe Bay eastward (*Osterkamp and Payne* , 1981; *Collett et al.*, 1989).

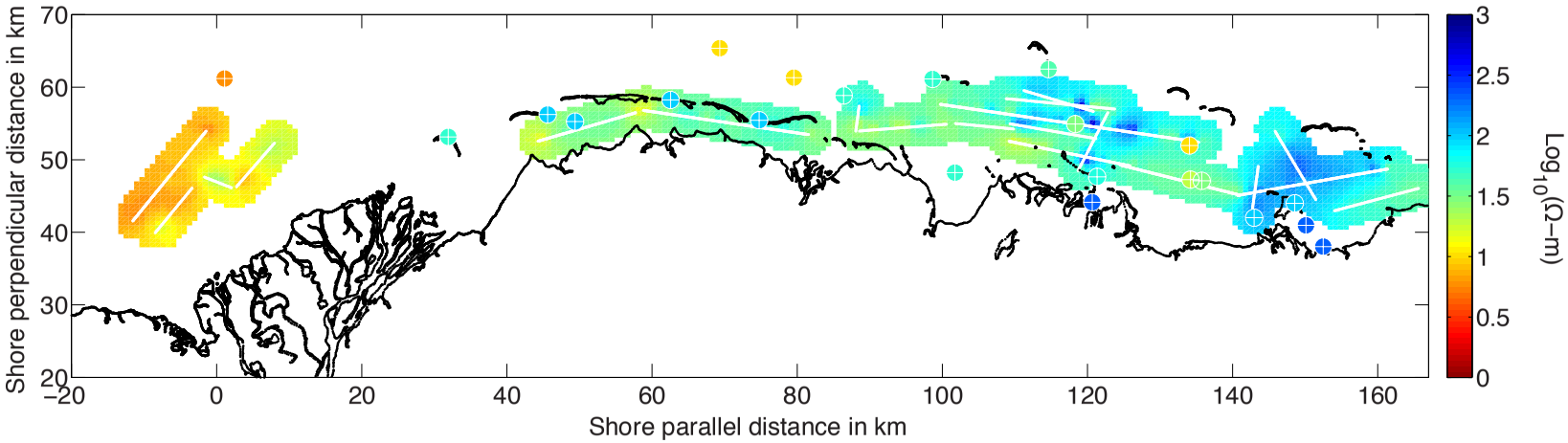

Figure 6.2: Map of peak logarithmic vertical resistivity, blue indicates more permafrost. On top of the map derived from EM results, peak resistivities as seen in well logs (*Ruppel et al.*, 2016) are plotted as circles on the same color scale with white crosshairs.

A map of resistivity can also be seen as a map of ice saturation, with higher resistivity values correlating with higher ice concentrations. Based on Archie's law and *King et al.* (1988), ice saturation can be used to compute the ratio of frozen sediment to unfrozen sediment as $R_f/R_i = S_w^{1-n}$, where R_f and R_i are resistivities of the frozen and unfrozen ground respectively, S_w is water saturation and n is an empirical parameter that is usually assumed to be 2 if no better data are available. We can rearrange this to obtain ice saturation, $S_{ice} = 1 - R_1/R_f$. We can take our unfrozen resistivity as 10 Ωm, because this is the maximum resistivity we are considering unfrozen, and the frozen resistivity as peak vertical resistivity to yield peak ice concentration.

Using peak vertical resistivity yields peak ice concentrations with a mean of 76% and a standard deviation of 14%, a maximum of 99% and a minimum of 5%. Only 2.4% of peak resistivity data points have ice saturation of less than 40%, which *King et al.* (1988) and *Brothers et al.* (2012) have indicated as the saturation at which geophysical parameters such as seismic velocity and resistivity increase dramatically as the sediment begins to cement and form ice-bonded permafrost. Archie's law is for isotropic material and it is not valid for the anisotropic permafrost layer. This is why we have not attempted an average ice concentration, but by using the vertical resistivity values we can obtain an ice concentration of an isotropic permafrost layer at that resistivity value which gives us the maximum possible ice concentration given our EM inversion results.

The biggest discrepancy between peak resistivities on Tow 3 and resistivities measured in boreholes is at the Karluk well log. Beechey Point, Tern A1, and Liberty are in better agreement. But in all cases the EM inversions are indicating higher resistivities than

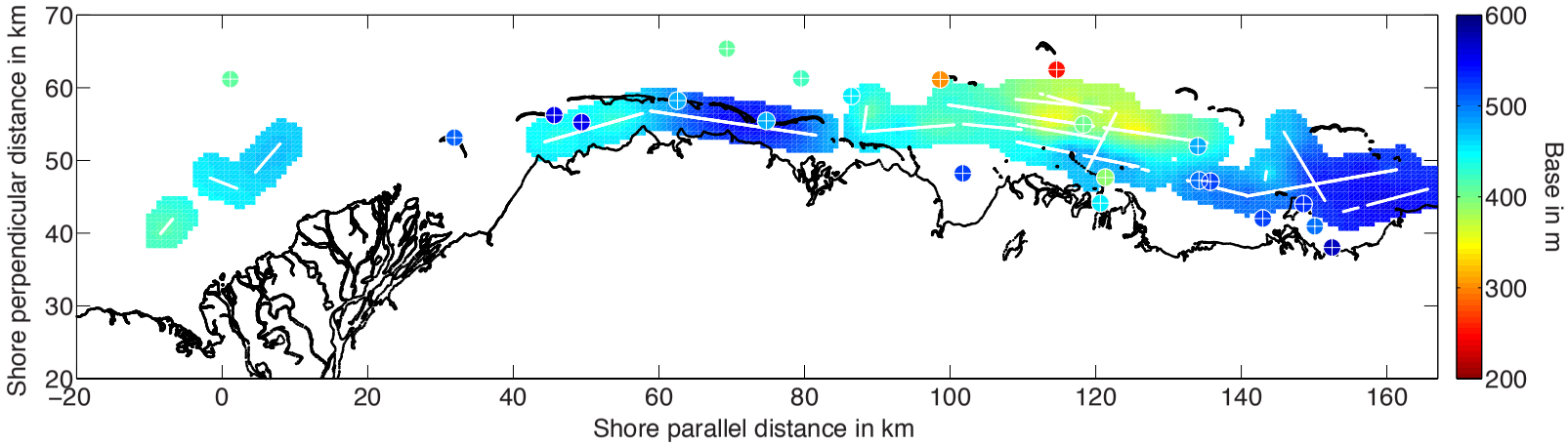

Figure 6.3: Map of depth to base of permafrost. Blue indicates deeper base. On top of the map derived from EM results, depths to base of permafrost as seen in well logs (*Ruppel et al.*, 2016) are plotted as circles on the same color scale with white crosshairs.

are being measured from well data. The high resistivity zones are patchy and the boreholes from *Ruppel et al.* (2016) are near parts of Tow 3 with lower resistivity values (in the range of 30-60 Ωm instead of over 100 Ωm). Values for borehole peak resistivity were visually estimated from printed records, making them not very robust and likely underestimated in an attempt to be conservative. Additionally, the induction tools used in the well logs measure horizontal resistivity, so we expect our vertical resistivities to be higher because of anisotropy. A potential issue that could bias EM results, and not boreholes, are pipelines or other large metal infrastructure in the area, which would re-radiate EM energy and appear as resistors in Porpoise data. Towing parallel to a pipeline would not produce any obvious artifacts, but would artificially raise amplitude and therefore resistivity values. However, as far as we know there are no pipelines in this area.

Deciding on the best determination of the base of permafrost was not trivial. The second 10 Ωm contour was chosen as the base for isotropic inversions for the same reason it was chosen as the top of permafrost. With only a few exceptions offshore boreholes indicate resistivity values beneath permafrost of 1-5 Ωm, indicating the transition point at the base should be similar to at the top. Anisotropy gives the clearest and sharpest contrast where we expect the base to be, but values of anisotropy are also the most variable across lines, making the choice of a single appropriate value inappropriate.

To accommodate this line to line variability, base was chosen to be the midway point between maximum values of anisotropy and the minimum value beneath the permafrost layer before loss of sensitivity for anisotropic inversions. The inversion regularization penalizes the difference between horizontal and vertical resistivity; therefore, the anisotropy

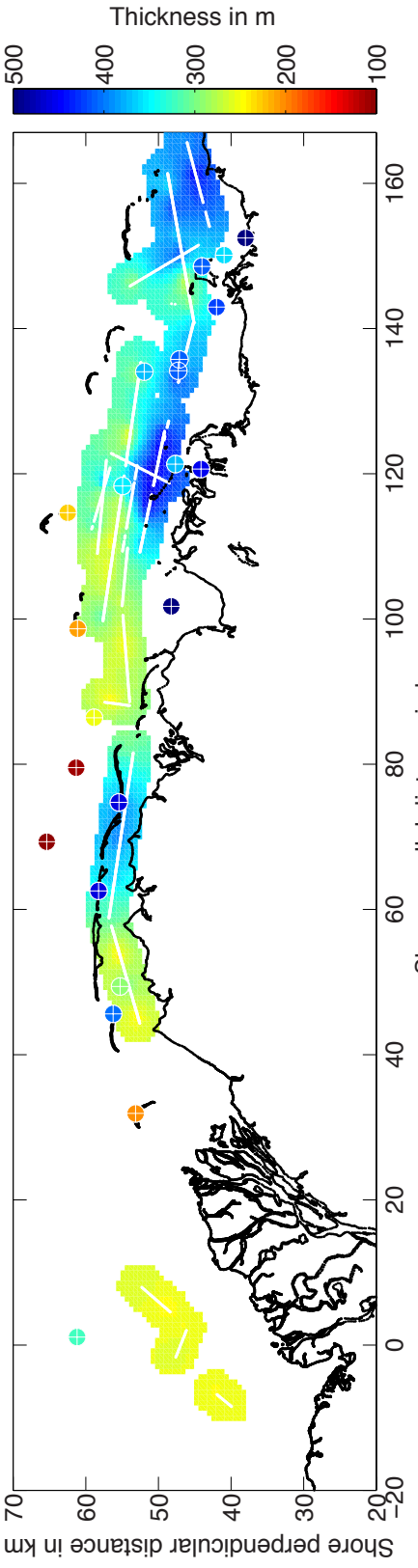

Figure 6.4: Map of thickness of permafrost, blue is thicker permafrost. On top of the map derived from EM results, thicknesses of permafrost as seen in well logs (*Ruppel et al.*, 2016) are plotted as circles on the same color scale with white crosshairs.

ratio will smoothly decay from its peak value towards one after we lose resolution. We therefore take the value of anisotropy midway between the peak value and the minimum value achieved above our maximum depth resolution to be the base of IBPF. The base depth is cut off at 600 m because we know this to be our maximum depth resolution from synthetic studies.

The resulting map of depth to base of permafrost is shown in Figure 6.3. Data gaps occur in areas where no permafrost base was resolved. Depth to base of permafrost derived from EM inversions has a mean value of 435 m, with a standard deviation of 90 m, and a maximum base depth of 593 m. The deepest base of permafrost seen in offshore boreholes is 570 m and is near Tigvariak island in the same area the EM results indicate deep, thick permafrost.

Lastly, the depths to top and base to permafrost can easily be made into permafrost thickness. This is done in Figure 6.4. Thicknesses are typically between 200 m to 500 m. Mean thickness is 313 m with a standard deviation of 89 m and a maximum thickness of 562 m. Areas with the thickest permafrost also tend to have highest peak resistivities, specifically offshore the Sagavanirktok River and east of Tigvariak Island. Agreement between boreholes and EM inversion results is good, despite 1D models in the previous section suggesting anisotropy prevents us from resolving the base of permafrost. Figure 6.4 shows we can provide a reasonable estimate of the base of permafrost, so long as we take into account inversion regularization in our definition of the base.

6.1.1 Gas Hydrate Stability Zone

Gas hydrates are ice-like structures that form when hydrogen bonds between water molecules form cages around gases under high pressures and low temperatures. Natural gas hydrates occur predominantly beneath the seabed of the continental margins, where ocean bottom temperatures are just above 0°C and hydrostatic water pressure is great enough to make gas hydrates stable (typically at least a few hundred meters water depth). Gas is typically methane formed by biological activity or leaking from hydrocarbon systems, but can also contain longer chain hydrocarbons such as ethane and propane. Gas hydrates may persist beneath the surface until the temperature rises to above the hydrate stability zone due to heat from the geothermal gradient. A gas hydrate stability curve is plotted on a temperature-pressure plot, for natural gas hydrates the pressure axis is typically converted to depth below the surface by assuming hydrostatic pressure. Plotting the geothermal gradient on the same axes shows the pressures and temperatures at which gas hydrate is stable in the area above the geothermal gradient and below the gas hydrate stability curve (see Figure 6.5).

The presence of permafrost depresses the 0°C isotherm, allowing colder temperatures to exist deeper beneath the surface. The cold temperatures in Arctic environments allow gas hydrates to exist in shallow water, and on land, in permafrost regions even at relatively low pressures. The impermeable ice-bonded permafrost also provides a cap to trap any free gas below the frozen layer, but within the gas hydrate stability zone, increasing the likelihood of hydrate formation. Because it is the permafrost cap that maintains

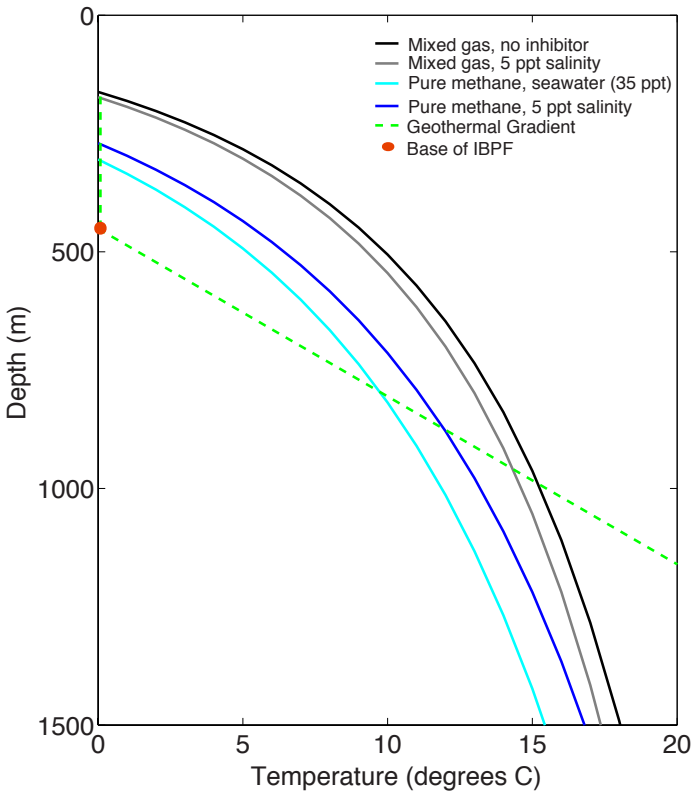

Figure 6.5: Gas hydrate stability curves, calculated with Colorado School of Mines program (*CSMHYD*, 2018), for pure methane and seawater, pure methane and brackish water, a mixture of gases and brackish water, and a mixture of gases and pure water. The region above the geothermal gradient and below the gas hydrate stability curve is the range of temperatures and pressures at which gas hydrate is stable.

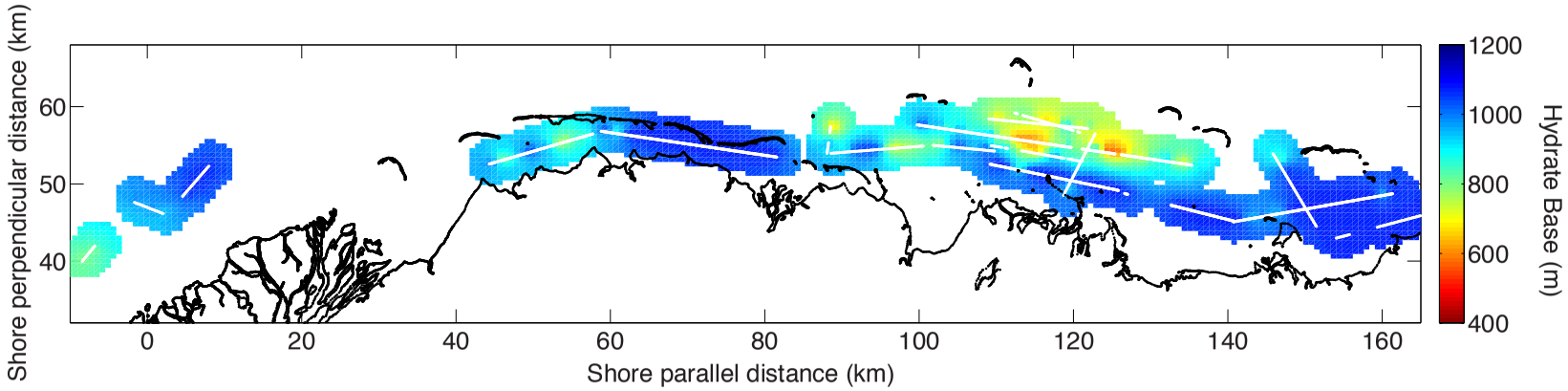

Figure 6.6: Map of gas hydrate stability zone, based on gas hydrate stability curve for water with 5 ppt salinity (*Tishchenko et al.*, 2005), permafrost thickness determined by CSEM data, and a 28.2°C/km geothermal gradient (*Lachenbruch et al.*, 1982).

near or below freezing temperatures at depth, the gas hydrate stability zone in Arctic environments is dependent on the thickness of the permafrost layer (*Holder et al.*, 1987; *Collett et al.*, 2011).

Figure 6.5 shows a range of pressure-temperature gas hydrate stability curves with temperature in degrees Celsius and pressure converted to depth by assuming a hydrostatic pressure of 9.795 kPa/m (*Collett et al.*, 2011; *Holder et al.*, 1987). In Figure 6.5 shades of blue represent 100% methane hydrates, the cyan curve is for pure methane hydrate with a water salinity of 35 ppt (seawater) and the blue curve is for pure methane with a water salinity of 5 ppt (slightly brackish). Shades of gray are for mixed gas hydrates with a composition of 98% methane, 1.5% ethane, and 0.5% propane (*Collett et al.*, 2011; *Holder et al.*, 1987), the light gray curve is for mixed gas hydrate and water with a salinity of 5 ppt and the black curve is for mixed gas hydrate and water without an inhibitor (pure fresh water). Gas hydrate stability curves were generated using the Colorado School of Mines program available online, and is very similar to the empirical equation given in *Tishchenko et al.* (2005) for pure methane at varying salinities, but has the added flexibility of adjusting the gas ratio (*CSMHYD*, 2018). Pure methane hydrate formed with seawater produces the smallest gas hydrate stability zone and mixed gas hydrate formed in fresh water produces the largest gas hydrate stability zone.

The geothermal gradient below the permafrost layer measured in onshore boreholes in Prudhoe Bay is fairly consistent at 28.2 $\pm$ 1.5°C/ km (*Lachenbruch et al.*, 1982). Beneath the pressure-temperature hydrate phase curves, the geothermal gradient is plotted in green with the base of IBPF identified at 490 m depth, a depth representative of thick

permafrost from our CSEM results. Estimates of the gas hydrate stability zone beneath permafrost onshore have assumed a linear gradient through the permafrost layer from surface temperatures (about -10 °C) to 0 °C (e.g., *Collett et al.*, 2011). This is not appropriate for the offshore environment because ocean temperatures are much warmer and because after permafrost has been submerged for over one thousand years the entire section reaches its melting temperature before starting to thaw from the bottom up (*Lachenbruch et al.*, 1982). We therefore take the temperature through the permafrost layer to be 0 °C with the base of IBPF determining the depth at which temperature starts to increase.

Now that we have used our method to produce maps of permafrost base and thickness, it is a natural extension to produce a map of the corresponding gas hydrate stability zone. For the purposes of generating one map we make a few assumptions: we assume a pure methane composition, a brackish water salinity of 5 ppt, a geothermal gradient of 28.2°C/km (*Lachenbruch et al.*, 1982), and a hydrostatic pressure gradient of 9.795 kPa/m (*Holder et al.*, 1987; *Collett et al.*, 2011). Based on well logs in the area, the pore water is likely brackish because resistivities below the IBPF layer drop back to a few Ωm, more consistent with brackish water than fresh water. We assume a pure methane composition to make this a conservative estimate of current gas hydrate stability zone, but we estimate that gas composition could increase our estimate of depth to edge of gas hydrate stability zone by a few hundred meters. Changes to the geothermal gradient outside the Prudhoe Bay area will also affect our estimates, thus our map is most relevant directly offshore Prudhoe Bay.

Finding the intersection of the geothermal gradient and the gas hydrate phase curve

yields the base of the gas hydrate stability zone. We obtain a depth to base of the gas hydrate stability zone at each location where we have depth to base of IBPF using EM soundings to produce the map in Figure 6.6. Our gas hydrate stability depths range from roughly 500 m to 1,200 m, which is consistent with previous predictions (*Collett et al.*, 2011) in the area. However, the map we produce here is an improvement because it is based on a denser sampling of permafrost thickness, though it is still subject to errors due to assumptions of gas composition and geothermal gradients. Our map of the base of gas hydrate stability zone should be most accurate directly offshore Prudhoe Bay because we used the geothermal gradient measured for this area. As distance from Prudhoe Bay increases (especially towards Harrison Bay) the geothermal gradient may change, changing the gas hydrate stability zone.

6.2 Comparison to offshore borehole data

The majority of exploration on the North Slope, and corresponding study of permafrost, has been done onshore. *Ruppel et al.* (2016) gathered data from existing boreholes offshore, most of which are located on either natural barrier islands or small man-made islands, to accommodate interest in relict subsea permafrost. Data from these boreholes were plotted alongside EM model results in the previous section (Figs. 6.1 to 6.3). Individual boreholes are shown here in detail and compared to vertical profiles from EM inversions.

The boreholes analyzed by *Ruppel et al.* (2016) employ a variety of techniques to determine resistivity. All are deep resistivity or conductivity logs whose signals penetrate far enough from the borehole to be unaffected by drilling effects. The majority of well logs presented here use deep dual induction logs (ILD), an induction logging tool that measures horizontal conductivity. Other conductivity logs are deep phasor induction (IDP) and deep enhanced phasor induction (IDER). All induction well logs measure conductivity and therefore saturate above 1000 Ωm because these conductivity values are approaching zero (.001 S/m). Logs that measure resistivity instead of conductivity include deep-penetration laterologs (LLD), induction resistivity (RILD), and deep-penetration shielded electromagnetic wave resistivity (SEDP, EWDP), a measure-while-drilling approach that uses EM wave propagation to measure resistivity.

The technique used to measure resistivity can influence the final value, and therefore not all well logs are directly comparable. Four boreholes are shown in Figures 6.7 to 6.10,

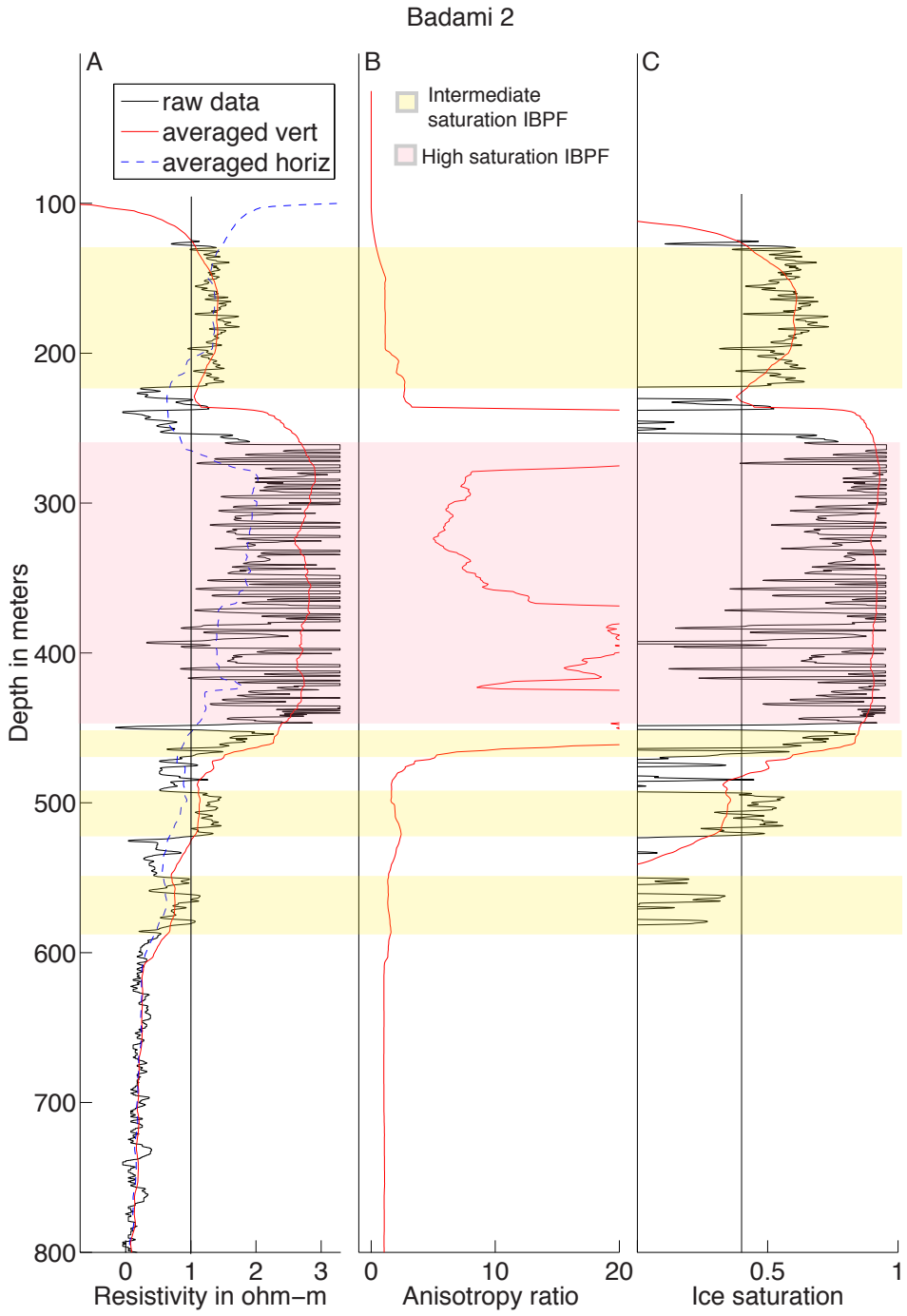

Figure 6.7: A. Resistivity from Badami 2. Black is raw borehole resistivity data, red is vertical resistivity smoothed on a 50 m scale, dashed blue is horizontal resistivity averaged on a 50 m scale. B. Anisotropy on 50 m scale. C. Ice saturation for raw and averaged resistivity values. Ice saturation zones from (*Ruppel et al.*, 2016).

and their locations are labelled in Figure 6.1. All four are induction logs and should be comparable to each other. Badami 2 is an IDER log while Beechey Point, West Mikkelsen 2 and Thetis Island are all ILD logs.

The Badami 2 well is located near Tigvariak Island, by the eastern edge of our CSEM survey, and is just shoreward of West Mikkelsen 2, which is on Tigvariak Island. The group of boreholes in this area contain the thickest and most resistive (>1000 Ωm) high saturation permafrost sections, which generally corresponds to the region of thickest and highest resistivities produced by our EM inversions. The Beechey point well is located near Tow 3 offshore the Sagavanirktok River outflow and indicates two layers of intermediate saturation permafrost. Thetis Island is located near the entrance to Harrison Bay and indicates a deeper, thinner layer of high saturation permafrost.

Well logs make measurements on a much finer scale than the diffusive EM method is able to resolve. We can attempt to imitate what diffusive EM methods would see based on well logs by averaging over a window representative of CSEM method resolution. The smoothing window used in Figures 6.7 to 6.10 is 50 m, which is on the small side, especially at depth, because our EM inversions would not resolve a 50 m layer. The 50 m window, however, does a good job of demonstrating the effects of smoothing while still capturing the major features in the well log.

For the vertical direction, in each moving window of thickness T, the average vertical resistivity can be found by adding the impedances in series. In the horizontal direction, average horizontal resistivity can be found by adding the admittance of all the layers in parallel. These averaged values of horizontal and vertical resistivity are plotted on top

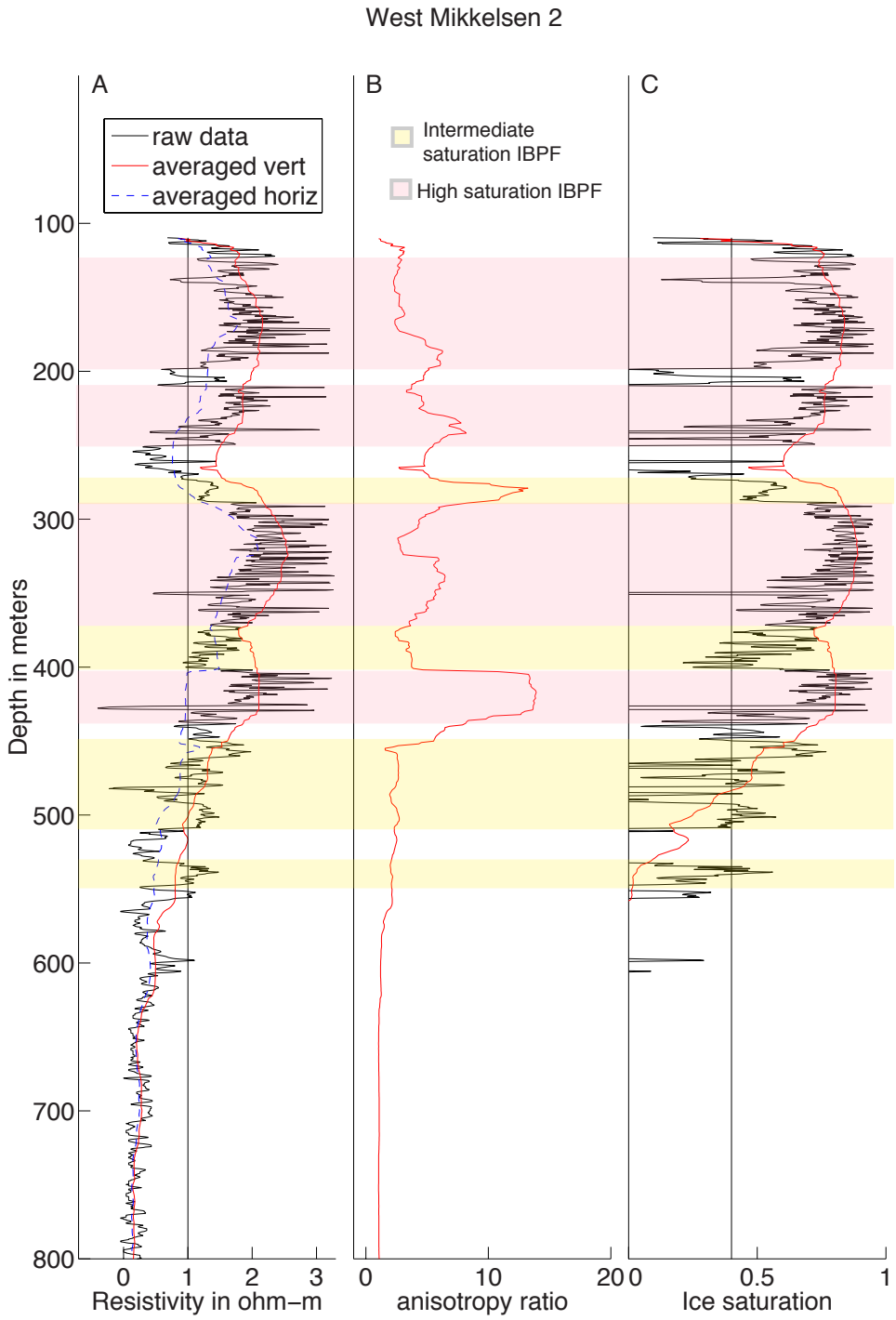

Figure 6.8: A. Resistivity from West Mikkelsen 2, on Tigvariak Island. Black is raw borehole resistivity data, red is vertical resistivity smoothed on a 50 m scale, dashed blue is horizontal resistivity averaged on a 50 m scale. B. Anisotropy on 50 m scale. C. Ice saturation for raw and averaged resistivity values. Ice saturation zones from (*Ruppel et al.*, 2016).

of raw borehole data in panel A of Figures 6.7 to 6.10. Anisotropy is then found as the vertical resistivity divided by horizontal resistivity, plotted in panel B of Figures 6.7 to 6.10. Mathematically speaking vertical and horizontal resistivity (ρ_v and ρ_h) are calculated as follows:

$$\rho_v = \frac{1}{T}\sum_{i=1}^{N} \rho_i t_i$$

and

$$\frac{1}{\rho_h} = \sigma_h = \frac{1}{T}\sum_{i=1}^{N} \sigma_i t_i,$$

where t is the thickness of each layer, T is the thickness of the smoothing window, and N is the number of layers in the moving window, ρ_i is the resistivity of each layer, and $\sigma_i = 1/\rho_i$ is the conductivity of each layer.

Resistivity values can be used to calculate the ice saturation present in the sediment column. Following the method used in the *Ruppel et al.* (2016) paper,

$$S = 1 - (\frac{aR_w}{\phi^k R_0})^{1/n} \tag{6.1}$$

where ϕ is taken to be an empirical function of depth given by *Lee* (2005) as $\phi = 0.532e^{-z/1963}$, S is the ice saturation, z is in meters, R_0 is the measured resistivity, k is the cementation factor and assumed to be 2, aR_w is a constant multiplied by the apparent resistivity of water saturated sediments and is 1 Ωm as in *Lee* (2005), and n is another empirical constant taken from *Pearson et al.* (1982) to be 1.983. We use this relationship to calculate ice saturation for four borehole logs, shown in panel C of Figures 6.7 to 6.10.

Beechey Point is less than 1 km away from the center of Tow 3, Badami 2 is nearest the intersection of Tow 15 and Tow 16, West Mikkelsen 2 borehole is near Tow 14, and

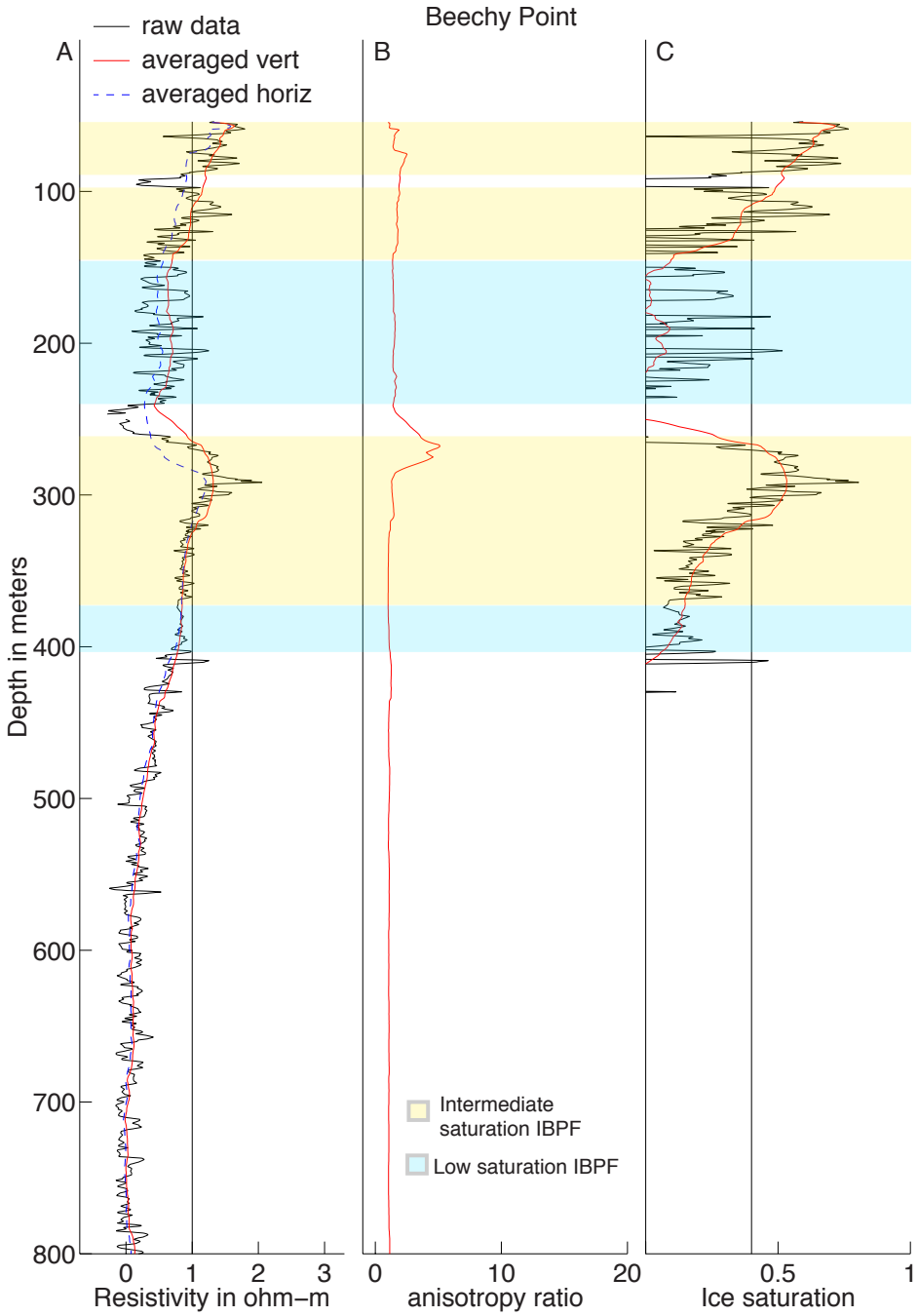

Figure 6.9: A. Resistivity from Beechey Point. Black is raw borehole resistivity data, red is vertical resistivity smoothed on a 50 m scale, dashed blue is horizontal resistivity averaged on a 50 m scale. B. Anisotropy on 50 m scale. C. Ice saturation for raw and averaged resistivity values. Ice saturation zones from (*Ruppel et al.*, 2016).

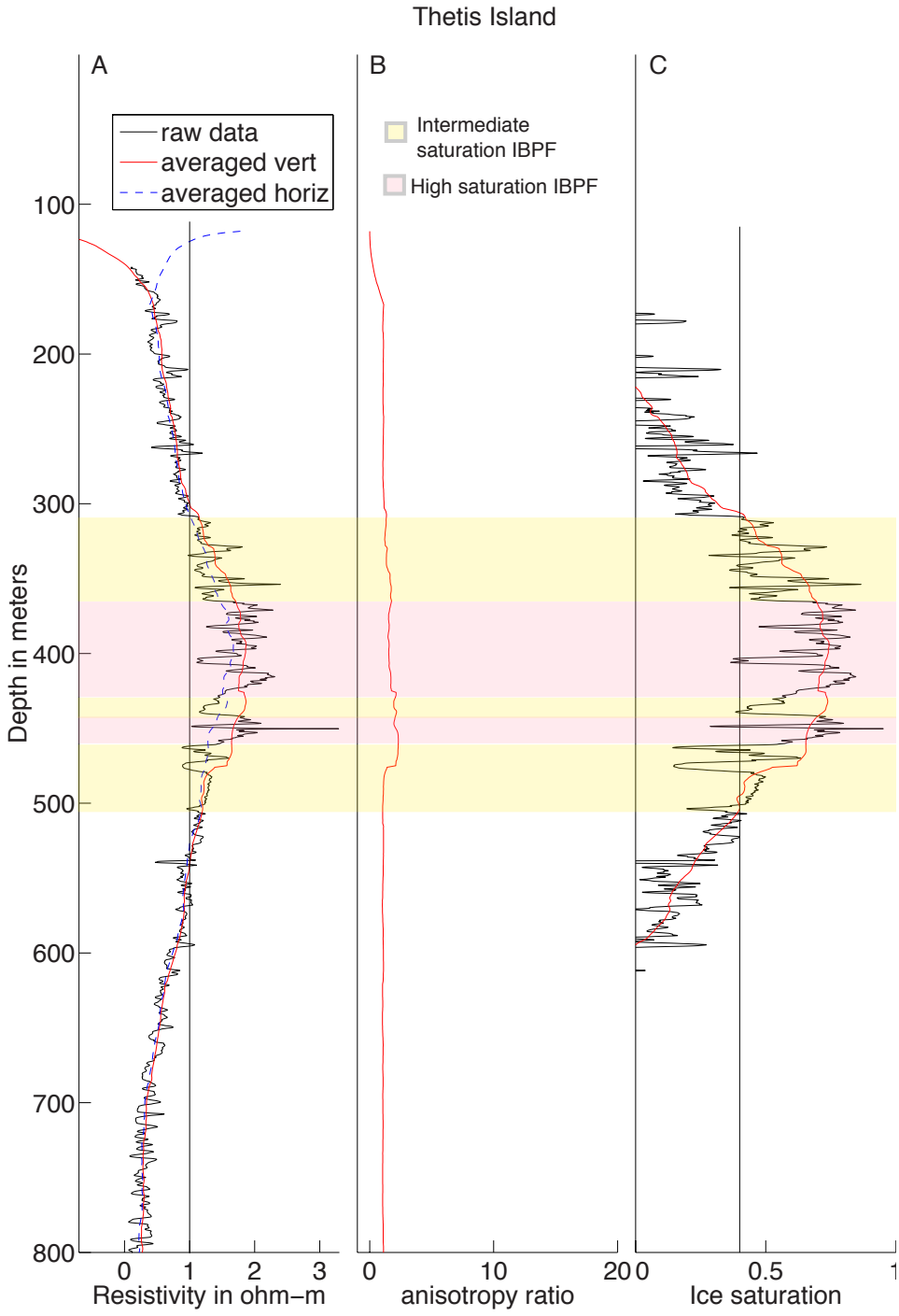

Figure 6.10: A. Resistivity from Thetis Island, near Harrison Bay. Black is raw borehole resistivity data, red is vertical resistivity smoothed on a 50 m scale, dashed blue is horizontal resistivity averaged on a 50 m scale. B. Anisotropy on 50 m scale. C. Ice saturation for raw and averaged resistivity values. Ice saturation zones from (*Ruppel et al.*, 2016).

Thetis Island is at the entrance to Harrison Bay, closest to Tow 5. Vertical profiles were taken from the 2D inversions closest to well logs and plotted on top of the well log resistivity in Figure 6.11. With the exception of Beechey Point, all other well logs are several to tens of kilometers away from the EM tow lines, making it unlikely that there will be an exact match between EM vertical profiles and the well logs. However, this is still a valuable exercise to see general differences between well logs and EM results.

In Beechey Point, Badami 2, and West Mikkelsen 2 there is a layer of unfrozen sediment between two layers of permafrost at about 250 m depth. Similar two-layer behavior in the Sagavanirktok River Delta was noted in *Osterkamp and Payne* (1981). The Tow 3 EM vertical profile reaches a similar peak resistivity as the Beechey Point borehole, but averages over the two layers and creates just one high resistive layer. The Occam inversion searches for the simplest model that fits the data, in this case the simplest model is a three layer model with anisotropy, which is why our EM inversion results do not capture the layered behavior seen in the well logs. The joint seafloor and Porpoise inversion of Tow 4 tried to re-create a two layered system, but the regulatory action resulted in a smooth model.

Though the vertical EM profiles do not replicate the vertical detail provided by well logs, by using the 10 Ωm contour to define the top of permafrost and mid point between peak and minimum anisotropies beneath the permafrost layer to define the base of permafrost, as was done for Figures 6.1 and 6.3, we are still able to get reasonable values for the thickness of the permafrost layer. This is because we understand the regularization in our inversion and have made smart choices when defining the base of permafrost even

though we have not resolved the underlying unfrozen sediment due to limited source-receiver offsets.

From section 5.3, we saw that given an anisotropic layer of permafrost with a vertical resistivity of 100 Ωm and horizontal resistivity of 5 Ωm our Porpoise system was only sensitive down to 300 m. Increasing the resistivity of the section increased the depth of sensitivity to a maximum of 600 m. For the thickest and most resistive permafrost sections the 600 m maximum depth of sensitivity is near the IBPF base, and for thinner less resistive permafrost layers the Porpoise maximum sensitivity and base would both be shallower. This means that it is unlikely that we are sensitive to the underlying unfrozen sediments and that the decay from high resistivity values within the permafrost section is due to inversion regularization and is not driven by data. As a result the EM vertical profiles tend to maintain higher resistivity values beyond the base of permafrost seen in the well logs, and do a better job of matching the top of the permafrost layer. Maps of permafrost extent (Figures 6.1 to 6.4) agree with borehole values because our definition of the IBPF base was chosen to be a best guess based on our inversion regularization while knowing our data is incapable of resolving the base due to limited source-receiver offsets.

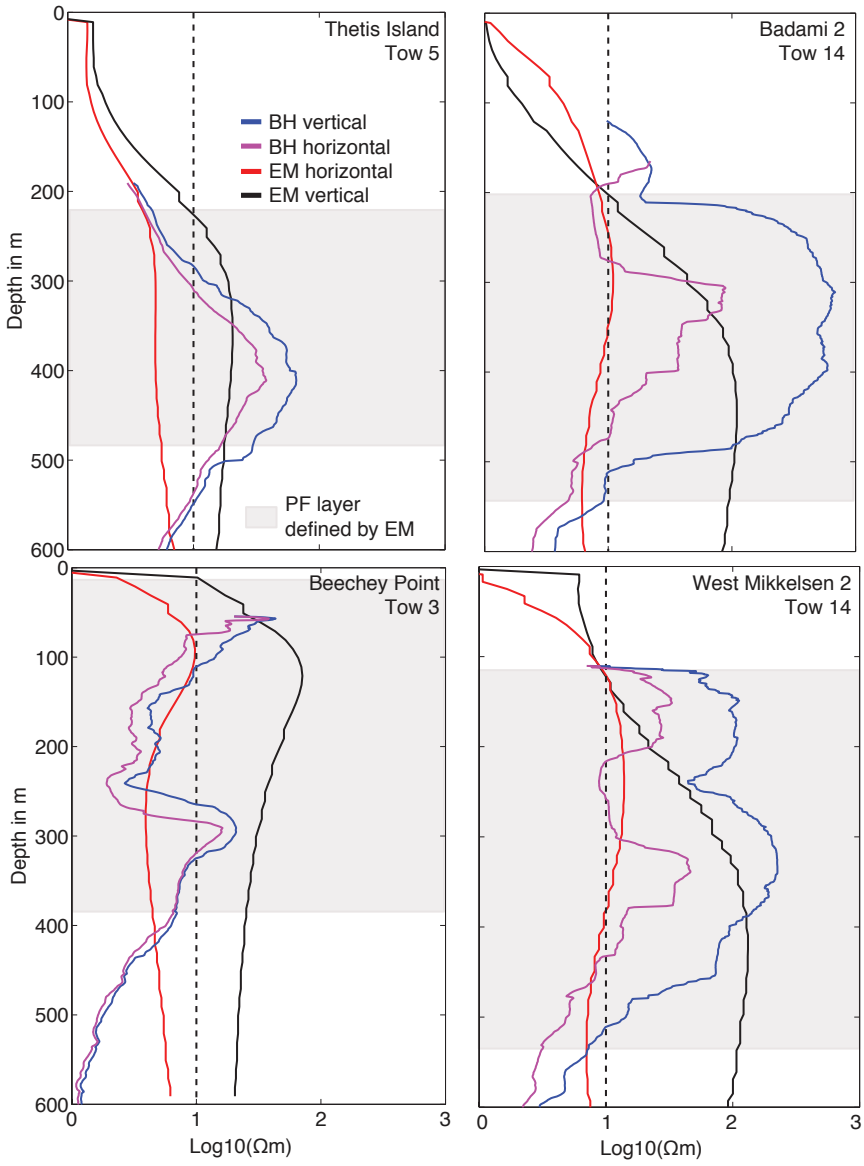

Figure 6.11: Vertical profiles from EM inversions plotted on top of smoothed resistivity measurements from nearby well logs. The permafrost (PF) layer according to the EM profiles are highlighted in beige boxes, according to the definition of top and base of permafrost described in section 5.1.

6.3 Thermal stability and longevity of subsea permafrost

The history of sea level transgressions influences the current distribution of permafrost. During sea level low stands sediment temperatures decrease and eventually form permafrost. The frozen ground warms and thaws while submerged during sea level high stands. Though permafrost is defined as ground that has been below 0°C for over two years, it takes thousands of years to form permafrost hundreds of meters thick (*Osterkamp*, 2001; *Mackay*, 1972). Using a simple conduction model, the depth to bottom of permafrost (X) at time t is given by

$$X(t) = \sqrt{\frac{2K(T_e - T_g)t}{h}}, \tag{6.2}$$

where K is the thermal conductivity of ice-bonded permafrost, T_e is temperature at the base of permafrost, T_g is the average ground temperature, and h is the volumetric latent heat (*Osterkamp*, 2001).

Thermal parameters for frozen ground, K and h, are given in *Harrison and Osterkamp* (1978) as $K = 6.1\text{x}10^7$ $\text{Jm}^{-1}\text{yr}^{-1}\text{deg}^{-1}$ and $h = 12.0\text{x}10^7$ Jm^{-3} for Prudhoe Bay. Assuming these values, it takes 20,000 years for permafrost to reach over 600 m depth. Given that the most recent sea level low stand lasted closer to 5,000 years (*Clark et al.*, 2009), the maximum thickness of permafrost formed during that time, permafrost near the current 100 m isobath, should be less than 300 m thick. Permafrost therefore thins seaward not only because it has been submerged longer and therefore degraded more, but also because permafrost formed further offshore would have been thinner upon submergence.

There are two main mechanisms by which subsea permafrost is degraded: top-down and bottom-up thawing (e.g., *Osterkamp*, 2001; *Lachenbruch et al.*, 1982). Submerged permafrost thaws from the top-down due to a combination of conduction and salt-water intrusion and from the bottom-up due to heating from the geothermal gradient. The top-down thawing mechanism is dependent on many factors and incompletely understood (*Lachenbruch et al.*, 1982). The topic is explored in a paper by *Harrison and Osterkamp* (1978), who concluded that salt transport is dominated by convection (the movement of interstitial water due to density contrasts) while heat transport remains diffusive (conduction) driven. High seabed temperatures lead to much faster thawing due almost exclusively to conduction, while thawing when seabed temperatures are near freezing temperature of the permafrost is much slower and due almost exclusively to salt intrusion by density driven convection (*Harrison and Osterkamp*, 1978).

Lachenbruch et al. (1982) did a thorough theoretical analysis of bottom-up thawing for the Prudhoe Bay area, which we summarize here. Permafrost degradation due to bottom-up thawing can be thought of as occurring in two stages. In the first stage temperature is conducted from the surface down to the base of permafrost until the entire permafrost layer is near its freezing point. Depleting this cold reservoir takes time and depends on the thickness of the layer, its temperature, and the average seabed temperature. It is during the second phase that the warm permafrost thaws from the bottom up due to heat from the geothermal gradient.

Next we present the analytical solution of *Lachenbruch et al.* (1982) to the first stage of permafrost degradation and estimate the time it takes to deplete the cold reservoir in

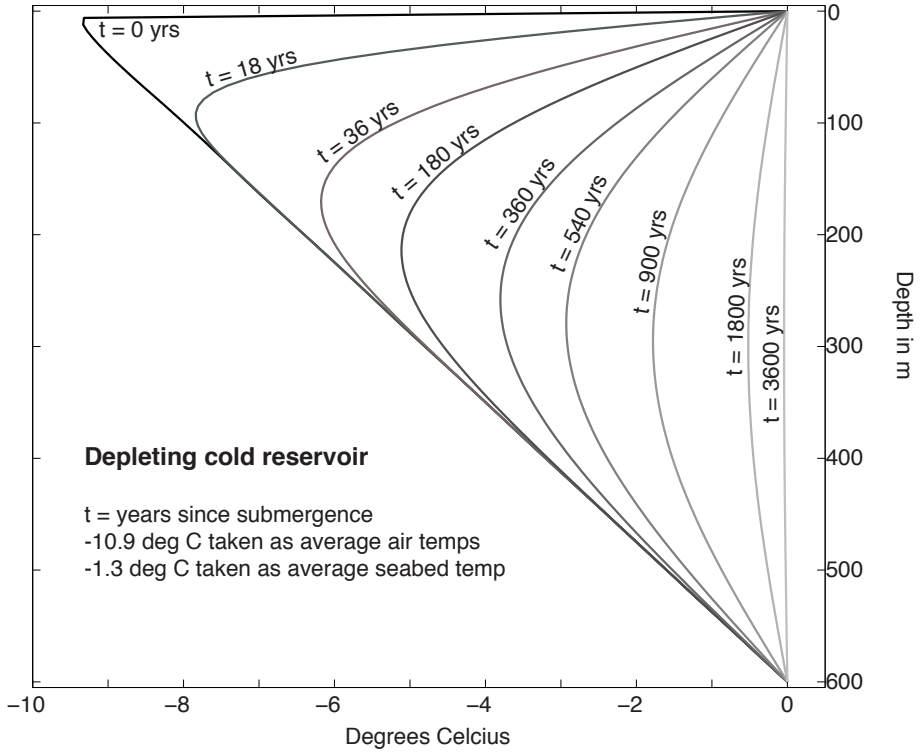

Figure 6.12: Depletion of cold reservoir of a 600 m thick permafrost layer initially exposed to sub-aerial temperatures of -10.9°C, then instantaneously submerged by ocean water at -1.3°C. For this layer thickness the characteristic time is $\lambda = 1,800$ years. After the initial 1,800 years have passed, nearly the entire permafrost layer has reached near-melting temperatures and the permafrost base will proceed to rise. This plot is an analytical solution to temperature degradation (depletion of the cold reservoir) prior to bottom-up thawing based on equations and parameters presented by (*Lachenbruch et al.*, 1982).

Prudhoe Bay. The entire formulation of this analytical solution is found in *Lachenbruch et al.* (1982). This model uses a few important assumptions: it is assumed that water depth is greater than 2 m and that no sea ice freezes to seabed, submergence and the corresponding increase in temperature is assumed to be instantaneous, and subsurface temperature and lithology offshore is assumed to be the same as onshore today. In water shallower than 2 m ice freezes to the seabed and couples to the atmosphere during winter months, preserving underlying permafrost longer. Submergence from 0 m to 2 m water depth can

take hundreds to thousands of years, depending on seabed slope and transgression rate. The last assumption is probably reasonable near shore where the shelf was exposed to air temperatures long enough to develop the same thickness of permafrost as currently on land (>20,000 years).

The following parameters are used by *Lachenbruch et al.* (1982) while formulating the analytical solution:

$\theta_0 = -10.9°C$, average Arctic air temperature

$\theta_b = -1°C$, temperature at the base of permafrost, also its freezing point

$\theta_s = -1.3°C$, seabed temperature

$Z(0) = 600$ m, base of ice-bearing permafrost at time of inundation

$\theta_1(z,t) =$ temperature profile through permafrost layer

Temperature distribution as the permafrost warms to a uniform temperature will be the solution to the diffusion equation:

$$\frac{\partial \theta_1}{\partial t} = \alpha \frac{\partial^2 \theta_1}{\partial z^2}, \qquad 0 \leq z \leq Z, \tag{6.3}$$

where α is thermal diffusivity and was calculated to be ≈ 0.016 cm^2/s for frozen sediments in Prudhoe Bay by *Lachenbruch et al.* (1982). Thermal diffusivity is a function of thermal conductivity (K), specific heat (c), and density (ρ) such that $\alpha = K/\rho c$, these parameters were determined for the Prudhoe Bay area with borehole temperatures and drill cuttings by *Lachenbruch et al.* (1982). Equation 6.3 is subject to two boundary conditions and an

initial condition:

$$\theta_1(z,0) = (\theta_0 - \theta_s)\left(1 - \frac{z}{Z}\right), \quad t = 0$$

$$\theta_1(z,t) = 0, \quad z = 0 \text{ and } Z, \quad t > 0.$$

The solution to the problem posed above is given in equation 6.4, where λ is the characteristic time constant, $\lambda = Z^2/4\alpha$ or about how long it takes to warm the entire permafrost layer to near freezing:

$$\theta_1(z,t) = (\theta_0 - \theta_s)\frac{2}{\pi}\sum_{n=1}^{\infty}\frac{1}{n}\exp\left(\frac{-n^2\pi^2}{4}\frac{t}{\lambda}\right)\sin\left(n\pi\frac{z}{Z}\right). \tag{6.4}$$

Figure 6.12 plots the solution to equation 6.4 for a 600 m thick layer of permafrost in Prudhoe Bay with a time constant of $\lambda = 1,800$ years. For a 300 m thick layer in Prudhoe Bay, similar to what we expect, that was submerged near the current 100 m isobath, λ is only 450 years.

To determine the rise rate of the base of permafrost after the λ years it takes to reach melting temperature, they assume a quasi-steady state with a constant geothermal heat flux (q) across the base at $Z(t)$. If L is the latent heat required for melting and ϕ is porosity, then the heat balance at the base of the warm permafrost given by:

$$-L\phi\frac{\mathrm{d}Z}{\mathrm{d}t} = q - K_{fr}\frac{\mathrm{d}\theta}{\mathrm{d}z}. \tag{6.5}$$

After λ years equation 6.5 simplifies to

$$-\frac{dZ}{dt} = \frac{q}{L\phi}.$$

Appropriate values for Prudhoe Bay are $q = 41$ cal/cm^2 yr, ϕ=0.385, and $L = 73$ cal/cm^3 which gives a rise rate of 1.5 cm/yr that is independent of permafrost layer thickness (*Lachenbruch et al.*, 1982).

In summary, for the Prudhoe Bay area, a 600 m thick permafrost layer reaches temperatures near freezing over the first 1,800 years after submergence and then the base begins to rise at a constant rate of 15 m every 1,000 years (*Lachenbruch et al.*, 1982). *Lachenbruch et al.* (1982) also determines how much the base rises during the initial phase of depleting the cold storage, for a 600 m layer the base rises about 10 m, for a thinner layer of 300 m the base would rise only 2.5 m.

We can use this basic thermal model to calculate how much permafrost will remain after submergence and how long a given permafrost thickness will persist after submergence, a few of these are shown in Tables 6.1 and 6.2. Table 6.1 gives values for how much permafrost would remain after $5,000$ years, $10,000$ years and $20,000$ years starting from a thickness of 300 m and 600 m. Table 6.2 indicates how long permafrost layers with thickness from 300 m to 700 m would persists after full submergence. Once permafrost thins to about 100 m this model no longer applies because density driven fluid circulation likely dominates and thaws permafrost faster than the conduction used in this model, we account for this by calculating time until less than 100 m thickness is reached for time values in Table 6.2.

Table 6.1: Remaining thickness of permafrost layer after 5, 10, and 20 thousand years from a starting thickness of 300 m (column 2) and 600 m (column 3).

Initial thickness:	300 m	600 m
5,000 years	222 m	515 m
10,000 years	147 m	440 m
20,000 years	–	290 m

Table 6.2: Time we would expect a starting thickness of permafrost to last after submergence given conduction model in (*Lachenbruch et al.*, 1982).

Initial thickness	Time until thawed
300 m	14,000 years
400 m	20,000 years
500 m	27,000 years
600 m	34,000 years
700 m	40,000 years

Based on the combination of Tables 6.1 and 6.2 we would not expect any permafrost to be left near the 100 m isobath, where the shelf was exposed for a relatively short time

compared to how long it has been submerged. Permafrost submerged in the recent past would have been at least 600 m thick, so we expect nearshore subsea permafrost to persist for another 30,000 years or so. To create a graphical representation of this we combine equation 6.2 for formation of permafrost with Lachenbruch's rate of thaw, and assume a steady linear increase in relative sea level rise of 100 m over 20,000 years to obtain a 2D profile of permafrost present upon submergence and expected remaining permafrost today. This 2D profile is plotted in Figure 6.13 with permafrost thickness calculated with equation 6.2 in blue and the remaining permafrost after submergence shown in red.

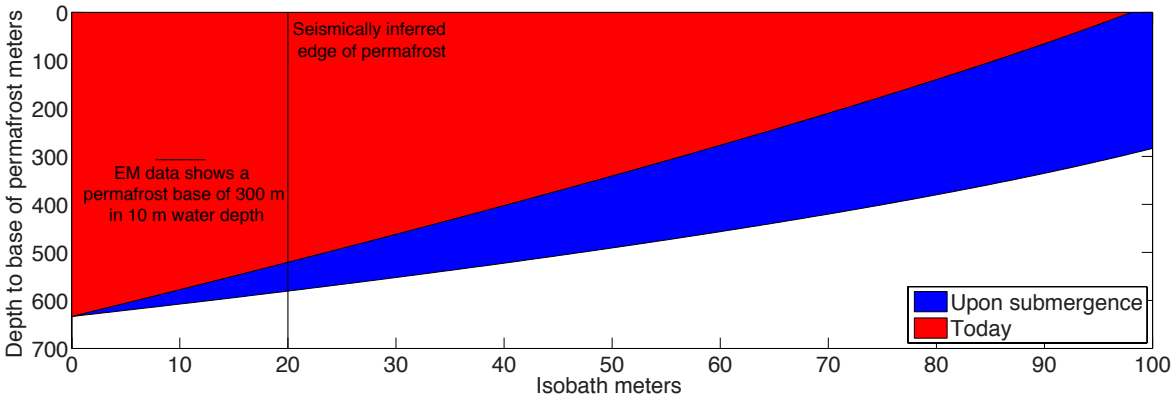

Figure 6.13: Analytical calculation of maximum amount of permafrost initially formed on exposed the shelf and what would remain today assuming a steady sea level increase. Geophysical methods detect significantly less IBPF on the shelf than predicted by this basic thermal model.

Seismic data (both refraction and reflection) detected no IBPF beyond the 20 m isobath (*Brothers et al.*, 2012; *Brothers et al.*, 2016), and though we were unable to collect data beyond the seismically inferred edge of permafrost due to the sea ice pack, the shore perpendicular Tow 2 inversion shows IBPF only 200 m thick (base depth of 300 m) at 10 m water depth, not the over 500 m thickness predicted in Figure 6.13. This simple

analytical calculation produces a significant overestimation of permafrost still present on the Alaskan Beaufort shelf. In contrast, seismic reflection and refraction surveys as well as some limited deep temperature profiles (*Morack et al.*, 1983; *Mackay*, 1972; *Taylor et al.*, 1996) suggest that permafrost exists to nearly the shelf edge in the Southern Beaufort Sea offshore Canada.

There are multiple reasons this simple analytical model is inadequately describing Alaskan permafrost extent (1) the calculation of initial permafrost thickness is overestimating thickness of permafrost formed (2) Lachenbruch's model is too idealized and underestimates speed at which permafrost thaws and/or (3) sea level rise was not in fact steady, instead rising faster earlier and slower in more recent times.

Both points (1) and (2) suggest the simple models are not capturing the mechanisms of permafrost formation and thawing. These idealized equations are calculating the thickness of permafrost based on the temperature definition - not the extent of freezing, the parameter to which geophysical techniques are sensitive. The depth of IBPF formed may be different than the depth of the 0°C isotherm; however, in Prudhoe Bay area these two are often close to coinciding on land (*Collett et al.*, 1989), and the discrepancy is not large enough to account for the 250 m difference in remaining base depth.

Equation 6.2 predicts permafrost thickness of about 600 m after 20,000 years of exposure. Permafrost thickness on land today is over 600 m (well logs have seen up to 660 m (*Collett et al.*, 1989)) in Prudhoe Bay, which is inline with 20,000 years of exposure, but the land above sea level has been exposed for longer than this because the last ice-age peaked 20,000 years ago. Therefore, the initial thickness of permafrost is likely

overestimated.

In addition to an overstated initial thickness, the conduction-only thaw model could be underestimating the speed at which submerged permafrost thaws if convection from the top-down is more influential than previously thought. The conduction-only model is based on the reasonable assumption that ice-bonded permafrost is impermeable, restricting heat transfer to conduction except in the top thawed layer. Warmer permafrost that has ceased to be ice-bonded may allow for easier convection, but this would still be limited to the top thawed layer and we do not see dramatic increases in depth to top of IBPF in our data. Inaccuracies in the conduction-only heat transfer model are therefore unlikely to account for the discrepancy between idealized model and data. There has been an argument made that saline water actually impedes the cold water depletion described by *Lachenbruch et al.* (1982) and preserves colder temperatures throughout the permafrost layer (*Nixon*, 1986). This thermal analysis was used to explain deep temperatures measurements made offshore Canada, but would only serve to exacerbate the discrepancy seen here offshore Alaska.

For the purposes of making Figure 6.13, a steady sea level rise was assumed. This is not a reasonable assumption, it is more likely that sea level rose at an unsteady rate that included multiple transgressions. *Hill et al.* (1985) attempted to reconstruct a history of sea-level rise for the Canadian Arctic, and their model has sea level rising rapidly to the 40 m isobath (reaching 40 m at 15k years ago), then falling to the 70 m isobath (between 15k and 12k years ago), and finally rising at a slower rate to the present day (70 m rise in 12k years). An initial rapid rise in sea level followed by a slower rise rate is consistent with the shallower IBPF base we have detected with geophysical methods. If we seek to

explain the data with two distinct rates of sea level rise then a rise of 80 m in the first 9,000 years followed by a 20 m rise in the ensuing 11,000 years would be consistent with the thickness of IBPF seen by our CSEM data. However, the combination of these two rise rates predicts permafrost out to the 90 m isobath and is therefore still an overestimation far out on the shelf.

Maps were made of depth to top of IBPF, its thickness, and peak resistivity based on data abstracted from CSEM inversions. Though our CSEM inversions tended to smear the base of IBPF to greater depths, we took this into account when defining the depth to base of IBPF and were still able to produce maps in agreement with offshore boreholes, but did not produce vertical CSEM profiles capable of quality well ties. Our CSEM soundings support the prior geophysical surveys that infer the current extent of IBPF is less than that expected from thermal considerations. Sea ice, however, prevented us from collecting data far enough offshore to quantifying the extent of IBPF on the shelf.

Portions of the text in Chapters 5 and 6, are being prepared for publication. The dissertation author is the first author of the work preparation; the coauthor on the publication is Steven Constable who supervised the research.

Bibliography

Brothers, L. L., P. E. Hart, and C. D. Ruppel (2012), Minimum distribution of subsea ice-bearing permafrost on the U.S. Beaufort Sea continental shelf, *Geophys. Res. Lett.*, *39*, L15501.

Brothers, L.L., B.M. Herman, P.E. Hart, and C.D. Ruppel, (2016), Subsea ice-bearing permafrost on the U.S. Beaufort Margin: 1. Minimum seaward extent defined from multichannel seismic reflection data, *Geochem. Geophys. Geosyst.*, *17* 4354-4365

Clark, P.U., A.S. Dyke, J.D. Shakun, A.E. Carlson, J. Clark, B. Wohlfarth, J.X. Mitrovica, S.W. Hostetler, and A.M. McCabe. (2009) The last glacial maximum. *Science*. *325* 710-714

Collet, T. S., L.W. Myung, W. F. Agena, J. J. Miller, M. V. Lewis, R. Boswell, T. L. Inks (2011) Permafrost-associated natural gas hydrate occurrences on the Alaskan North Slope, *Mar. Pet. Geol.*, *28*, 279-294

Collett, T.S., K.J. Bird, K.A. Kvenvolden, and L.B. Magoon (1989), Map showing the depth to the base of the deepest ice-bearing permafrost as determined from well logs, North Slope, Alaska: USGS Oil and Gas Investigations Map 222.

Center for Hydrate Research, Colorado School of Mines. (2018)CSMHYD code, available at: http://hydrates.mines.edu/CHR/Software.html. Accessed February 20, 2018.

Frederick, J. M., and B. A. Buffett (2015), Effects of submarine groundwater discharge on the present-day extent of relict submarine permafrost and gas hydrate stability on the Beaufort Sea continental shelf. *J. Geophys. Res. Earth Surf.*, *120*, 417432

Frederick, J. M., and B. A. Buffett (2014), Taliks in relict submarine permafrost and methane hydrate deposits: Pathways for gas escape under present and future conditions, *J. Geophys. Res. Earth Surf.*, *119*, 106 -122

Harrison, W.D., T.E. Osterkamp, (1978) Heat and mass transport processes in subsea permafrost 1. An analysis of molecular diffusion and its consequences. *J. Geophys. Res.*. *83*(C9) 4707-4712

Hill, P.R., P.J. Mudie, K. Moran and S.M. Blasco (1985) A sea-level curve for the Canadian Beaufort Shelf, *Can. J. Earth Sci.*, *22*(1) 1383-1393

Holder, G.D., R.D. Malone, and W.F. Lawson (1987) Effects of gas composition and geothermal properties on the thickness and depth of natural-gas-hydrate zones. *J. Petrol. Tech. 39*(9) p. 1147-1152

King, M.S., R.W. Zimmerman, R.F. Corwin (1988) Seismic and electrical properties of unconsolidated permafrost, *Geophys. Prospec.*, *36*, 349-364

Lachenbruch, A.H., J. H. Sass, B.V. Marshall, and T.H. Moses, Jr. (1982) Permafrost, heat flow, and the geothermal regime at Prudhoe Bay, Alaska. *J. Geophys. Res.*, *87* (B11) 9301-9316

Lee, M.W. (2005) Well log analysis to assist the interpretation of 3-D seismic data at the Milne Point, North Slope of Alaska. *U.S. Geol. Surv. Sci. Invest. Rep.*, 2005-5048, 18 pp.

Mackay, J.R., (1972) Offshore permafrost and ground ice, Southern Beaufort Sea, Canada *Can. J. Earth Sci. 9* p. 1550-1560

Morack, J.L., H.A. MacAulay, and J.A. Hunter. (1983) Geophysical measurements of subbottom permafrost in the Canadian Beaufort Sea. *In* Proceedings, Permafrost, Fourth International Conference, National Academy Press, Washington, D.C., pp. 866-871

Nixon, J.F. (Derick). (1986) Thermal simulation of subsea saline permafrost. *Can. J. Earth Sci. 23* p. 2039-2046

Osterkamp, T. E., (2001) Sub-sea permafrost in Encyclopedia of Ocean Sciences (Second Edition), pp 559-569, Academic Press.

Osterkamp, T. E., and M.W. Payne. (1981) Estimates of permafrost thickness from well logs in northern Alaska. *Cold Reg. Sci. Technol.*, textit5, 13-27

Pearson, C.F., P.M. Halleck, P.L. McGuire, R. Hermes, and M. Mathews (1983) Natural gas hydrate deposits: A reveiw of in-situ properties. *J. Phys. Chem.*, *87*, 4180-4185

Pohlman, J., C. Ruppel, C. Maue, L. Brothers, J.Kessler, and C. Worey. (2012). Real-time mapping of seawater and atmospheric methane concentrations offshore of Alaska's North Slope. *USGS Sound Waves*, 140, 4-5

Ruppel, C.D., B.H. Herman, L.L. Brothers, and P.E. Hart (2016) Subsea ice-bearing permafrost on the U.S. Beaufort Margin: 2. Borehole constraints, *Geochem. Geophy. Geosy.*, *17*, 4333-4353. doi:10.1002/2016GC006582.

Taylor, A.E., S.R. Dallimore, and S.I. Outcalt. (1996) Late quarternary history of the Mackenzie-Beaufort region, Arctic Canada, from modeling of permafrost temperatures. 1. The onshore-offshore transition. *Can. J. Earth Sci. 33* p. 52-61

Tishchenko, P., C. Hensen, K. Wallmann, and C.S. Wong (2005) Calculation of the stability and solubility of methane hydrate in seawater. *Chem. Geol. 219* p. 37-52

Chapter 7

Conclusions and future work

We have developed a surface-towed EM system capable of operating in shallow waters on the Arctic shelf. With a 1,000 m array we were able to resolve the top few hundred meters (down to a maximum of 600 m) of the seafloor, including the top transition from marine sediment to relict subsea permafrost. We were also able to obtain reasonable estimates of permafrost thickness across most of our survey area that agreed with borehole data. This makes our Porpoise surface-towed marine CSEM system a cheaper alternative to boreholes and a useful tool that could be used to extensively map subsea relict permafrost offshore Alaska, Canada and Siberia.

There is more work to do to fully understand the extent of permafrost in the Prudhoe Bay area, some of that involves modeling and some requires more ship time. With additional ship time and through collaboration with permafrost modelers, we could address a number of scientific problems that will be mentioned here, some of which arose as a result of our pilot study. We are currently working on securing funding for ship time

that would allow us to answer these questions.

The maximum offshore extent of relict permafrost remains a primary outstanding question. We were prevented from addressing the offshore extent in the pilot study because of dense sea-ice close to shore. Collecting more data later in the season, when sea-ice is likely further offshore, would allow us to capture the seaward edge of permafrost and image unfrozen sediments, which would be helpful in interpretation.

Seismic refraction data confidently identifies extensive amounts of ice-bonded permafrost in Harrison Bay, while CSEM data show only small resistivity anomalies. We suspect this is because layers of ice-bonded permafrost in Harrison Bay are thin and beneath a few hundred meters of unfrozen sediment, which is consistent with well logs (*Ruppel et al.*, 2016) and both seismic and CSEM data sets. Expanding CSEM coverage in Harrison Bay, including longer offset data, would allow for a more complete analysis and comparison between seismic and CSEM data.

Based on modeling (*Frederick and Buffet*, 2015) and our CSEM observations offshore the Sagavanirktok River, increased groundwater flow preserves high ice concentration in shallow regions of permafrost. We could confirm or refute the generality of this observation by collecting data offshore the main confluence of the Colville River for comparison with data collected offshore the Sag River in 2015.

We could collect data in Harrison Bay in the same region that *Pohlman et al.* (2012) measured high concentrations of methane in the water column to see if the increased methane venting is correlated with a talik. The talik would likely be in a paleo river channel of the Colville River, away from the present day main confluence, as suggested by

(*Frederick and Buffet*, 2014) modeling. The talik would be a somewhat linear feature with low resistivity extending perpendicular to shore, as seen in *Shakhova et al.* (2010, 2013).

Barrier islands are present across much of the Arctic coast and are often associated with elevated seismic velocities. The barrier island chain and related topography may play a role in subsea permafrost stability, or vice versa. Most of these islands are moving west and shoreward and will eventually disappear (*Hopkins and Hartz*, 1978). We would like to better understand the atmospheric coupling through this changing topography and its effect on the underlying and surrounding permafrost by collecting data shoreward and seaward of these islands. Indeed, it may be possible to place receivers on the islands themselves to create a continuous model.

The shoreline west of Harrison Bay towards Drew Point has a high rate of coastal erosion, compared to lower rates further east (*Gibbs and Richmond*, 2015). We may expect to see a thick permafrost layer just offshore areas of high coastal erosion and a thinner permafrost layer near slowly eroding coastlines. These variations can be detected by making CSEM measurements along the coast near the shore line in regions of high and low erosion rates. The permafrost layer may give some indication of historical erosion rates and inundation history, and help predict future erosion rates.

Anisotropic inversions from 2015 defined base of permafrost between 300 m and 600 m depth, which is consistent with the expected maximum depth of permafrost. A 600 m base is at the limit of resolution of the 1 km array we used previously. This is deep enough to map permafrost, but capturing the transition to unfrozen sediments beneath the permafrost will be useful for interpreting ice saturations. For this we need to collect

longer offset data, to do so we would adopt two strategies. First, we would expand the Porpoise array to be 1500 m in length, which should be sufficient to guarantee information down to 800 m. To maintain a useable signal to noise ratio at longer offsets we will increase the dipole moment by increasing transmitter and receiver dipole lengths and transmitter power output. Second, we would use seafloor receivers to obtain offsets up to 6 km.

Bruce Buffet and Jennifer Frederick have expressed interest in collaborating to use modeling to help us better integrate our data into current understanding of permafrost dynamics. With a more detailed map of permafrost thickness and ice saturation we should be able to construct a 2D thermal model and make some predications about its longevity given various average ocean temperatures. We will also be able to use Jennifer Frederick's physical models to compute predictions of electrical conductivity and instrument responses. This will provide a way to validate and directly compare model results to our new CSEM measurements.

Bibliography

Frederick, J. M., and B. A. Buffett (2015), Effects of submarine groundwater discharge on the present-day extent of relict submarine permafrost and gas hydrate stability on the Beaufort Sea continental shelf. *J. Geophys. Res. Earth Surf.*, *120*, 417432

Frederick, J. M., and B. A. Buffett (2014), Taliks in relict submarine permafrost and methane hydrate deposits: Pathways for gas escape under present and future conditions, *J. Geophys. Res. Earth Surf.*, *119*, 106 -122

Gibbs, A.E., B.M. Richmond. (2015) National assessment of shoreline change-historicl shoreline change along the north coast of Alasak, A.S.-Canadian border to Icy Cape. *USGS open-file report* 2015-1048

Hopkins, D.M., and R.W. Hartz. (1978) Coastal morphology, coastal erosion, and barrier islands of the Beaufort Sea, Alaska. *USGS Open File Report 78-1063*

Pohlman, J., C. Ruppel, C. Maue, L. Brothers, J.Kessler, and C. Worey. (2012). Real-time mapping of seawater and atmospheric methane concentrations offshore of Alaska's North Slope. *USGS Sound Waves*, 140, 4-5

Ruppel, C.D., B.H. Herman, L.L. Brothers, and P.E. Hart (2016) Subsea ice-bearing permafrost on the U.S. Beaufort Margin: 2. Borehole constraints, *Geochem. Geophy. Geosy.*, *17*, 4333-4353. doi:10.1002/2016GC006582.

Shakhova, N., I. Semiletov, A. Salyuk, V. Yusupov, D. Kosmach, and O. Gustafsson (2010), Extensive methane venting to the atmosphere from sediments of the East Siberian Arctic Shelf, *Science*, *327*, 1246?1250.

Shakova, N., I. Semiletov, I. Leifer, V. Sergienko, A. Salyuk, D. Kosmach, C. Stubbs, D. Nicolsky, V. Tumskoy, and O. Gustafsson. (2013) Ebullition and storm-induced methane release from the East Siberian Arctic Shelf. *Nat. Geosci.*. *7*, 64-70

Appendix A

2015 Inversions

Appendix A includes all inversions from 2015 that were not presented in the text. Inversions 3, 4, and 5-8 can be found in the results chapter. Inversions of tows 1,2, and 9-16 can be found here.

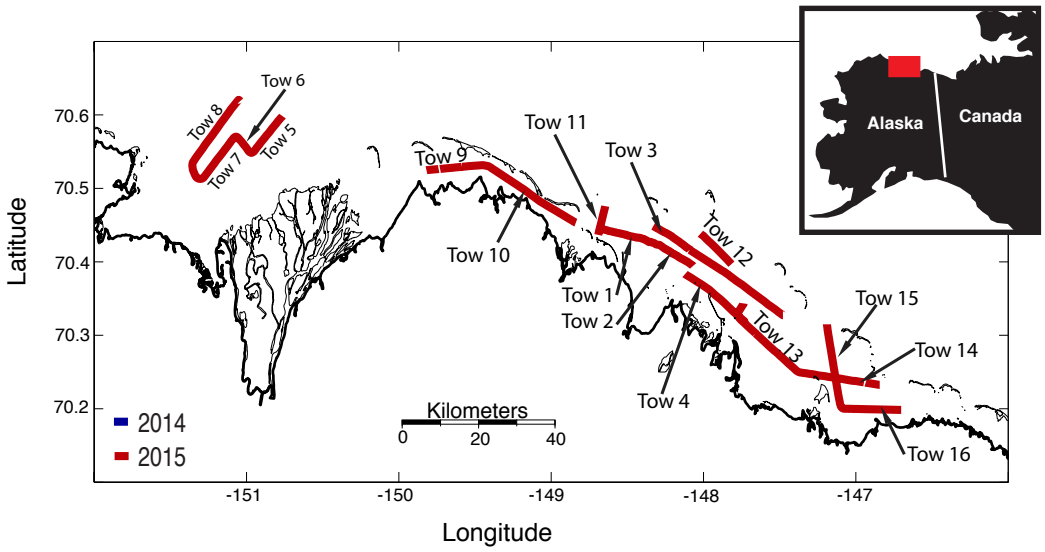

Figure A.1: Location map of tow lines from 2015.

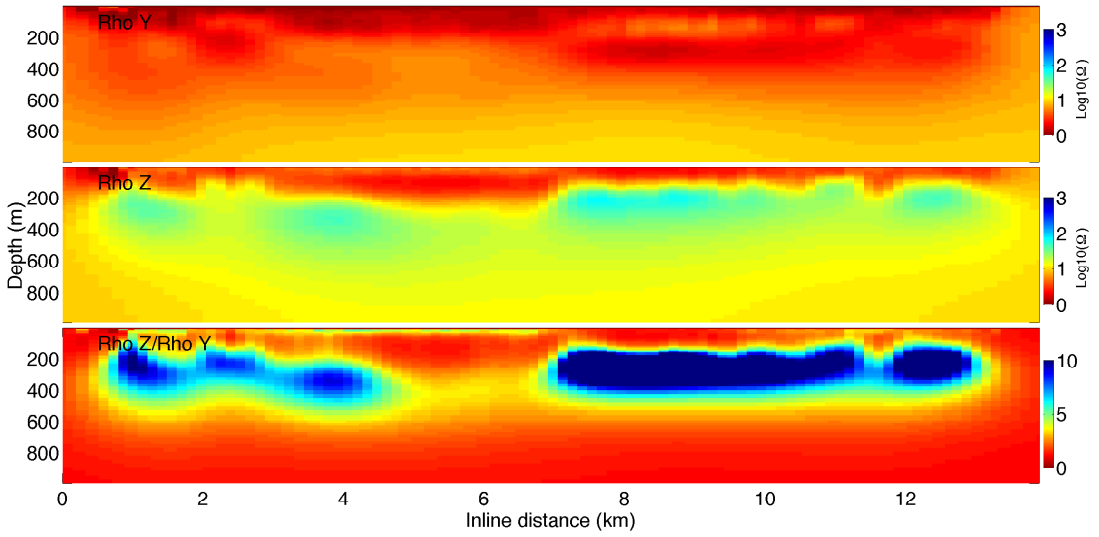

Figure A.2: Anisotropic inversion from Tow 1 2015

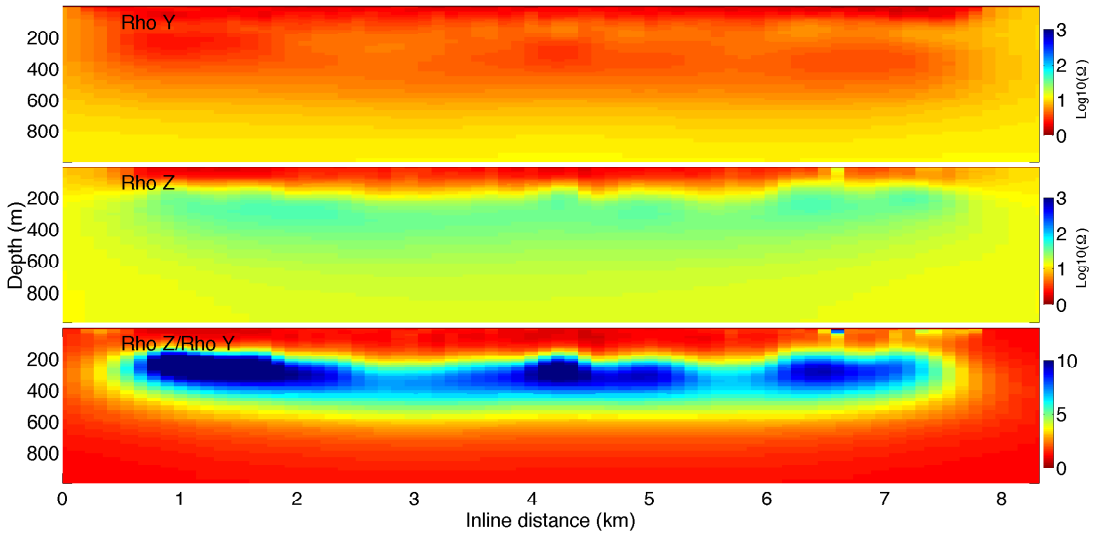

Figure A.3: Anisotropic inversion from Tow 2 2015

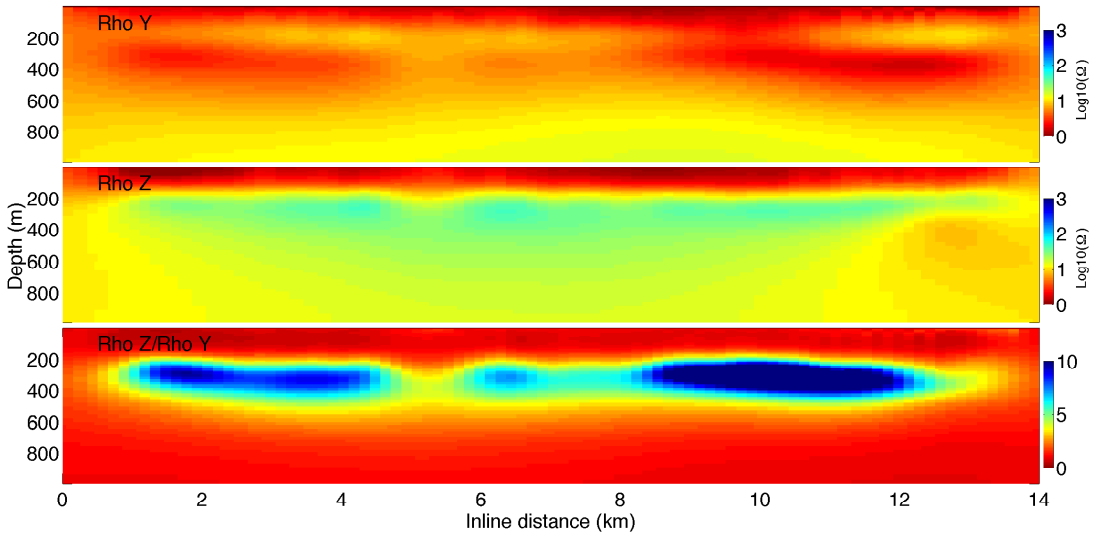

Figure A.4: Anisotropic inversion from Tow 9 2015

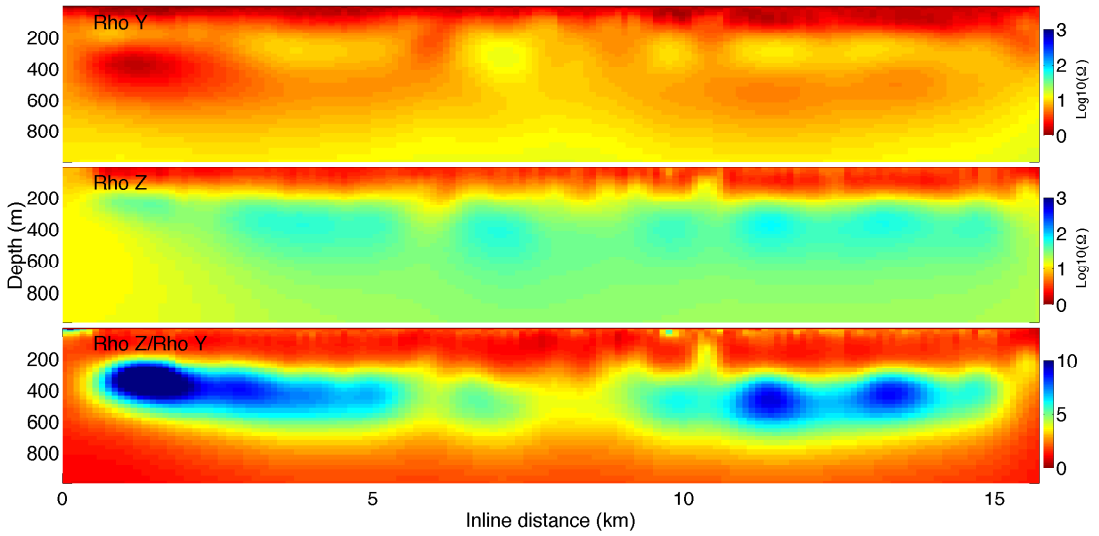

Figure A.5: Anisotropic inversion from Tow 10 2015

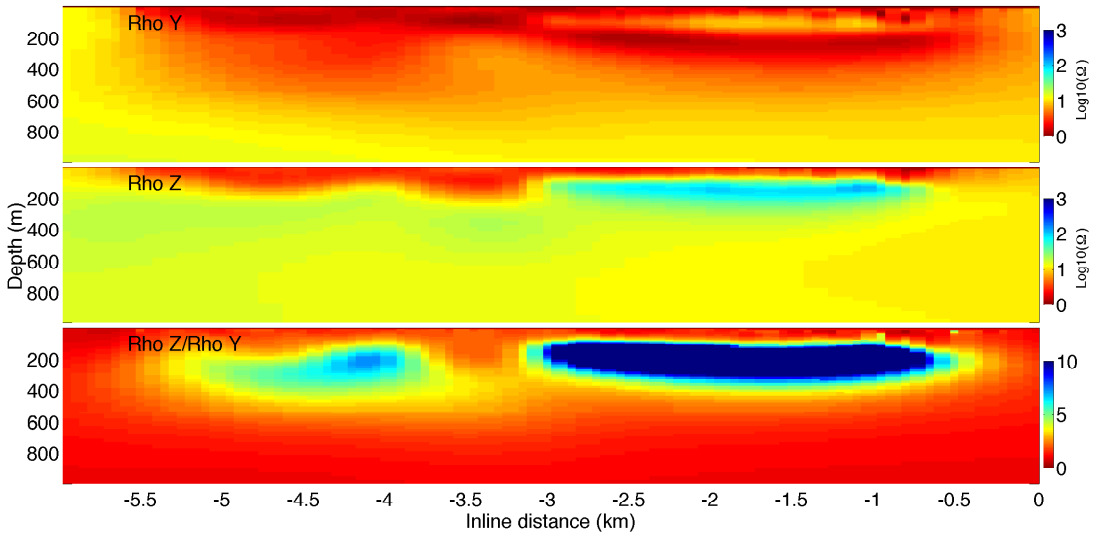

Figure A.6: Anisotropic inversion from Tow 11 2015

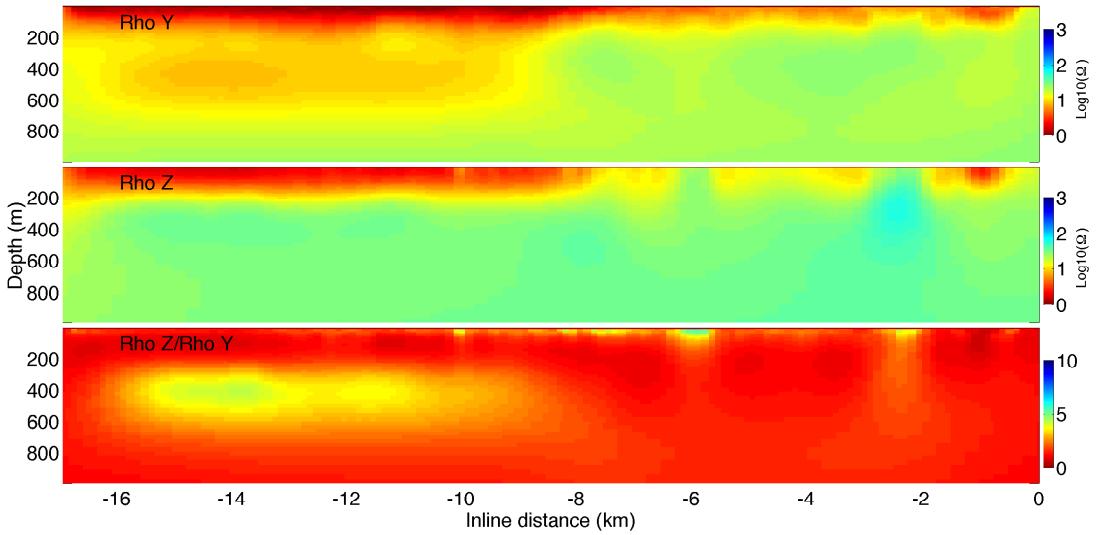

Figure A.7: Anisotropic inversion from Tow 13 2015

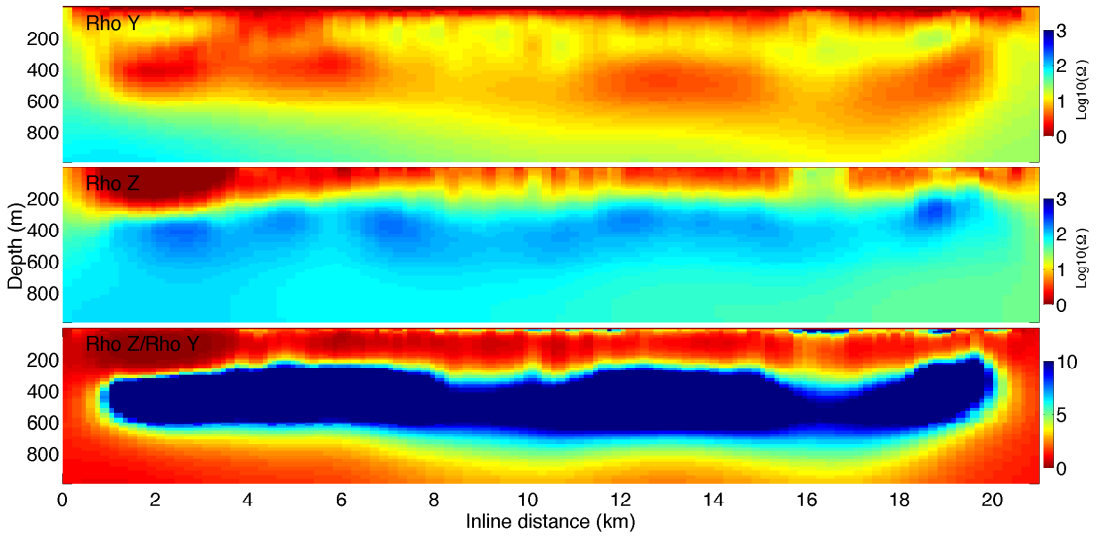

Figure A.8: Anisotropic inversion from Tow 14 2015

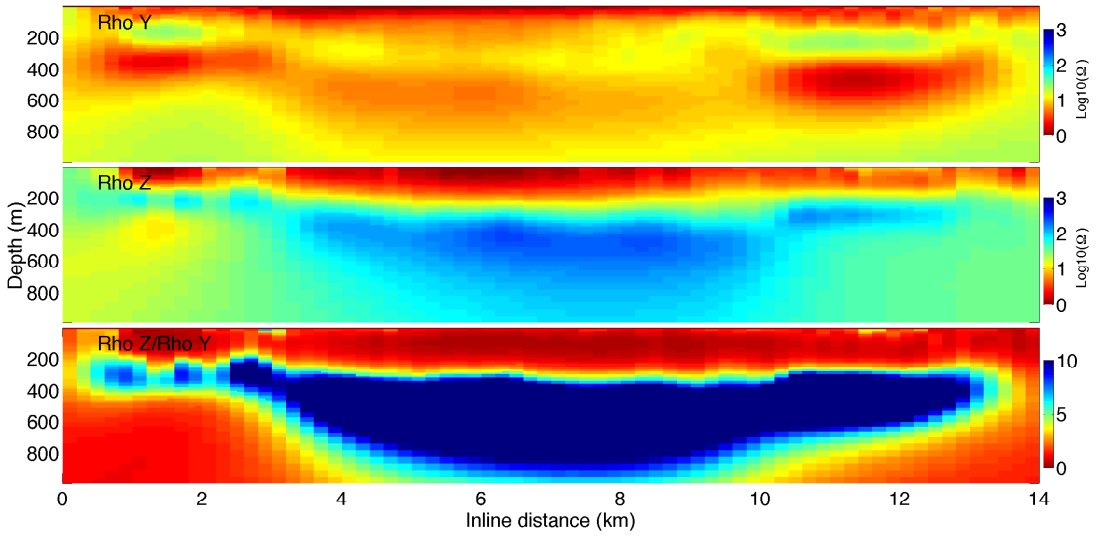

Figure A.9: Anisotropic inversion from Tow 15 2015

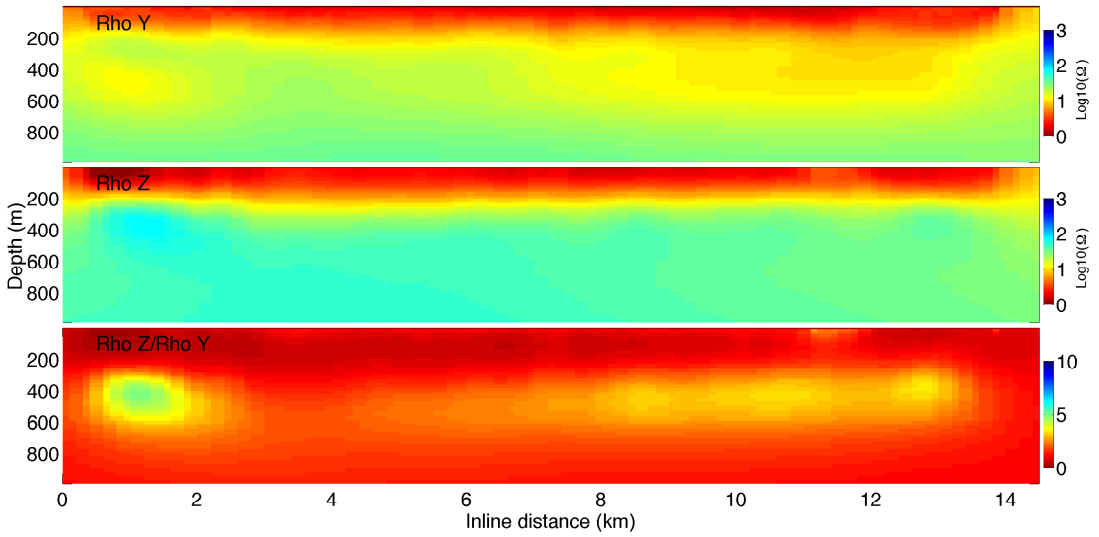

Figure A.10: Anisotropic inversion from Tow 16 2015

Appendix B

2014 Inversions

Appendix B contains all inversions from 2014 that were not presented in the text. Inversion of Tow 2 can be found in the results chapter. Inversions of tows 1, 3, and 4 can be found here.

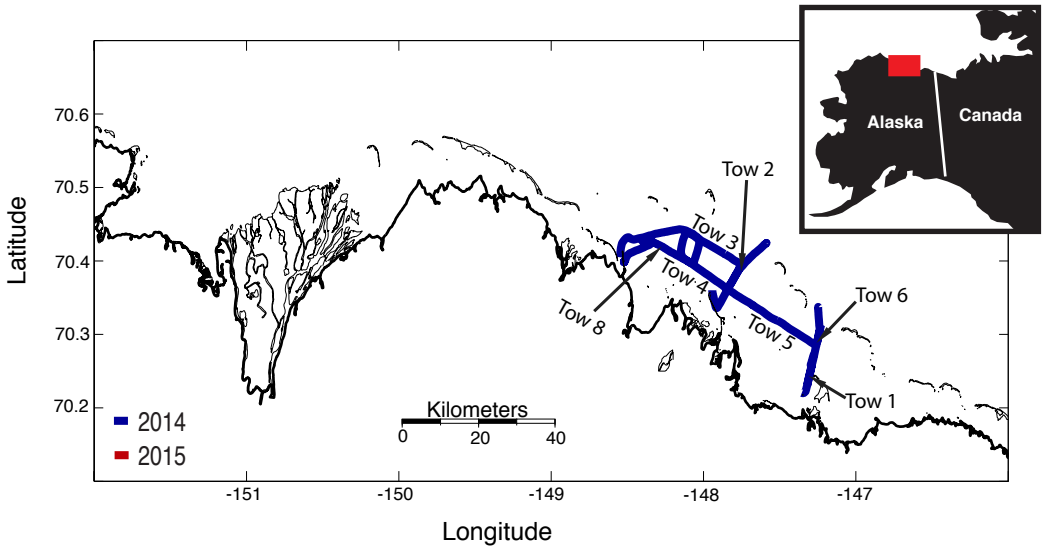

Figure B.1: Location map of tow lines from 2014.

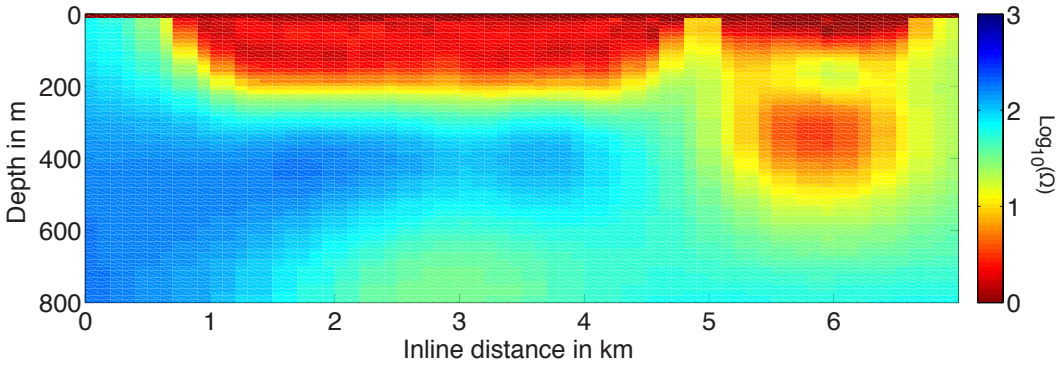

Figure B.2: Tow 1 from 2014, isotropic amplitude only.

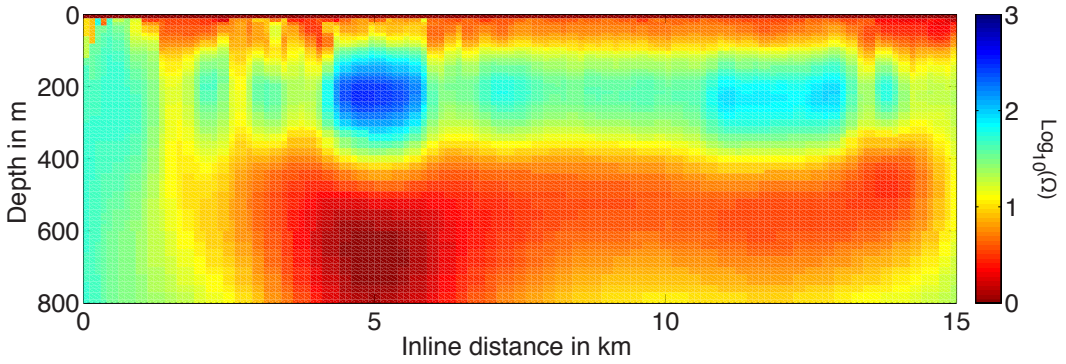

Figure B.3: Tow 3 from 2014, isotropic amplitude only.

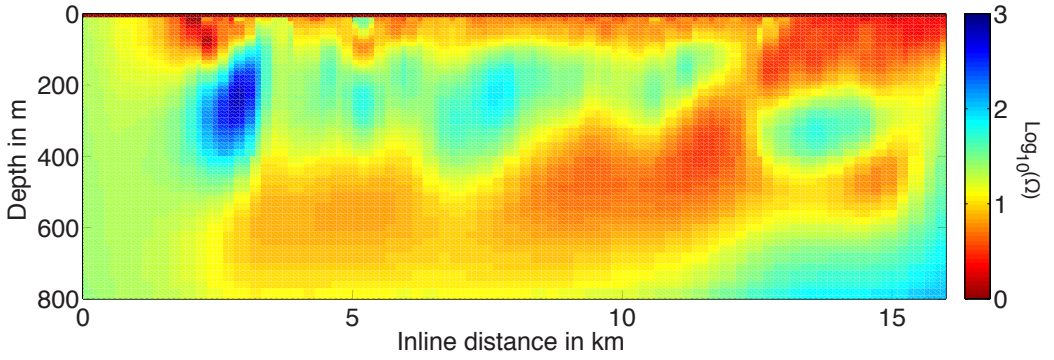

Figure B.4: Tow 4 from 2014, isotropic amplitude only.